ALKALI TREATMENTS FOR SOLUTION-PROCESSED CHALCOPYRITE PHOTOVOLTAICS FABRICATED FROM COLLOIDAL NANOPARTICLE INKS

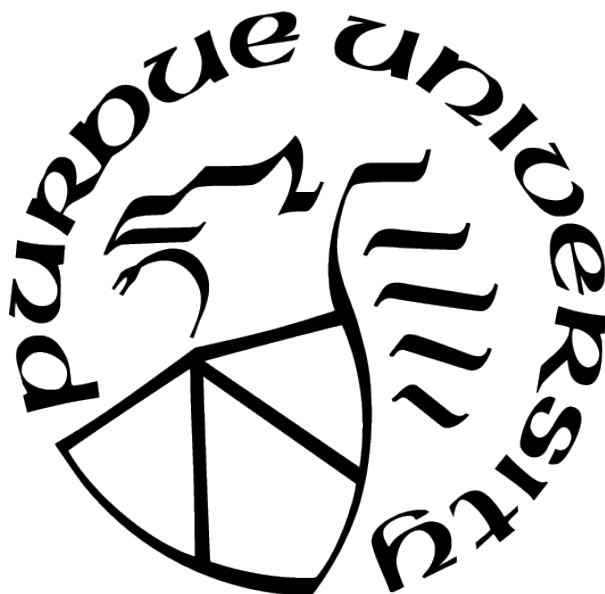by

Essam H. Alruqobah

A Dissertation

Submitted to the Faculty of Purdue University

In Partial Fulfillment of the Requirements for the degree of

Doctor of Philosophy

Davidson School of Chemical Engineering

West Lafayette, Indiana

December 2020

THE PURDUE UNIVERSITY GRADUATE SCHOOL
STATEMENT OF COMMITTEE APPROVAL

Dr. Rakesh Agrawal, Chair

Davidson School of Chemical Engineering

Dr. Letian Dou

Davidson School of Chemical Engineering

Dr. Michael Harris

Davidson School of Chemical Engineering

Dr. Peter Bermel

School of Electrical and Computer Engineering

Approved by:

Dr. John Morgan

إلى الحاضر الغائب،
حمود عبدالله الرقبه

ACKNOWLEDGMENTS

This journey to pursue a Ph.D. has been a tough and an exciting one at the same time. It would not have been possible without the help and support of a number of individuals.

First and foremost, I would like to extend my thanks and gratitude to my advisor and mentor, Prof. Rakesh Agrawal. I have been very fortunate to have had the opportunity to work as his mentee. His leadership, constructive criticism, and most importantly his dedication to safety have been instrumental in my development as an independent researcher. I have learned a lot from him throughout my time as his student, and I have gained valuable skills that will benefit me throughout my personal and professional life.

I would like to acknowledge committee members Prof. Peter Bermel, Prof. Letian Dou, and Prof. Michael Harris. I am thankful for Prof. Peter Bermel for his feedback and questions, both during my prelim and during my presentations at the weekly NPT meetings. I would also like to extend my thanks to Prof. Letian Dou for lending his expertise on photovoltaics. I also owe thanks to Prof. Michael Harris for serving on my committee and for his useful questions.

Throughout my time at Purdue, I have been lucky to have worked with a brilliant group of individuals. Special thanks to group alumni Dr. Steven McLeod and Dr. Mark Koeper for their mentorship and training when I first joined Purdue, and for introducing me and teaching me the basics of the *formidable* rapid thermal processing (RTP) furnace, of which I have become an expert. Special thanks are also extended to fellow group members and alumni Dr. Xianyi Hu, Dr. Ryan Ellis, Swapnil Deshmukh, David Rokke, Jonathan Turnley, Dr. Joe Andler, Kyle Weideman, Anna Murray, Apurva Pradhan, Daniel Hayes, Dr. Xin Zhao, Dr. Caleb Miskin, Dr. Brian Graeser, and Robert Boyne. I would also like to thank Dr. Dmitry Zemylanov at Purdue's Birck Nanotechnology Center for his assistance in conducting XPS measurements and for useful discussions.

Thanks are also owed to the staff of the Davidson School of Chemical Engineering for their assistance over the years. Melissa Laguire has been very helpful in scheduling meetings, reserving conference rooms, and reminding us of important deadlines. Yury Zvinevich, Jeff

Valley, and Nick Humphrey have also been helpful in assisting with equipment-related issues in the lab. Thanks are also extended to Bev Johnson at the Chemical Engineering Graduate Office for her help and assistance throughout my time at Purdue.

I would also like to extend my gratitude to my friends, both in West Lafayette and back home in Kuwait. Their support and their encouragement during the past five years has made graduate school a tad more bearable. Special acknowledgment goes to the Khaldiya/Dhahia group and to the Surra group. They always manage to make me enjoy my time to the fullest whenever I go home during the holidays.

Words cannot express my deepest gratitude to my family for their unconditional love and support for me throughout my life. My parents, Homoud and Lamyaa, have always pushed me to be the best I can be, and who have made who I am today. I will always be indebted to them. Gratitude is also extended to my brother, Abdullah, and my sister-in-law, Danah, whose support these past five years has kept me going, especially during periods of frustrations in the lab.

TABLE OF CONTENTS

LIST OF TABLES

LIST OF FIGURES

11

12

13

17

ABBREVIATIONS

AZO	Aluminum-doped Zinc Oxide
CBD	Chemical Bath Deposition
CGI	[Cu]/[In]+[Ga]
CGS	$CuGaS_2$
CIGS	$Cu(In,Ga)S_2$
CIGSe	$Cu(In,Ga)Se_2$
CIGSSe	$Cu(In,Ga)(S,Se)_2$
CIS	$CuInS_2$
CISe	$CuInSe_2$
CISSe	$CuIn(S,Se)_2$
C-V	Capacitance Voltage
CZTS	Cu_2ZnSnS_4
CZTSe	$Cu_2ZnSnSe_4$
CZTSSe	$Cu_2ZnSn(S,Se)_4$
DMSO	Dimethyl Sulfoxide
EDS	Electron-dispersive X-Ray Spectroscopy
EDXRD	Energy-dispersive X-ray diffraction
EQE	External Quantum Efficiency
FIB	Focused-Ion Beam
FWHM	Full Width at Half Maximum
GGI	[Ga]/[In]+[Ga]
HAADF	High-angle Annular Dark Field Imaging
ITO	Indium-doped Tin Oxide
i-ZnO	Intrinsically-doped Zinc Oxide
NMF	n-methylformamide
OLA	Oleylamine
p.c.e.	Power Conversion Efficiency

PDT	Post-Deposition Treatment
RTP	Rapid Thermal Processing Furnace
SEM	Scanning Electron Microscope
SLG	Soda-Lime Glass
STEM-EDS	Scanning Transmission Electron Microscopy EDS
TEM	Transmission Electron Microscope
UPS	Ultraviolet Photoelectron Spectroscopy
XPS	X-Ray Photoelectron Spectroscopy
XRF	X-Ray Fluorescence Spectroscopy

ABSTRACT

Today, most of the worldwide energy demand is being met by the use of non-renewable carbon-based fossil fuels that are harmful to the environment and contribute to climate change. With rising populations and rising standards of living worldwide, the demand for energy is expected to rise, increasing the need for sustainable and environmentally-friendly energy sources. Photovoltaics has the most potential of all renewable energy sources in fulfilling the worldwide energy demand in the future.

The worldwide photovoltaics market is dominated today by the use of silicon-based photovoltaics. In recent years, thin-film $Cu(In, Ga)(S, Se)_2$ (CIGSe, CIGSSe) has attracted attention as a feasible solar cell absorber material due to its favorable properties such as a high light absorption coefficient and tunable bandgap. Today, CIGSe and CIGSSe solar cells are mainly fabricated through the use of costly and resource-intensive vacuum-based routes, limiting its potential for large-scale utilization. However, solution-based routes towards CIGSe and CIGSSe manufacturing have emerged as a potentially low-cost alternative to vacuum-based CIGSe and CIGSSe manufacturing.

One of the strategies implemented in high-quality CIGSe film and device fabrication is alkali treatments. Sodium treatments are widely used in CIGSe and CIGSSe processing, and are required for high efficiency CIGSe and CIGSSe devices. Furthermore, the use of heavy alkali (K, Rb, Cs) post-deposition treatments in vacuum-based CIGSe fabrication have a resulted in a substantial increase in CIGSe device performance. Despite their beneficial effects, their use on solution-processed CIGSe (CIGSSe) films and devices remains limited. In this work, the effects of different alkalies on solution-processed nanoparticle-based CIGSSe films and devices are investigated and analyzed.

Starting with potassium, introduction of K treatments to solution-processed CIGSSe films selenized from oleylamine-capped colloidal sulfide-based $Cu(In, Ga)S_2$ nanoparticle inks resulted in enhancements in the selenization and grain growth of CIGSSe films. Furthermore, X-ray photoelectron spectroscopy (XPS) on the as-selenized films shows evidence of the presence of a high bandgap K-In-Se phase on CIGSSe films that were treated with potassium.

Moreover, solar cell devices fabricated from CIGSSe films that were treated with both sodium and potassium showed significantly enhanced performance.

Moving onto low carbon CIGSSe films that are selenized from sulfide-capped $Cu(In, Ga)S_2$ (CIGS) nanoparticle films, significant growth resistance was observed for the sulfide-capped CIGS nanoparticles, resulting in selenized and annealed films that are characterized by a thin-coarsened layer and a significantly thicker fine grain layer that is mainly composed of metals that did not incorporate into the growth front. By introducing sodium alkali treatments to the sulfide-capped films, significant enhancements to the grain growth were observed, resulting in fully-grown low-carbon CIGSSe films. It was also found that the use of an alkali treatment, prior to selenization and growth, is a requirement for sufficient growth of sulfide-capped CIGS nanoparticle films into coarsened CIGSSe films needed for high quality devices. Furthermore, rubidium alkali treatments on sulfide-capped CIGS nanoparticle films were also found to be effective in their growth-assisting ability. Moreover, increased PL response was observed with CIGSSe films that were treated with Rb prior to growth. The results and observations presented in this work provide an avenue towards enhancing the performance of solution-processed nanoparticle-based $Cu(In, Ga)(S, Se)_2$ solar cells.

1. INTRODUCTION

1.1 The Need for Solar Power

Most of the worldwide energy needs today are being met by the use of non-renewable energy sources such as petroleum, natural gas, and coal, accounting for over 80% of the worldwide energy consumption [1], [2]. With population growth and increases in the standards of living around the world, especially India and China, the worldwide energy demand is projected to increase by 50%, from 605 quadrillion Btu in 2019 to 900 quadrillion Btu by 2050. The increasing energy demand, the finite availability of fossil fuels, and the harmful effects fossil fuel emissions have on the environment have stimulated research into renewable and more environmentally-friendly energy sources. Today, renewable energy sources (wind, solar, hydroelectric, geothermal) account for only 15% of the worldwide energy demand. Their share is projected to increase to 30% by 2050 [2].

Of the available renewable energy sources, solar power is the most promising in meeting the worldwide energy demand [3]. The amount of solar energy that reaches the Earth is on the order of 10^5 TW, with 600 TW being potentially feasible to harness [3].

Renewable electricity generation in the United States is also projected to increase over the next few decades [1]. Renewables will increase their share in the U.S. electricity generation from 19% in 2019 to a projected 38%, with nuclear power and coal decreasing their shares by 2050, and natural gas remaining more or less stagnant [1]. Figure 1.1 below shows the shares of different renewable energy sources for electricity generation in the United States in 2019 and their projections by 2050. In 2019, renewable electricity generation is dominated by wind power and hydroelectric energy sources in the United States. However, by 2050, solar energy electricity generation in the United States is projected to overtake wind and hydroelectric energy sources, and increase its share of the renewable electricity market from 15% in 2019 to 46% by 2050, while wind power will remain more or less stagnant, and hydroelectric electricity generation's share of the renewables market will decrease by more than 50%.

Today, solar energy is harnessed via two techniques: solar thermal power and photo-voltaics. Solar thermal power uses solar energy to heat a fluid and generate steam that is used to produce electricity via a turbine. Photovoltaics on the other hand, uses solar radiation to produce electricity via a solid state material. This dissertation will focus on photovoltaics.
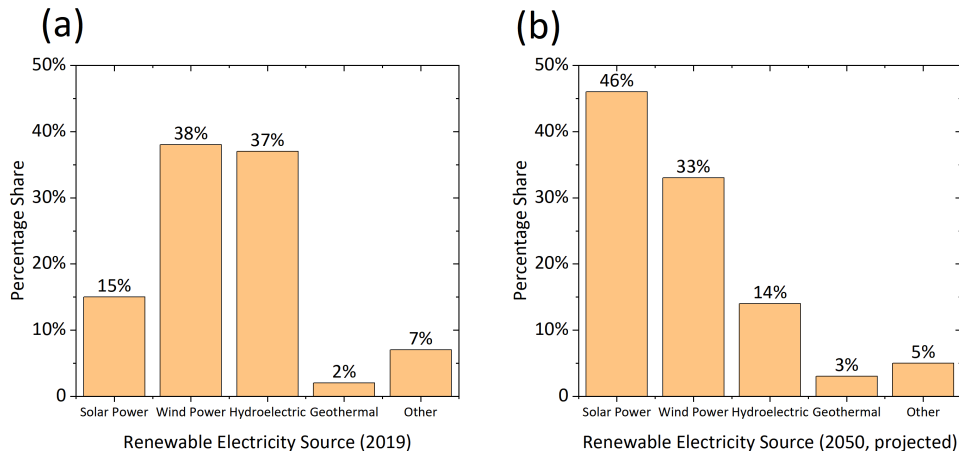
Figure 1.1. Percentage share different sources of renewable electricity generation in the United States in (a) 2019 and (b) 2050, projected. Source Annual Energy Outlook 2020 Report, U.S. Energy Information Administration [1].

1.2 Basic Principles of Solar Cells

A brief overview of solar cell device physics is presented below. For more information, the reader is referred to refs. [4]–[6].

A solar cell is a solid-state semiconductor that extracts electricity from electromagnetic radiation. Light, with a high-enough energy, generates electron-hole pairs (carriers) in the solar cell material, which are extracted to an external circuit to perform electrical work. When light with energy higher than the bandgap (a fundamental property of a semiconductor) is incident on a semiconductor, electrons will be excited from the valence band to the conduction band leaving behind holes in the valence band. The excited electron will remain in the conduction band for a given amount of time (on the order of nanoseconds to microseconds in good quality semiconductor such as GaAs, Si, and CIGSSe), and then relax back to

the valence band and recombine with holes. Excited electrons will need to be extracted to the external circuit to perform useful work, before they relax to the valence band.

The core of a solar cell device is the p-n junction diode, which consists of a p-type (electron-poor) material in contact with an n-type (electron-rich) material. When the p-n junction is first formed, electrons from the n-type material diffuse across the junction to the p-type material due to the electron concentration gradient, forming an electric field across the junction that opposes the diffusion. Diffusion of electrons will continue until the formed electric field is high enough to prevent further electron diffusion. When light is shined onto a p-n junction, light-generated carriers (electrons in the p-type material, holes in the n-type material) are swept across the p-n junction due to the built-in electric field generating a current. In a solar cell, the p-n junction is sandwiched between other materials (back contact, TCOs) to facilitate charge collection.

The single-diode model is a simple model to represent the behavior of an ideal solar cell. Figure 1.2 shows the equivalent circuit of a basic ideal solar cell. The circuit consists of a current generator in parallel with a diode. Two resistances are included in the model: a resistance in series to the current generator, R_S, and a shunt resistance that is in parallel with the current generator, R_{sh}. R_S and R_{sh} are lumped circuit parameters that are added to represent parasitic losses that occur in a solar cell device.
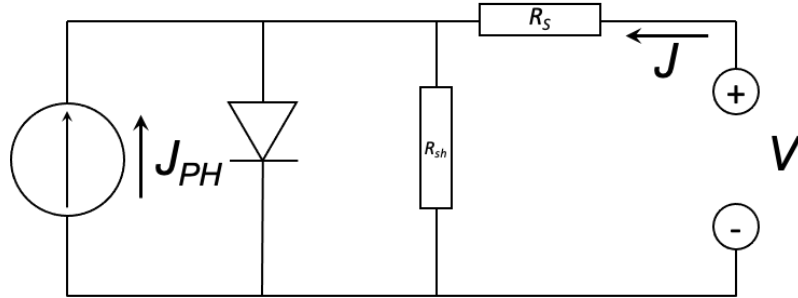
Figure 1.2. Single-diode model equivalent circuit diagram of a solar cell

For the circuit diagram shown in Figure 1.2, applying Kirchhoff rules, the current J is given by,

$$J = J_0 \left[\exp\left(\frac{q(V - AJR_S)}{nk_BT}\right) - 1 \right] + \frac{V - AJR_S}{R_{sh}} - J_{ph} \tag{1.1}$$

25

where J is the current density through the load, J_0 is the reverse saturation current density, q is the elemental charge, V is the voltage through the load, A is the device area, R_S is the series resistance, R_{sh} is the shunt resistance, n is the ideality factor, k_B is Boltzmann's constant, T is the absolute temperature, and J_{ph} is the photo-generated current.

Double diode models that account for further non-idealities in the device behavior have also been proposed [6].

1.2.1 Solar Cell Performance Characterization

The performance parameters of solar cell devices is characterized and measured under standard test conditions by shining a standardized AM1.5 light (calibrated to 1000 W/m^2), with the device temperature at 25 °C. Figure 1.3 shows a typical J-V curve, with all key parameters highlighted. The current-voltage (J-V) behavior of the device, under light and in dark is measured. Key parameters extracted from the J-V plot include the current at zero voltage (short circuit, J_{sc}), the voltage at open circuit (zero current) conditions (open circuit voltage, V_{OC}), and the fill factor (FF), which represents the 'squareness' of the J-V curve, and is defined by,

$$FF = \frac{P_{max}}{J_{sc}V_{oc}} = \frac{J_{max}V_{max}}{J_{sc}V_{oc}} \tag{1.2}$$

The most important parameter to characterize the performance of a solar cell device is the power conversion efficiency (p.c.e., η), and is defined by the ratio of the maximum power extracted from the device to the total incident power,

$$\eta = \frac{P_{max}}{P_{Incident}} = \frac{FFJ_{sc}V_{oc}}{P_{Incident}} \tag{1.3}$$

where $P_{Incident}$ is the power incident on the device (1000 W/m^2 when measured under standard AM1.5 conditions). One typical approximation that is typically done is to take the photo-generated current approximately equal to the short-circuit current, i.e. $J_{ph} \approx J_{sc}$. For more information of solar cell device characterization, the reader is referred to Hegedus et al. [7].
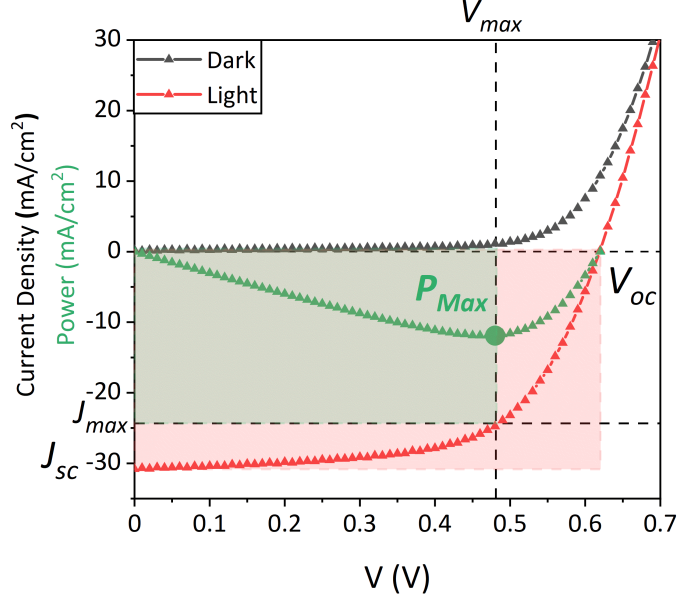
Figure 1.3. Light and dark J-V curves of a 12% p.c.e. solution-processed CIGSSe solar cell, with key parameters highlighted. The green rectangle denotes P_{max}, and the red rectangle denotes the product $J_{sc}V_{oc}$.

Another important measurement to characterize the performance of the solar cell device is the external quantum efficiency (EQE), which is defined as the probability that a photon with a given energy (wavelength) that is incident on the device will deliver an electron to the external circuit; an EQE value of unity means that every photon of a wavelength λ that is incident on solar cell device will cause one electron to be extracted to the external circuit. The short-circuit current can also be extracted from EQE data through,

$$J_{sc} = \int_0^\infty qEQE(\lambda)E(\lambda)\,d\lambda \tag{1.4}$$

where J_{sc} represents the short-circuit current density, q represents the elemental charge, λ represents the wavelength, $EQE(\lambda)$ represents the external quantum efficiency at wavelength λ, $E(\lambda)$ represents the photon flux at wavelength λ.

1.3 Photovoltaic Technologies

Currently, crystalline silicon-based solar cells dominate the solar cell market, accounting for over 82% of the photovoltaic market share, and with lab-scale single-junction conversion efficiencies approaching 27% [3], [8]. They represent the most developed and widely studied PV technology, and the most widely used today [3]. However in recent years, thin-film solar cell (TFSCs) technologies have gained interest in recent years due to their high absorption coefficients and direct bandgaps [3], [9]. These properties allow significantly thinner device thicknesses (2-3 μm as opposed to 200-300 μm for c-Si solar cells). This is translated into lower material usage in device fabrication [3], [9]. Due to this thin structure, thin-film solar cell technologies allow the fabrication of flexible solar cell devices, and building-integrated PV structures, which are difficult to implement using thick c-Si solar cell devices [9], [10].

CdTe, CIGSe (CIGSSe), and amorphous silicon (a-Si) represent the three most widely commercialized thin-film PV materials today, with CdTe dominating the thin-film PV market [3], [9]. However, in recent years, chalcopyrite $Cu(In, Ga)Se_2$ ($Cu(In, Ga)(S, Se)_2$) has garnered increased attention due to the substantial increases in lab-scale efficiencies, and the potential of high-efficiency devices to be fabricated on flexible substrates [3], [10]–[12]. Furthermore, the bandgap of CIGSe can also be tuned by adjusting the Ga-to-In ratio in the film (see Table 1.1 below), which has uses in designing next-generation tandem device structures such as $CuInSe_2$/perovskite tandem solar cells [13], [14]. Furthermore, the ability to fabricate CIGSe (CIGSSe) absorber films and devices via various solution-processed non-vacuum-based techniques potentially allows the implementation of printing or roll-to-roll fabrication, which would reduce fabrication costs considerably [15], [16]. This dissertation will focus on the $Cu(In, Ga)(S, Se)_2$ system.

1.4 The $Cu(In, Ga)(S, Se)_2$ System

Chalcopyrite $Cu(In, Ga)Se_2$ ($Cu(In, Ga)(S, Se)_2$), or CIGSe (CIGSSe) is a p-type poly-crystalline semiconductor that has attracted interest in recent years owing to its high absorption coefficient, direct and tunable bandgap [3], [9], [10], [12], [17]. CIGSe (CIGSSe) devices can also be deposited and grown on flexible substrates as only 1-2 μm-thick light

absorber layer is sufficient for good light absorption [4], [9], [10], [12] Figure 1.4 shows the crystal structure of chalcopyrite $Cu(In, Ga)Se_2$.
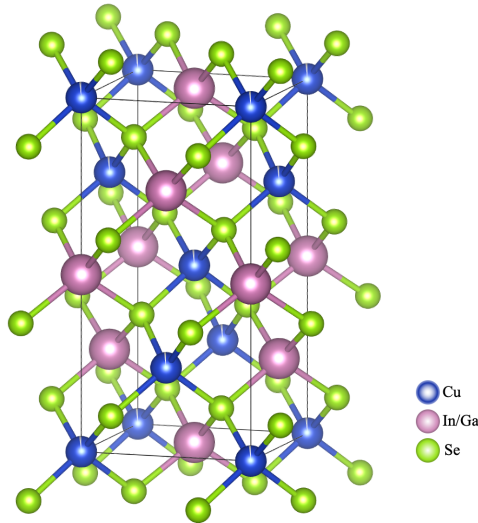
Figure 1.4. Crystal structure of chalcopyrite $Cu(In, Ga)Se_2$.

The CIGSe (CIGSSe) system is an intrinsically-doped p-type semiconductor (p-type character due to material properties, and not due to external doping), with its p-type conductivity due to the presence of Cu vacancies, which would form in the material when it is grown Cu-poor ([Cu]/[In]+[Ga] <1). High-efficiency CIGSe (CIGSSe) devices typically have the overall [Cu]/[In]+[Ga] ratio between 0.8 and 0.95. This is to enhance the p-type conductivity and prevent the formation of detrimental Cu_2Se. The formation of Cu_2Se is thermodynamically favorable when [Cu]/[In]+[Ga] is close to unity [18], [19]. As mentioned above, one of the attractive properties of the CIGSe (CIGSSe) system is the ability to tune the bandgap of the material. This is done by varying the [Ga]/[In]+[Ga] ratio, the [S]/[S]+[Se] ratio, or a combination of both [20]–[23]. The bandgaps, and lattice parameters, will generally vary linearly with the GGI and chalcogen ratio, going from 1.00 eV for $CuInSe_2$ to 2.40 eV for $CuGaS_2$. [20]–[23]. Table 1.1 below lists different common ternary chalcopyrite materials and their respective bandgaps and lattice parameters.

Table 1.1. Bandgaps and lattice parameters of common ternary chalcopyrite materials [24].

Material	Bandgap (eV)	Lattice Parameter (Å)
$CuInSe_2$	1.00	5.79
$CuGaSe_2$	1.70	5.62
$CuInS_2$	1.55	5.55
$CuGaS_2$	2.40	5.39

1.4.1 Structure of a CIGSSe Solar Cell

Figure 1.5 shows a schematic of a CIGSSe device stack. A CIGSe (CIGSSe) solar cell device is fabricated as a substrate-type structure, and is typically grown on glass substrates or flexible polymer films [10], [12]. The CIGSe (CIGSSe) device stack consists of a metallic back contact, with CIGSe (CIGSSe) film grown on top of it forming the main light absorber layer (p-type). An n-type buffer layer is deposited onto the CIGSe (CIGSSe) film, and a transparent conducting oxide (TCO) layer is then deposited on top of the buffer layer. Finally, the device is finished with deposition of metallic grids.
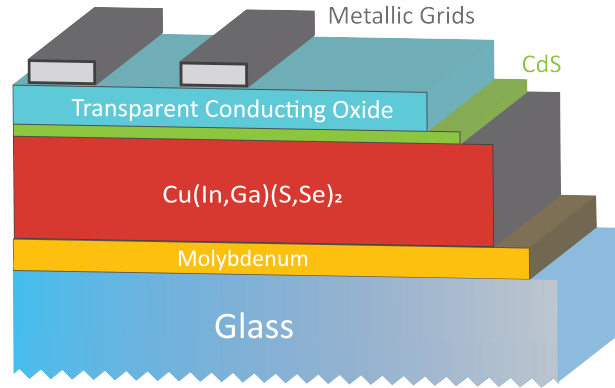
Figure 1.5. Diagram of a CIGSSe device stack fabricated on a glass substrate, and employing a CdS buffer layer.

The metallic back contact material used in almost all CIGSe (CIGSSe) devices is molybdenum as it forms an Ohmic contact with the p-type CIGSe (CIGSSe) film, and does not show any diffusion behavior into the CIGSe (CIGSSe) layer during the high temperature growth process. As for the n-type buffer layer, CdS is the most widely used material for a buffer layer, and is deposited via chemical-bath deposition, with thicknesses around 50 nm being sufficient for a high-efficiency device [25]; the thickness can be reduced to 20 or 30 nm when a heavy alkali post-deposition treatment is applied on the CIGSe film (see Chapter 2 for overview on alkali metal treatments on CIGSe (CIGSSe.)) [12], [26]. However, due to Cd toxicity, and the 'spike' band alignment between CdS and CIGSe [27], [28], high-efficiency Cd-free CIGSe devices that use alternative buffer layers have been reported [21], [28]–[31].

For the TCO layer, i-ZnO/ITO, i-ZnO/AZO (Al-doped ZnO), ZnMgO/Al-doped ZnMgO [32] are TCO layer stacks that are commonly used in CIGSe (CIGSSe) devices, and are usually deposited via radio frequency (RF) sputtering.

An overview of common CIGSe and CIGSSe film fabrication methods and processes are given below.

1.5   CIGSe (CIGSSe) Absorber Films Fabrication

CIGSe (CIGSSe) absorber films can be fabricated via various methods. A brief overview of the different methods is given below.

1.5.1   Vacuum-Based $Cu(In, Ga)(S, Se)_2$

Vacuum-based methods to grow CIGSe (CIGSSe) absorber films are the most widely used routes to grow the absorber films, and they have been responsible for producing the highest efficiency CIGSe (CIGSSe) devices. Two main vacuum-based methods are used to fabricate CIGSe (CIGSSe) films: the three-stage co-evaporation process and the two-step process. A brief overview of each is given below.

1.5.1.1 Three-Stage Co-Evaporation Process

One of the most commonly used methods to fabricate CIGSe absorber films is the three-stage co-evaporation process, which was developed by NREL in the mid 1990s [33]–[35]. The CIGSe deposition is conducted in a vacuum chamber, with copper, indium, and gallium evaporated onto Mo-coated substrates using Knudsen effusion cells.[1] Excess selenium is evaporated simultaneously with the metals; Se flux on the order of three-four times Cu, In, Ga flux is typical [36]–[39].

The three stages in this process consist of a low-temperature Cu-poor stage, followed by a high temperature Cu-rich stage, and ends with a high-temperature Cu-poor stage. The first stage is conducted at a low temperature (300 °C - 350 °C), In and Ga, along with Se, are evaporated onto the Mo-coated substrates. At the end of the first stage, the deposited film consists of $(In, Ga)Se_3$, with relatively small grain sizes [40]. In the Cu-rich second stage, the In and Ga evaporation is shut down, and the substrate temperature is increased to temperatures greater than 500 °C (typically 560 °C - 600 °C), with Cu and Se evaporated onto the film in the absence of group III elements [33]–[40]. The Cu is evaporated until the overall film stoichiometry is slightly Cu-rich ([Cu]/[In]+[Ga] $\approx$ 1.1) [18], [33]–[40]. During the second stage, the entire film undergoes a recrystallization process due to the high deposition temperature, and to the presence of a liquid Cu-Se phase [40]. The third and final stage consists of evaporating In, Ga, and Se (without Cu) at the same temperature used in the second stage, until the film's overall composition is Cu-poor (CGI $\approx$ 0.8-0.95), after which the substrate is cooled [18], [33]–[40]. The excess Se flux is maintained until the substrate temperature reaches 300 °C - 400 °C to prevent In-loss through evaporation of Se-poor In_2Se from the CIGSe film [33], [41].

Typical CIGSe films that are deposited via three-stage process have thickness on the order of 2-3 μm, and have a 'double-graded' Ga structure in which the Ga amount decreases from the back contact to minimum value slightly before the space-charge region ($\sim$ 400 nm from the film surface), and increase again towards the film surface reaching a maximum value at the interface [18], [33]–[40]. This double-graded structure leads to enhancements in

---

[1]Alkali metals are also deposited using Knudsen effusion cells via evaporation of alkali fluorides. See Chapter 2.

the device performance, compared to an ungraded film (See Chapter 7). This is similar to the back-surface field technique used in Si-based solar cells.

1.5.1.2 Two Step Process

The other more commonly used vacuum-based method to fabricate CIGSe (CIGSSe) absorber films is the two-step process. The first step of this process consists of deposition (under vacuum) of Cu, In, Ga onto Mo-coated substrates forming a metal film stack. [21], [22], [31], [42]. In the second step, the metal film stack is selenized either in a Se ambient [43], or in a H_2Se atmosphere at elevated temperature to grow and coarsen the film [21], [22], [31], [42]. The current 23.35% CIGSSe world record by Solar Frontier is fabricated via the two-step route in their Sulfurization-after-Selenization (SAS) process; the metal film stack is first selenized in H_2Se, after which the surface of the resulting CIGSe film is sulfurized in a H_2S ambient to obtain the front bandgap grading [21], [22], [31], [42].

1.5.2 Solution-Processed Thin Film $Cu(In, Ga)(S, Se)_2$

Non-vacuum solution-based routes towards CIGSe (CIGSSe) fabrication have gained interest in recent years due to their low capital costs, higher material utilization, and their compatibility with printing and roll-to-roll manufacturing [3], [44]. However, solution-processed CIGSe (CIGSSe) device performance has lagged behind its vacuum-base counterpart, with the highest reported efficiency of a solution-processed CIGSSe device being 18.68% by Solar Frontier in 2016 using a DMSO-based ink [45]. However, their exact deposition process and conditions were not disclosed [45]. Zhang et al. reported an 18.1% champion device efficiency for a solution-processed CIGSSe film fabricated using dangerous and explosive hydrazine [46]. The highest non-hydrazine CIGSSe device efficiency is 15% (based on total device area), fabricated via a nanoparticle-based route, was reported by McLeod et al. [47].

In general, solution-processed routes towards CIGSSe absorber films are two-step methods: the first of which is deposition of a precursor ink onto a Mo-coated substrate forming the precursor film, and the second is annealing the precursor film at high temperature (T $\geq$ 450 °C) in a suitable ambient (Se vapor or H_2Se) to grow the grains forming the coarsened

absorber film [44]. Subsequent device layers are deposited onto the coarsened film forming the complete device. Figure 1.6 below shows a schematic of the solution-based fabrication process of a CIGSSe device.
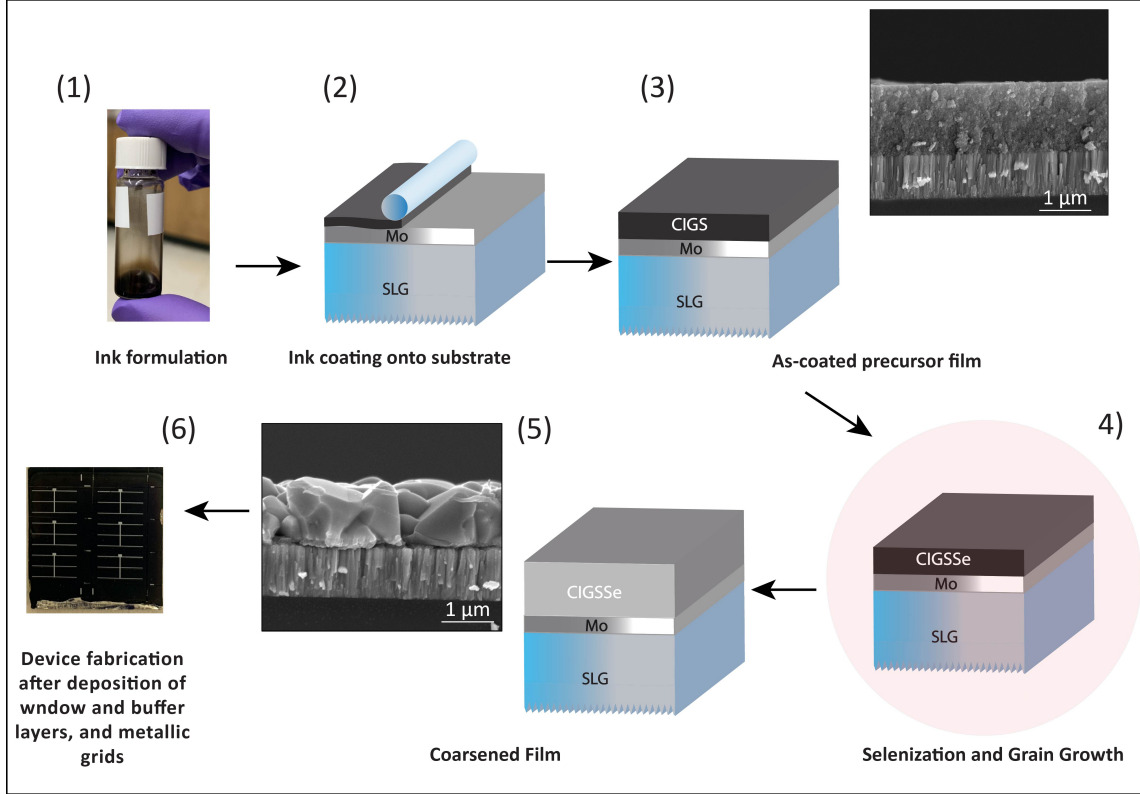
Figure 1.6. Schematic of fabrication of solution-processed CIGSSe device from CIGS nanoparticles. (1) Ink preparation and formulation. (2) Ink is coated onto Mo-coated substrates forming the as-coated film (3). (4) as-coated ink is sintered and selenized in a Se-vapor forming the coarsened film (5). (6) CIGSSe device is fabricated with deposition of window and buffer layers, and subsequent deposition of metallic grids.

Methods to fabricate solution-processed CIGSe (CIGSSe) absorber films are divided based on how the precursor ink and film are synthesized and fabricated, and can be roughly divided into nanoparticle-based routes and molecular precursor-based routes [44]. Electrochemical-based routes to produce CIGSe (CIGSSe) have also been used, but much less so than either the molecular precursor or the nanoparticle-based routes [3].

1.5.2.1 Colloidal Nanoparticle Route

Colloidal nanoparticle routes have been used extensively to synthesize a wide variety of materials and absorber films including CISSe [48], CZTSSe [49]–[53], CIGSSe [15], [47], [54]–[57], $CuAsS_4$ [58], [59], and AZTSSe [60]; and is the fabrication route used throughout this dissertation.

The use of nanoparticles allows a high degree of composition control in that the desired composition of the final absorber material can be tuned on the nano-scale [44]. In the colloidal nanoparticle-based route for CIGSSe films, nanoparticles of a precursor material are synthesized via a colloidal synthesis reaction, after which they are purified and dried. The dried nanoparticles are then suspended in a suitable solvent forming the nanoparticle ink. This ink is then coated onto a Mo-coated substrate forming the precursor nanoparticle film. The film is then annealed at high temperature ($\geq$ 450 °C) in a Se-vapor ambient to coarsen the film. The precursor nanoparticles that are used in almost all the CIGSSe nanoparticle-based routes are sulfide $Cu(In, Ga)S_2$ (CIGS), and are usually synthesized using the oleylamine (OLA) (an 18-carbon primary amine, boiling point = 364 °C) [47], [54], [56], [57]; sulfide CIGS nanoparticle are also used as the precursors to CIGSSe in this work. Oleylamine is commonly used in nanoparticle syntheses due to its excellent ability to control the kinetics and sizes of the nanoparticles, and to its ability to prevent nanoparticle agglomeration during the colloidal synthesis reaction by providing stearic hindrance between the nanoparticles [61], [62]. During the nanoparticle synthesis, the nitrogen on the oleylamine molecule attaches to the synthesized CIGS nanoparticle surface as a ligand molecule (OLA-capped nanoparticle) [15], [57], [61], [63]. Due to its high boiling point, oleylamine is difficult to remove with heat-based methods, and will typically remain attached to the nanoparticle surface, even after coating the precursor nanoparticle film. During the high temperature selenization step of OLA-capped CIGS nanoparticles into a coarsened CIGSSe film, a bi-layer morphology results consisting of a coarsened CIGSSe film on the top, and a high-carbon 'fine grain' layer on the bottom; the carbon accumulation in the 'fine grain' layer is due to the carbon leftover from the oleylamine ligand. [15], [47], [54]–[57]. Figure 1.7 shows a film cross-section of a CIGSSe film selenized from OLA-capped CIGS nanoparticles.

Ligand-exchange processes in which the oleylamine ligand is exchanged with a low-boiling ligand that would leave during the high temperature annealing phase have been developed for sulfide-based CIGS nanoparticles, and have demonstrated the removal of near-complete removal of carbon in the final film [57].
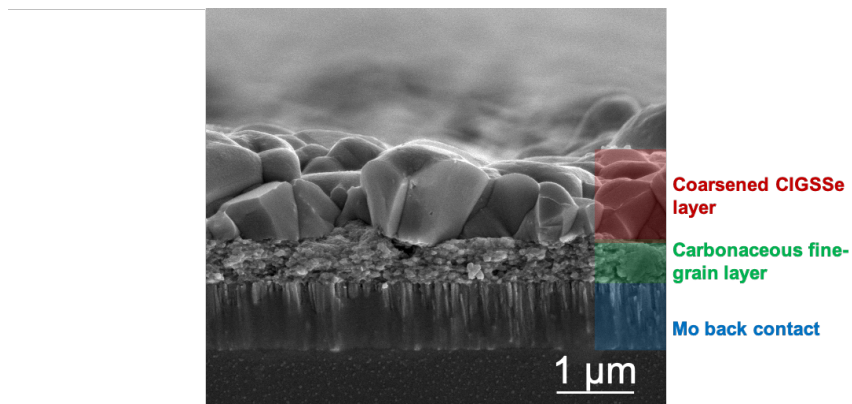
Figure 1.7. Cross-sectional SEM image of a $Cu(In, Ga)(S, Se)_2$ film selenized at 550 °C for 15 minutes from oleylamine-capped $Cu(In, Ga)S_2$ nanoparticles.

Nanoparticle-based CIGSe (CIGSSe) have shown considerable success in producing high-efficiency CIGSSe, with device efficiencies $\geq$ 12% with an un-graded CIGSSe film have been reported by various authors [47], [54], [56], [57].

1.5.2.2 Molecular Precursor Route

The other main solution-processed route towards fabricating CISe (CISSe) and CIGSe (CIGSSe) absorber films is through molecular precursors. In this route, molecular solutions of Cu, In, Ga are prepared from metal salts dissolved in a suitable solvent such as methanol [64] and DMSO, DMF [65]. The molecular solutions are then coated onto Mo-coated glass substrates, and selenized in a Se-rich environment to form the coarsened absorber film.

Molecular solutions utilizing amine-thiol chemistry are also widely used to fabricate CISSe (CIGSSe) absorber films [66]–[69]. The amine-thiol solvent system allows the flexibility to dissolve a wide variety of metals and metal salts to form the precursor ink. These include metal sulfides, metal acetates, metal iodides, metal halides, and even pure metals such as Cu, In, and Ga [63], [66]–[69]. The metal-containing (metal salts or pure metals) amine-thiol

solutions are deposited onto Mo-coated substrates via spin-coating or blade-coating form the precursor film, which is then selenized at elevated temperatures in a Se-containing ambient to form the coarsened CIGSSe film. Efficiencies of up to 15.25% (active area) have been reported for CIGSSe devices fabricated using the amine-thiol system [69].

The highest efficiency reported for a molecular precursor CIGSSe device is 18.1%, which was fabricated using a hydrazine-based approach [46].

2. ALKALI METALS IN CIGSSE FILMS AND DEVICES

2.1 Introduction

The use of alkali doping in CIGSSe processing is considered a requirement for high-quality CIGSSe absorber films, and high-efficiency CIGSSe devices [11], [12], [41], [70]–[72]. Sodium is the most studied and the most commonly used of the alkali metals in CIGSe (CIGSSe) processing, as almost all high efficiency $Cu(In, Ga)Se_2$ ($Cu(In, Ga)(S, Se)_2$) devices contain an intentional sodium addition step before, during, or after growth of the CIGSSe absorber film. More recently, the effects of the addition of heavier alkali such as potassium [12], [73], [74], rubidium [75], [76], and cesium [77], [78], on CIGSSe have led to a sharp increase in the record CIGSSe device efficiency, where lab-scale efficiencies increased from 20.35% to 23.35% within a span of six years (See Figure 2.1 below) [11].

Sodium alkali treatments generally enhance the CIGSe (CIGSSe) film grain growth [18], [55], [56], [79], [80] and improve the CIGSe (CIGSSe) bulk optoelectronic properties through grain boundary passivation [18], [70], [81]. Moreover, the use of heavier alkalies (K, Rb, Cs) in CIGSe (CIGSSe) processing through a post-deposition treatment leads to a modification of the $Cu(In, Ga)Se_2$ film surface, resulting in a surface that is depleted of both Cu and Ga, and to the formation of a high-bandgap K-In-Se (in the case of K) or Rb-In-Se (in the case of Rb) phase on the absorber surface [12], [73], [74]. These surface modifying effects have led to considerable increase in CIGSe (CIGSSe) device performance. The use of alkalies, especially K and Rb, has become an integral part in the vacuum-based CIGSe and CIGSSe processing.

In this chapter, an overview of the use and effects of different alkali metals on CIGSSe films devices is presented. Starting from sodium, its effects on the CIGSSe film morphology, growth kinetics, and optoelectronic performance is outlined. Next, the effects of heavier alkali (K, Rb, Cs) on vacuum-based CIGSSe is presented. Finally, the chapter ends with an overview of alkali use on solution-processed CIGSSe films and devices.
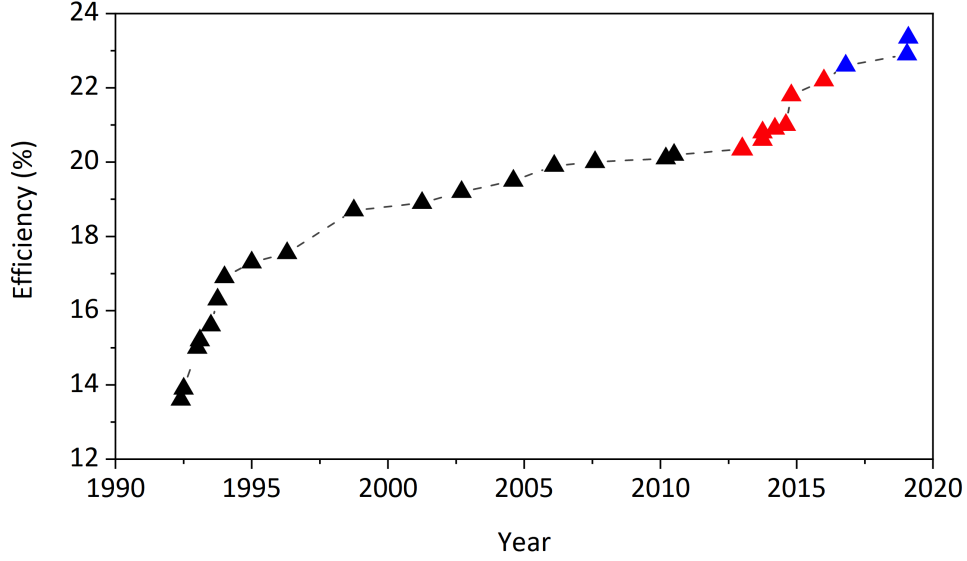
Figure 2.1. Development timeline of CIGSe (CIGSSe) record efficiencies in the last 30 years. Data points shown in red denote CIGSe (CIGSSe) devices with K treatments, while data points in blue denote CIGSe (CIGSSe) with Rb or Cs treatments. Figure adapted from Hariksos et al. [11]

2.2   The Role of Sodium in CIGSSe Films and Devices

The role of sodium on CIGSe film and device enhancement was first reported by Hedstrom et al. where $Cu(In, Ga)Se_2$ films grown on soda-lime glass substrates showed enhanced growth and significantly enhanced optoelectronic properties, compared to films grown on other substrates such as borosilicate glass, sapphire, and alumina [41]. Following that, a large number of observations and models on the specific action of Na on CISe and CIGSe (CIGSSe) were reported since then, with the consensus that sodium is highly beneficial in enhancing the optoelectronic performance of CIGSSe devices.

The morphological changes to the CIGSe (CIGSSe) film seen with Na addition are manifested in larger grain sizes (reduction in grain boundaries) and a stronger (112) texturing of the CIGSe (CIGSSe) absorber film [41], [55]. The Na enhancement of the CIGSSe film grain growth has been explained to be due to increased selenium incorporation and the formation of a liquid medium during CIGSSe film deposition and grain growth [55], [82]. During growth, sodium already present in CIGSSe films assists selenium incorporation by binding to the Se vapor forming a liquid-phase Na_2Se_x in the film [82]. The liquid Na_2Se_x acts as a

selenium reservoir in the film and accelerates metal diffusion within the film, and ultimately enhances grain growth [55], [56], [82]. Other authors have shown that the presence of Na in CIGSe films grown via the three-stage process decreases In/Ga intermixing, and in extreme cases leads to a high-In CIGSe and high-Ga CIGSe phase segregation [18], [71]. Moreover, Rudmann et al. have postulated that specific action of Na on the CIGSe growth kinetics and elemental distribution is a function of the CIGSe (CIGSSe) growth process used [18]

Sodium has also been shown to enhance the electronic and optoelectronic properties of CIGSSe films and devices, leading to significant gains in the p.c.e. manifested in an increase in open-circuit voltage, fill factor, and to a lesser degree an increase in the short circuit current. Moreover, enhanced p-type conductivity, with an order of magnitude increase in the carrier concentration, has also been reported for Na-treated CIGSSe films, as compared to untreated films.

The mechanism by which Na enhances the electronic properties of CIGSe (CIGSSe) is still a matter of debate. A number of models regarding Na-induced electronic enhancements of CIGSe (CIGSSe) films have been proposed by researchers. One such model is the presence of Na (alkali) accelerates the neutralization of V_{Se} defects, which are donor-type defects and act as recombination traps for photo-generated carriers [83]. Kronik and co-workers have proposed that Na neutralizes the V_{Se} donor-type defect through Na-catalyzed film oxidation [83]. On the other hand, Niles et al. have argued that electronic enhancements from Na are due to Na occupying In and/or Ga states forming Na_{In} and Na_{Ga} defects, which are acceptor states, and thus would enhance p-type conductivity [84]. Contreras et al. proposed that Na reduces the formation of the donor-type In_{Cu} anti-site defect by occupying Cu-sites, forming Na_{Cu} states [80]. Other reports have suggested that Na neutralizes the $(2V_{Cu} + In_{Cu})$ neutral defect complex reducing the In_{Cu} compensating defect [85]. Sodium has also been suggested to passivate the CIGSe (CIGSSe) grain boundaries by many researchers [70], [72], [86]. However this was recently called into question by Abou-Ras and co-workers [87].

2.2.1 Sodium Incorporation Methods

In CIGSe and CIGSSe processing, sodium can be incorporated into the CIGSe film via various routes, the selection of which mostly depends on the growth process used. Figure 2.2

shows a diagram of the different Na incorporation routes used in CIGSe (CIGSSe) processing. The most common route for Na addition is through diffusion from a Na-containing substrate during the high temperature growth (T ≥ 550 °C), e.g. soda lime glass. For a more precise control of the amount of Na addition into the CIGSe (CIGSSe) film, external routes to incorporate Na are used. A Na-containing species can be evaporated during CIGSe film growth, alongside Cu, In, Ga, and Se. Sodium can also be added prior to CIGSe film deposition and growth through the deposition of a Na-containing compound either on the Mo back contact, or on a CIGSe precursor film such as in the case of the two-step process or in solution-processed CIGSe (CIGSSe). Na can also be added after CIGSe film growth through a post-deposition Na treatment (usually through evaporation of NaF in a Se ambient) to enhance the CIGSe electronic properties with minimal effects on the film growth kinetics [10], [12], [73]. Na-PDT is shown to be more effective in enhancing vacuum-based CIGSe, particularly at low growth temperatures (400 °C - 450 °C) [71]. Chirilla et al. have used Na-PDT to enhance the electronic properties of CIGSe films grown on flexible polyamide films at low temperatures (T ≤ 450 °C).

The most common external sodium source used in CIGSe (CIGSSe) processing is sodium fluoride (NaF), which has been used extensively in vacuum-based CIGSe [10], [12], [70], [73], and in solution-processed CIGSSe [15], [55]–[57], [66]. The extensive use of NaF as the sodium source is mainly due to its high stability (does not disassociate during evaporation) [88], and the relative inertness of the fluoride on CIGSe film properties. Other Na sources such as Na_2Se [89], NaCl [47], [54], [64], and NaSCN [64] have also been used in CIGSe (CIGSSe) processing.

The majority of sodium incorporated into CIGSe (CIGSSe) films mainly resides on grain boundaries and grain surfaces, with much lower amounts of Na found in the intra-grain regions [18], [71], [79], [86], [90]. Cadel and co-workers have demonstrated through the use of atom-probe tomography the presence of Na in the CIGSe grains, with enrichment of Na on the grain boundaries [91]. The typical amount of Na in a high efficiency CIGSe film is reported to be on the order of 0.1 at% [71], which is typically comparable to the amount of Na that diffuses from the soda-lime glass substrate during the three-stage process when grown at high temperatures (≥ 550 °C) [71].
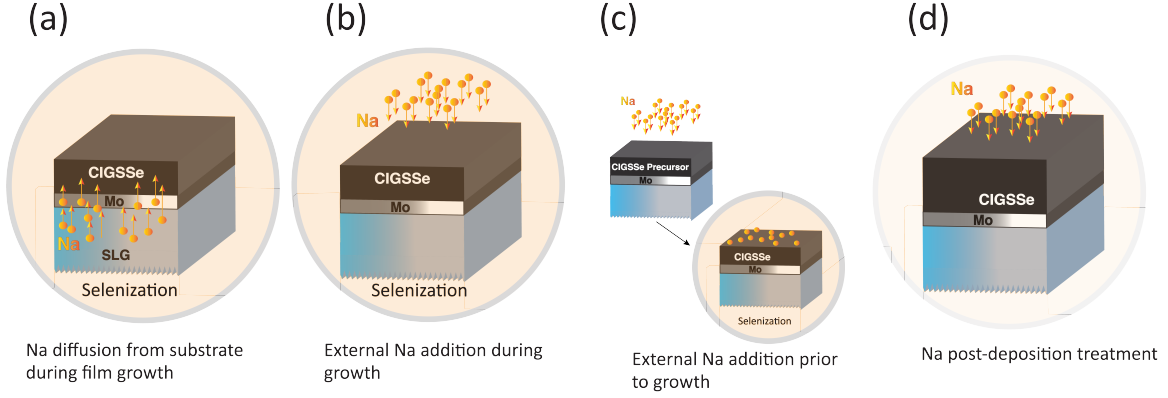
Figure 2.2. Possible routes for Na incorporation into CIGSe (CIGSSe) film. (a) Diffusion from substrate, e.g. soda-lime glass. (b) Deposition of Na-containing compound on CIGSe (CIGSSe) during growth. (c) Deposition of Na-containing compound prior to selenization and growth, e.g. on a CIGSe precursor film. (d) Deposition of Na after CIGSe (CIGSSe) film growth through a post-deposition treatment.

2.3 Potassium

The use of potassium treatments in CIGSe (CIGSSe) device fabrication represents one of the most significant developments in CIGSe (CIGSSe) solar cells, and has been responsible for the sharp increase in the record CIGSe (CIGSSe) device efficiencies in recent years [11]. The surface effect of K on CIGSe was first discovered in 2013 by researchers at Empa [12], who reported that K added through a post-deposition treatment to CIGSe films modifies the surface, and depletes it of Cu and Ga, leaving an In-rich surface [12]. The depleted CIGSe surface enhances the p-n interface with CdS through assisting Cd diffusion onto the CIGSe surface due to the higher number of Cu vacancies[1] [12]. In practice, this allows a thinner CdS layer to be deposited with minimal losses in both open-circuit voltage and the fill factor, while providing a gain in the short-circuit current due to lower light absorption in the thin CdS layer [12]. They were able to increase the device p.c.e. from 18.7% for a Na-treated film to 20.4% for a Na + K treated film [12].

Potassium post-deposition treatments on CIGSe was also reported to lead to a bandgap widening of the CIGSe surface [92], [93]. Pistor et al. have attributed the surface bandgap

---

[1]During CdS chemical bath deposition on CIGSe, a surface p-n inversion occurs due to Cd diffusion onto the CIGSe film. Cd occupies Cu vacancies forming Cd_{Cu} donor-type defects.

widening to be a result of the Cu-depleted surface [93]. However, other researchers have shown through experimental observations [73], [92] and theoretical arguments [81], [94]; that the surface bandgap widening is caused by the formation of a In_2Se_3 or a $KInSe_2$ phase on the surface, as a result of the potassium treatments on CIGSe. The higher surface bandgap improves the junction quality by forming a passivation layer at the CIGSe/CdS interface. Other authors also reported that potassium treatments not only modify the CIGSe surface, but also the CIGSe bulk [30], [56], [81]. Increased PL intensities and carrier lifetimes (from TRPL measurements) are reported for K-treated film, compared to untreated CIGSe [30], [81]. The main effects realized by KF-PDT on CIGSe (CIGSSe) solar cells are increases in open-circuit voltage and fill factor [12], [74]. Increases in the p-type conductivity of CIGSe subjected to a potassium treatment are also reported [95].

Potassium treatments on vacuum-based CIGSe film are conducted *in situ* with the CIGSe film growth as post deposition treatments (Figure 2.2 (d)), where KF is evaporated in a Se atmosphere onto the fully grown CIGSe film surface. In a typical co-evaporation process with KF-PDT, after the CIGSe film deposition, the temperature of the substrate is lowered from the deposition temperature of 550 °C - 600 °C to 250 °C - 350 °C, at which KF is evaporated, along with Se. Typical evaporated KF thicknesses used are 10 - 40 nm [12], [74], [96]. In the cases of CIGSSe films with sulfurized surfaces such as those produced by Solar Frontier, KF-PDT is done in a S-containing ambient at the same temperatures as in the conventional three-stage co-evaporation process [32]. Similar to Na, K is also found to reside mainly on grain boundaries [81]. Moreover, potassium has also been observed to accumulate at both the Mo-CIGSe and the CIGSe-CdS interfaces [12], [81].

2.4 Heavy Alkalies

Heavier alkalies such as Rb and Cs were also incorporated into CIGSe (CIGSSe) processing, and have led to significant gains in the power-conversion efficiency of CIGSe (CIGSSe) solar cells [75], [97]; the current CIGSSe world record of 23.35% by Solar Frontier utilizes CsF post deposition treatment [21]. RbF and CsF post-deposition treatments has been reported to cause similar effects to KF-PDT, which include surface depletion of Cu and Ga, and formation of a $AkInSe_2$ (Ak = K, Rb, Cs) phase on the film surface [75], [94], [98].

Similarly to the case of K, Rb and Cs have been shown through theoretical arguments to mainly reside on the grain boundaries [94], and in the case of Rb, experimental evidence of the accumulation of Rb on the CIGSe interfaces and grain boundaries has also been reported [99], [100].

Significant improvements in the open circuit voltage and fill factor are also reported with the heavy alkalies [75]. Wolter et al. reported significant increases in the p.c.e. of RbF-PDT CIGSSe devices, increasing from 13.3% for the untreated film to 18.2% for a film treated with NaF/RbF PDT [97]. Similar to K, the CIGSe (CIGSSe) film tolerance with a thin CdS layer is also improved with the heavy alkali treatments [21]. Increased surface bandgap is also reported with RbF [101].

A commonly reported observation from the CIGSe (CIGSSe) literature is that heavy alkalies, when added through a PDT, tend to replace lighter alkalies already in the CIGSSe film. This effect was first reported by Chirilla et al., where they observe that K, added through a KF-PDT to CIGSe film which had undergone a NaF-PDT prior to the K treatment, had replaced the Na that was in the film [12]. This was attributed to be a result of an ion-exchange process that exchanges heavy alkalies with lighter ones [12]. Similar effects are also reported for heavier alkalies in that Rb replaces K and Na, while Cs replaces Rb, K, and Na, when added through a post-deposition treatment [75].

2.5 Alkali Treatments in Solution-Processed Routes

Given the very beneficial effects of alkali treatments on vacuum-based CIGSe (CIGSSe) films and devices, they have not been utilized extensively in solution-processed CIGSe, with the exception of Na.

Sodium has been used in various reports in solution-processed CIGSe (CIGSSe) films and devices [15], [47], [54]–[57], [64], [66], [102]. Na is added prior to growth, and no reports of addition of Na through a post-deposition treatment for solution-processed CIGSSe are published. Effects observed with Na addition include increased grain sizes and grain growth [54], [55], [102], higher (112) texturing [55], a decrease in the thickness of the carbonaceous 'fine-grain' layer [102], reduced band-tailing [56], and increases in device efficiencies [54], [56], [64]. McLeod and co-workers have proposed that the presence of Na prevents grain

44

growth stagnation in CIGSSe films grown from a solution-processed nanoparticle-based CIGS precursor [55]. They propose that Na enhances metallic diffusion within the film, which would otherwise be limited, due to the formation of a liquid-phase Na-Se species [55]. Similar observations are also report by Moon et al. [102].

Unlike vacuum-grown CIGSe (CIGSSe), the carrier concentration does not appear to change appreciably with the addition of Na on solution-processed films CIGSSe [54], [56] and CISe [103] films and devices. Rehan et al. proposed that the reason the carrier concentration is not influenced by Na is that the mechanism by which Na acts on solution-processed CISe (CIGSSe) is different than on vacuum-based absorbers [103]. They argue that the performance gains realized by Na on solution-processed devices are due to reduced surface defects [103].

The Na sources and delivery methods used in solution-processed CIGSSe (CISe) fabrication routes are more varied than in the vacuum-based routes, however, Na is almost always added prior to selenization and growth. Na can be delivered via solution-based routes such as dipping the precursor film in an aqueous NaCl solution [47], [54], and adding a Na-containing species (NaCl [64], NaSCN [64], NaHCOO [64], [102], [103]) directly to the ink used for coating. Na also can be delivered to solution-processed CIGSSe via vacuum-based routes through the evaporation of NaF onto the precursor film prior to selenization [15], [55]–[57], [66], [67].

Heavier alkalies (K, Rb, Cs) are much less utilized in solution-processed CIGSe (CIGSSe) films and devices, despite the significant performance gains with heavy alkali treatments on vacuum-based CIGSSe (CIGSe) devices.

2.6   Scope of this Dissertation

Alkali treatments, particularly K, Rb, and Cs, are highly effective in improving the performance of CIGSe and CIGSSe solar cells. Despite their beneficial effect on vacuum-based CIGSe (CIGSSe), their use on solution-processed CIGSe and CIGSSe films and devices remains lacking, with the exception of Na.

Due to the nature of solution-processed methods, and the absence of methods that can apply alkali treatments *in situ* after CIGSSe absorber growth, alkali treatments (mainly Na) for solution-processed CIGSe and CIGSSe films are generally applied prior to growth. The

alkali would then be present in the film during the entirety of the selenization and grain growth process. Implementation of alkali treatments on solution-processed CIGSe (CIGSSe) requires taking into account how the alkali affects the film formation and growth, as well as its effects on the electronic and optoelectronic properties of the absorber film. These two aspects, combined with the drastically different growth mechanism involved in the selenization and grain growth of solution-processed CIGSe and CIGSSe over their vacuum-based counterparts, warrant investigation as the literature is currently lacking in this regard. This differs from vacuum-based CIGSe and CIGSSe where generally post deposition treatments are applied *in-situ* after absorber growth.

In this report, the effect of different alkalies on solution-processed nanoparticle-based CIGSSe absorber films and devices is investigated. The CIGSSe films used throughout this dissertation are fabricated from the selenization of $Cu(In, Ga)S_2$ nanoparticles, both high-carbon oleylamine-capped and low-carbon sulfide-capped nanoparticles are used.

Starting with Chapter 3, the effect of potassium on the CIGSSe films growth, morphology, surface chemistry, and optoelectronic performance is investigated. Addition of K into the as-coated OLA-capped CIGS nanoparticle film has shown to be effective in improving the grain growth of CIGSSe films, and contributes to the formation of a surface species not observed for untreated or films treated with Na only. Furthermore, significant optoelectronic performance enhancements were realized via inclusion of K treatment. In chapter 4, analysis of the effect of KCN, an etchant used in the nanoparticle-based CIGSSe processing [47], [54], on sulfide-based CIGS nanoparticles, and subsequent CIGSSe films fabricated from the CIGS nanoparticles, is presented. It is found that KCN etches Cu and Ga selectively from the film bulk, and that CIGSSe films fabricated from KCN-etched CIGS nanoparticles are composed of a mixture of two-phases: α-$Cu(In, Ga)Se_2$ and the Cu-deficient β-$Cu(In, Ga)_3Se_5$. Moreover, enhanced grain growth is observed for CIGSSe film selenized from KCN-treated CIGS nanoparticle films, which is explained by the potassium-induced growth assisting behavior, with the potassium introduced into the film from the KCN treatments.

In Chapter 5, growth behavior of low-carbon ligand-exchanged DAS-capped CIGS nanoparticles is analyzed. it is found that DAS-capped CIGS nanoparticles are very resistant to grow into coarsened CIGSSe films due to their different surface properties, compared with

46

the high-carbon OLA-capped CIGS nanoparticles, with untreated CIGSSe films selenized from DAS-capped CIGS nanoparticles showing poor optoelectronic performance. It is also observed that treating the DAS-capped films with alkali leads to a step change in both the extent of growth, and in the optoelectronic performance of CIGSSe films and devices selenized from DAS-capped CIGS nanoparticles, and that an alkali treatment applied prior to selenization, is required for adequate film growth.

In Chapter 6, preliminary results on the inclusion of Rb into low-carbon CIGSSe absorber films is presented. It is found that Rb, like Na and K, shows growth-assisting behavior, which has not been observed in the literature. Moreover, absorber films fabricated from Rb-treated DAS-capped CIGS nanoparticles show enhanced PL signals, implying better film quality and reduced non-radiative recombination. Finally in Chapter 7, preliminary results on the inclusion of Ga grading, a feature of all high-efficiency CIGSe and CIGSSe devices, on solution-processed nanoparticle-based CIGSSe films is presented.

3. EFFECTS OF POTASSIUM ON CIGSSE SOLAR CELLS FABRICATED FROM OLEYLAMINE-CAPPED CIGS NANOPARTICLES

3.1 Introduction

As described in Chapter 2, achieving high-efficiency CIGSSe solar cells has required the use of alkali treatments [54], [83], [89]. Sodium treatment for CIGSSe has been utilized extensively in improving device performance and efficiency, both in vacuum-based routes [89], [104], and in solution-processing routes [47], [54], [66]. Sodium is known to enhance the performance of CIGSSe solar cell through passivation of grain boundaries and increased carrier density [85], [89], [105], [106]. Moreover, If supplied before or during CIGSSe growth, Na also enhances grain growth of the absorber layer (e.g. when CIGSSe is grown on SLG substrates) [18], [55]. Other alkali such as potassium, lithium, and cesium were thought to act in a similar manner as sodium [79], [80]. However, one of the significant developments in CIGSSe processing in recent years has been the discovery the effects that heavy alkali (K, Rb, Cs) post-deposition treatments have in improving the performance of CIGSSe solar cells [12], [21], [30], [75]. Chirilă et al. have shown that unlike sodium, potassium added through a post-deposition treatment modifies the absorber surface by inducing the depletion of Cu and Ga from the surface and rendering it Cu and Ga poor, thereby enhancing Cd diffusion into the CIGSSe surface during CdS chemical bath deposition [12]. This ultimately leads to an improvement of the junction quality and allows the deposition of a thinner CdS buffer layer without significant loss of V_{oc} or FF [12]. Moreover, reports in the literature have observed surface bandgap widening for CIGSSe films subjected to a KF-PDT or NaF/KF-PDT treatments [73], [93]. Pistor et al. have attributed the surface bandgap widening to

be a result of a Cu-depleted film surface [93]. However, other reports in the literature have shown that a high bandgap In_2Se_3 or $KInSe_2$ surface phase forms on the CIGSe absorbers subjected to a KF-PDT treatment, and that this surface phase is responsible for the increased surface bandgap observed in KF-treated CIGSe [73], [81], [92], [94]. The increased surface bandgap enhances junction quality and reduces interface recombination [92]. Despite these very beneficial effects of potassium treatments, they have only been applied to vacuum-based CIGSSe solar cells, and to the best of our knowledge no report on the systematic use of K treatments on solution-processed CIGSSe devices is published. Guo et al. used potassium cyanide treatments on CIGS nanoparticle films prior to selenization to render them Cu-poor and observed performance improvements [54].

In this chapter, the effects of potassium treatments on solution-processed CIGSSe films is explored through the use of potassium fluoride as the K source. First, we study the effects potassium has on the morphology and grain size of the absorber films. Next, we show how potassium alters the surface chemistry of the CIGSSe absorber film using XPS where it is found to cause the formation of an additional Se surface state not present in non-treated films or NaF-only treated films. Finally, the optoelectronic performance of CIGSSe solar cells in terms of J-V parameters, EQE, and carrier concentration with varying potassium and/or sodium content is evaluated. We find that, like sodium, potassium enhances the growth of CIGSSe grains from CIGS and leads to a larger grained film. Additionally, we find that K-treated films show enhanced optoelectronic performance manifested in higher open-circuit voltage and fill factor, as compared to non-treated and Na-only treated films. Post-selenization potassium treatment, as is done on vacuum-based CIGSSe, on solution-processed nanoparticle-based CIGSSe absorbers is also explored. XPS surface analysis on a KF post-deposition (selenization) treated CIGSSe film show the presence of the K-In-Se surface state, and that a PDT is necessary to induce Cu and Ga depletion from the surface.

3.2 Experimental Section

3.2.1 Cu(In, Ga)S₂ Nanoparticle Synthesis

$Cu(In, Ga)S_2$ nanoparticles were synthesized via a solvo-thermal/ hot-injection reaction of a sulfur solution and Cu,In, and Ga salts, as outlined by McLeod et al and Guo et al.[47], [54]. Briefly, a 1.0 M sulfur (Sigma-Aldrich, 99.99%) in degassed oleylamine (Sigma Aldrich, reagent grade 70%, $\geq$ 98% primary amines) solution is prepared in a N_2-filled glovebox by adding sulfur flakes in oleylamine-containing flask which was sealed in the glovebox. The S-OLA was heated at 65 °C for 1 hour to ensure complete dissolution of sulfur in the oleylamine. The metals-OLA solution is prepared by adding 1.38 mmol Cu(II) acetylacetonate (Sigma Aldrich, 99.9%), 1.5 mmol In acetylacetonate (Sigma Aldrich, 99.99%), and 0.45 mmol Ga acetylacetonate (Sigma Aldrich, 99.99%) to 12 ml of oleylamine in a nitrogen-filled glovebox. The metals-OLA flask is taken out of the glovebox and preheated to 285 °C under inert argon. Upon reaching 285ºC, the 1.0 M sulfur-OLA solution is injected into the metal salts-OLA flask. The reaction was allowed to proceed for 30 minutes at 285 °C under Ar atmosphere. Following the reaction, the nanoparticles were washed in hexane and alcohols to remove excess OLA and unreacted precursors. The as-coated $Cu(In, Ga)S_2$ nanoparticle film have a [Cu]/[In]+[Ga] ratio of 0.92 $\pm$ 0.02, and [Ga]/[In]+[Ga] ratio of 0.27 $\pm$ 0.01, as measured by XRF.

3.2.2 Nanoparticle Film Formulation and Alkali Addition

The synthesized $Cu(In, Ga)S_2$ nanoparticles were then suspended in hexanethiol forming the colloidal nanoparticle ink. The ink was then coated onto Mo-coated soda-lime glass substrates via blade-coating technique and annealed at 300ºC to evaporate excess organic material. No intentional Ga grading was applied. Sodium and potassium were supplied by evaporating NaF (Sigma Aldrich, 99.99%) and KF (Sigma Aldrich, 99.9%) onto the as-coated sulfide CIGS nanoparticle film, or the as-selenized CIGSSe films, via e-beam evaporation. No KCN treatment was used.

3.2.3 Absorber Selenization And Growth

$Cu(In, Ga)S_2$ (CIGS) nanoparticle films were selenized and grown into $Cu(In, Ga)(S, Se)_2$ (CIGSSe) grains in a tubular furnace under a Se-argon atmosphere. The nanoparticle film is placed in a rectangular graphite box along with Se pellets and annealed at 500 °C for 20 minutes under inert argon. The graphite box was then allowed to cool naturally to room temperature, also under an argon atmosphere. The selenized CIGSSe films have a [Cu]/[In]+[Ga] ratio of 0.87 ± 0.02, and [Ga]/[In]+[Ga] ratio of 0.26 ± 0.01, as measured by XRF.

3.2.4 Solar Cell Fabrication

CIGSSe solar cells were fabricated using the conventional stack SLG/Mo/CIGSSe /CdS/i-ZnO/ITO/Ni-Al grids. 50 nm thick CdS n-type buffer layer was deposited via chemical-bath deposition. This is followed by deposition of 80 nm i-ZnO and 220 nm of indium-doped tin oxide (ITO) TCO layers using radio frequency (RF) sputtering. Devices were finished by evaporation of Ni-Al grids using e-beam evaporation. Individual cells were isolated via mechanical scribing, with each cell area having a nominal area of 0.47 cm^2. Unless otherwise stated, all devices shown have 100 nm MgF_2 anti-reflective coating deposited via e-beam evaporation.

3.2.5 Characterizations

Elemental ratios were measured using a Fischerscope XAN 250 X-ray fluorescence instrument. Plan-view and cross-sectional scanning electron images were taken using a FEI Quanta electron microscope under an accelerating voltage of 10 keV. Grain size analysis and quantification of each alkali condition was conducted on the SEM plan view images by first identifying individual grains using edge detection in Adobe Photoshop, and then using ImageJ image processing software [107] to produce average grain area and grain perimeter

distributions, as shown by McLeod et al. [55]. Grain diameters were calculated by assuming circular grains using the relation [55]:

$$GrainDiameter = 4 \times \frac{GrainArea}{GrainPerimeter} \qquad (3.1)$$

Powder X-ray diffraction data was collected in Bragg-Brentano mode using a Rigaku Smart-Lab diffractometer with a Cu K_α radiation source. Raman spectroscopy data was collected using a Horiba/Jobin Yvon HR800 confocal microscope using a 633 nm He:Ne laser with 100x magnification.

X-ray photoelectron spectroscopy (XPS) data was collected on the selenized CIGSSe films at the *Surface Analysis Facility of the Birck Nanotechnology Center, Purdue University* using a Kratos AXIS Ultra DLD Imaging X-ray Photoelectron Spectrometer, with a monochromatic Al K_α (1486.6 eV) radiation and a chamber base pressure of less than 2×10^{-9} Torr. To minimize oxygen surface contamination after selenization, samples were transferred rapidly from the selenization furnace to a N_2-filled glovebox with a transfer time of less than 1 minute. Samples were then soaked in dilute ammonia solution in the glovebox to remove excess alkali and alkali fluorides from the surface, after which they were then dried with nitrogen and vacuum sealed inside the glovebox for transfer to the XPS instrument. The vacuum seal was broken in an inert glovebox connected to the XPS instrument with a load-lock chamber through which the samples were loaded into the XPS chamber. XPS photoelectron peak analysis and fitting was done using CasaXPS software with Voigt profiles and a linear background. The adventitious carbon C 1s peak is set to 285 eV. Spin-orbit doublets' FWHM of respective Voigt profiles are set equal and the peak area is fixed according to corresponding $|2j + 1|$ multiplicity of each orbital [108]. All XPS spectra were area normalized to the Se 3d peak area of each respective sample.

3.2.6 Solar Cell Characterization

Four-point probe current-voltage (J-V) measurements were conducted under standard AM1.5 conditions using an Oriel Sol3A solar simulator calibrated to 1000 W/cm^2 using an Oriel 91150 V silicon reference cell. All J-V measurements were conducted at 25 °C using

a temperature-controlled stage. J-V data was analyzed according to methods provided by Hegedus and Shafarman [7]. External quantum efficiency (EQE) data was taken at zero bias using an in-house built instrument with a preamplifier and lock-in amplifier for signal processing with a chopper frequency of 160 Hz. Capacitance-voltage profiling was conducted using an Agilent 4284A impedance analyzer. Capacitance-voltage data was collected on completed devices under dark conditions at room temperature at 100 kHz AC frequency and 2 mV$_{RMS}$.

3.3   Results

To elucidate the effect potassium has on the morphology of the film, nanoparticle films with no alkali, 10 nm, 20 nm, and 50 nm evaporated KF were selenized at 500 °C for 20 minutes with excess Se, as discussed in the experimental section.

Figure 3.1 shows the SEM plan view and cross-sectional images of the selenized absorber films with different amounts of evaporated KF prior to selenization, and Figure 3.3(a) shows the average grain diameter of CIGSSe films selenized with different KF amounts. The CIGSSe grain size and morphology are affected by the amount of potassium that is evaporated onto the film with the grain size and coarsened film thickness increase with the amount of KF added to the film prior to selenization. The plan view images (Figure 3.1, left column) and average grain diameter (Figure 3.3(a)) show the film grain size gradually increasing with increasing KF amount. Moreover, a simultaneous decrease of the underlying 'fine grain' layer thickness is also observed. Increasing the evaporated KF thickness to 50 nm shows CIGSSe grains starting to separate into islands, with pinholes between them exposing the fine grain layer underneath. (Figure 3.1 (g-h)). The fine grain layer is typically observed for solution-processed CIGSSe and CZTSSe absorber films [53], [55], [66], [68]. The origin of this layer is primarily due to the carbon leftover from carbon-containing ligands and reagents that are used during the processing steps prior to selenization [66], [68], [109]–[111].

The potassium effect on the growth morphology and grain size is similar to what is seen with sodium in CIGSe[18], [54], [55] and in CZTSSe [112]. To compare the effects between Na and K treatments, CIGSSe films were selenized with 5 nm, 10 nm, 15 nm, and 30 nm of NaF evaporated prior to selenization; Figure 3.2 shows the SEM plan-view and cross-sectional
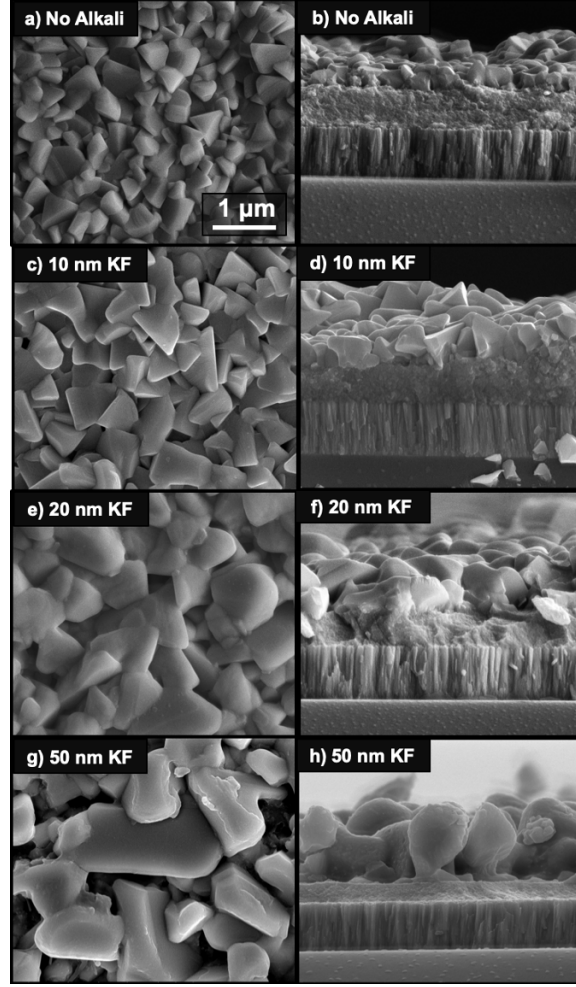
Figure 3.1. SEM plan-view (a,c,e,g) and cross-sectional (b,d,f,h) images of $Cu(In, Ga)(S, Se)_2$ films selenized at 500oC for 20 minutes with no alkali addition (a-b), 10 nm KF (c-d), 20 nm KF (e-f), and 50 nm KF (g-h). Scale bar is same for all images.

images of those films, while Figure 3.3(b) shows the measured average grain diameter. Films treated with NaF show larger grain sizes and a thicker coarsened layer than films treated with a similar thickness of KF; the selenized grain film thickness with 10 nm NaF (Figure 3.3 (b); Figure 3.2 (b),(f)) is larger than in the 10 nm KF film (Figure 3.1 (c), (d); Figure 3.3 (a)). Moreover, the film that was selenized with 30 nm NaF has comparable average grain size (Figure 3.3 (a), (b)) as the 50 nm KF film with a similar island morphology and pinholes exposing the carbonaceous fine grain (Figure 3.1 (g,h). For the same evaporated thickness, NaF is more active than KF in enhancing the grain growth and sintering of CIGSSe films.
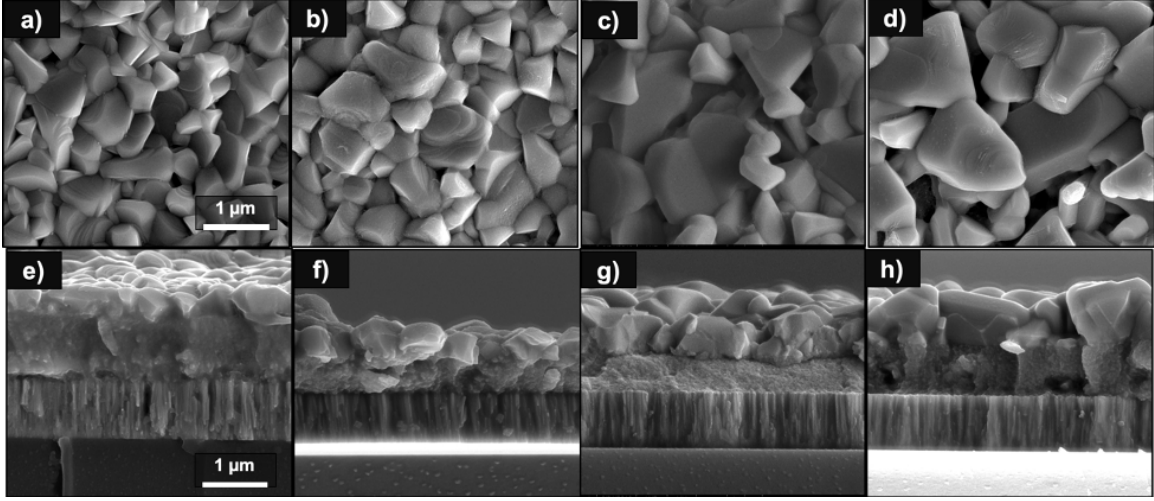
Figure 3.2. SEM plan-view and cross-sectional images of $Cu(In, Ga)(S, Se)_2$ films selenized at 500 °C for 20 minutes with 5 nm NaF (a,e), 10 nm NaF (b,f) 15 nm NaF (c,g), and 30 nm NaF (d,h). Scale bar is the same for all Images.

The higher activity of sodium over heavier alkalies (K, Cs) in enhancing the grain growth has also been observed in vacuum-based CIGSe grown via co-evaporation [80].

Braunger et al. have proposed that Na enhances growth because it enhances selenium incorporation in the film [113]. Sodium is proposed to bind to vapor selenium and forms a liquid Na_2Se_x which has a higher sticking coefficient than Se [113]. Furthermore, Na_2Se_x segregates at grain boundaries and will act as a liquid reservoir for selenium during growth [113]. Presence of liquid Na_2Se_x during growth also provides an enhanced medium for elemental diffusion, which will assist sintering and grain growth [114], [115]. McLeod et al. have investigated the effect of Na on the growth of CIGSSe films from a CIGS nanoparticle precursor and have hypothesized than Na present during growth will assist with Cu, In, and Ga diffusion, which otherwise would be limited, by forming a liquid flux agent in the film [55]. As for potassium, no mechanism regarding its ability to impact the grain growth of CIGSe (CIGSSe) from a nanoparticle film has been reported in the literature. Results in Figure 3.1 and Figure 3.3 (a) show that the final CIGSSe grain size correlates with how much K is in the film with a similar trend observed for Na-treated films (Figure 3.3 (b) and Figure 3.2). Moreover, the same trend was observed for films selenized with both NaF and KF treatments. Figure 3.4 shows SEM plan-view and cross-sectional images of CIGSSe films
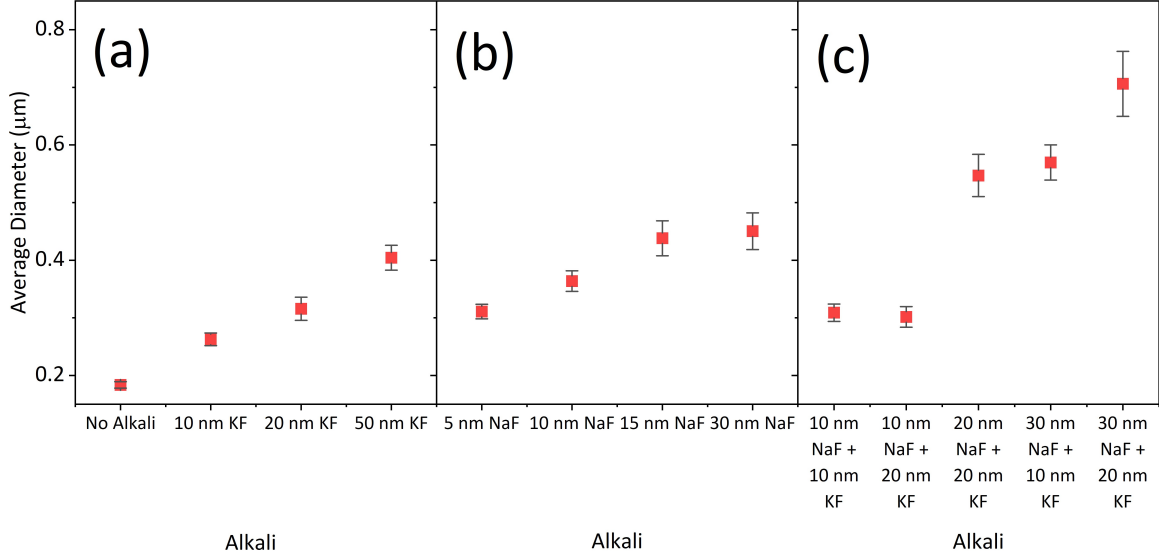
Figure 3.3. Average grain diameter of CIGSSe films selenized at 500 ºC for 20 minutes with (a) different KF amounts, (b) different NaF amounts, and (c) with different NaF and KF amounts

treated with both Na and K, while Figure 3.3 (c) shows the average grain diameter. Adding Na, K, or both assists in the growth and leads to a film with larger grain size. Since similar effects on the morphology are observed in NaF and KF-treated films, it is likely that K acts in a comparable mechanism as Na in terms of its effect on the growth of CIGSSe films. Figure 3.5 (a), (b), and (c) show the PXRD patterns of the selenized films with different alkali contents; and Figure 3.5 (d) shows the Raman spectra of the films selenized with different KF amounts. A broad shoulder to the left of CIGSe Raman A1 mode at ~ 155 cm^{-1} is detected for 20 nm KF-treated film, which is characteristic of the ordered defect complex (ODC). The ODC has lower Cu content than $Cu(In, Ga)Se_2$ chalcopyrite structure [66], [74], [116].

The surface chemical environment of the selenized $Cu(In, Ga)(S, Se)_2$ films was analyzed using X-ray photoelectron spectroscopy (XPS). Figure 3.6 shows the XPS data for the Se 3d core level for CIGSSe films selenized with different thicknesses of alkali fluorides deposited prior to selenization: without addition of alkali (No Alkali), 15 nm NaF, 10 nm KF, and 20 nm KF. Voigt peak fitting on the Se 3d XPS signal shows the presence of two Se 3d contributions (Se-1 and Se-2) for all samples. Se-1 and Se-2 signals have been suggested to
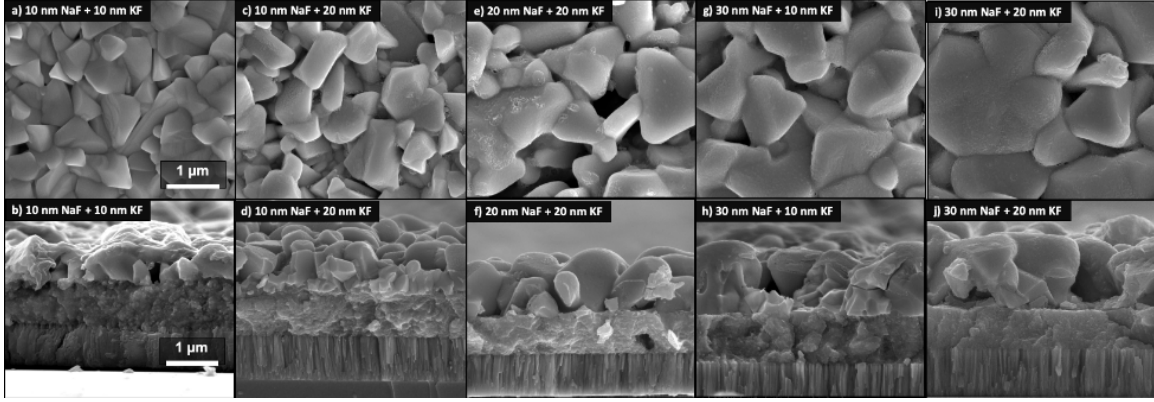
Figure 3.4. SEM plan-view and cross-sectional) images of $Cu(In, Ga)(S, Se)_2$ films selenized at 500 °C for 20 minutes with different NaF + KF combinations evaporated onto the as-coated film prior to selenization: 10 nm NaF + 10 nm KF (a-b), 10 nm NaF + 20 nm KF (c-d), 20 nm NaF + 20 nm KF (e-f), 30 nm NaF + 10 nm KF (g-h), and 30 nm NaF + 20 nm KF (i-j). Scale bar is same for all images.

belong to the CIGSe chalcopyrite chemical environment [26], [73], [74], [117]. For the sample selenized with 20 nm KF, we were able to identify an additional minor Se 3d contribution (Se-3) at lower binding energy than the Se-1 and Se-2; the Se-3 is not observed in either the No Alkali, 15 nm NaF, or the 10 nm KF samples. This low-binding energy state is observed in vacuum-grown CIGSe subjected to a KF-PDT, and is attributed to a K-In-Se surface species [26], [73], [92]. Handick et al. have shown that the K-In-Se widens the bandgap at the absorber surface markedly, and have suggested that this would aid in the passivation of the CIGSSe/CdS junction and that this surface state is one of the reasons for the increased performance of films treated with KF-PDT [92]. Figure 3.7 shows the XPS spectra of Se LMM-K 2p region. A shoulder on the Se LMM peak is observed on the lower binding energy side at $\sim$ 293.7 eV for films selenized with evaporated KF, which is attributed to the K $2p_{3/2}$ photoelectron transition; associated Voigt peaks are also shown on Figure 3.7. Despite observing K on the surface of the 10 nm KF sample through XPS and the enhanced solar cell performance (see Solar Cell Performance section), we were not able to identify the Se-3 state with certainty in the Se 3d XPS core level spectrum for the 10 nm KF sample.

The indicated alkali amounts show the alkali that was added to the film prior to selenization. However, the films are deposited onto Mo-coated soda-lime glass so some Na diffusion
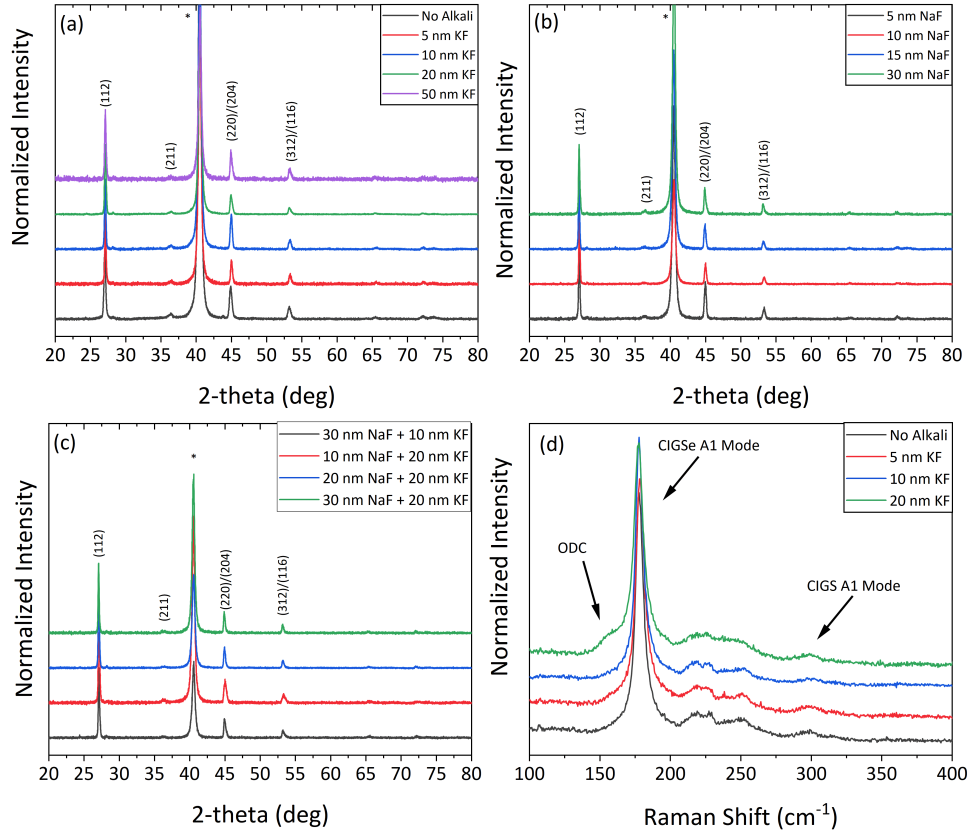
Figure 3.5. (a), (b), and (c): Powder X-ray diffraction patterns of $Cu(In, Ga)(S, Se)_2$ selenized at 500 C and 20 minutes with (a) with no alkali addition, 5 nm KF, 10 nm KF, and 20 nm KF; (b) 5, 10, 15, 30 nm NaF; and (c) 30 nm NaF+10 nm KF, 10 nm NaF+20 nm KF, 20 nm NaF+20 nm KF, and 30 nm NaF+20 nm KF. (d): Raman spectra of CIGSSe films selenized at 500 C for 20 minutes with no alkali addition, 5 nm KF, 10 nm KF, and 20 nm KF. The asterisk in (a), (b), and (c) denotes Mo (110) peak.

from the glass is expected. Figure 3.8 shows the Na 1s XPS transitions. The No Alkali sample shows the lowest Na 1s peak intensity, with the 15 nm NaF unsurprisingly showing higher Na 1s intensity. The KF-only films (10 nm KF, 20 nm KF, and 25 nm KF) were not subjected to any external Na treatment and were selenized at the same temperatures and for the same duration as the other samples, with the only Na source for the KF-only samples being the SLG substrate. We would then expect the same amount of Na on the surface for the No Alkali and KF-only conditions. However, what we found was that the signal intensity of the Na 1s peak was higher for the 20 nm KF and the 25 nm KF conditions compared to the No Alkali condition. The fact that the only Na source is the SLG substrate and that
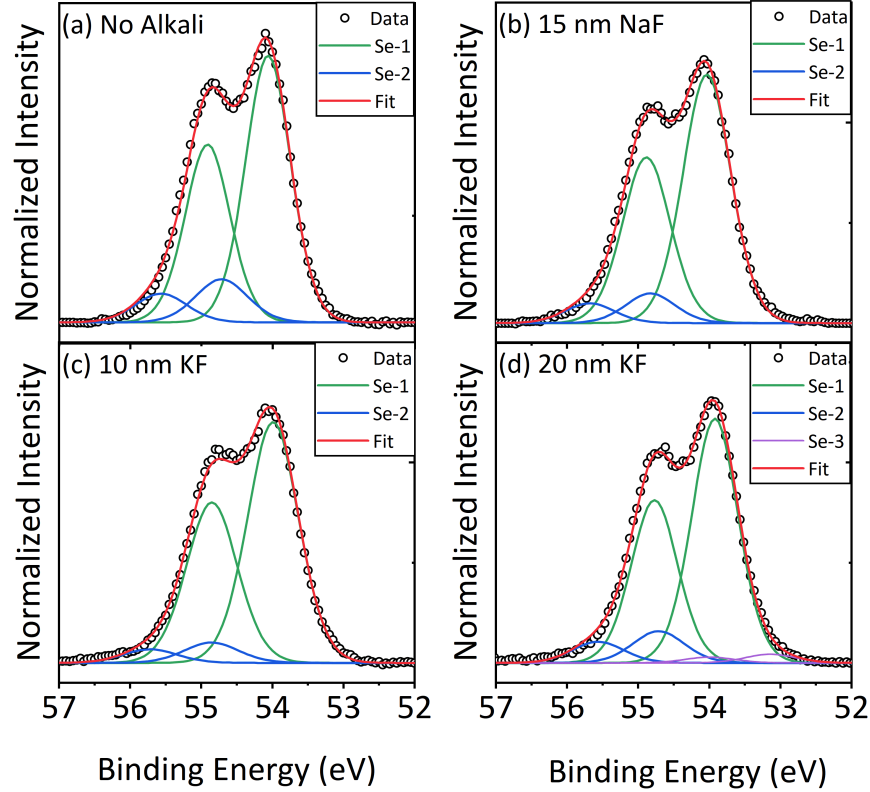
Figure 3.6. Normalized Se 3d XPS transitions of CIGSSe films selenized at 500 °C for 20 minutes with (a) no alkali added, with (b) 15 nm NaF, (c) with 10 nm KF, and (d) with 20 nm KF. When fitting the Se 3d doublet contribution, the Se $3d_{5/2}$ and $3d_{3/2}$ doublet separation was set at 0.86 eV.

the intensity of the Na 1s signal correlates with the amount of KF evaporated on the film suggests that K aids in the out-diffusion of Na from the glass substrate. Similar behavior was reported for Li-doped solution-processed CZTSSe films in which films with Li added to the ink showed more Na diffusion from the glass through an ion-exchange mechanism [118].

Figure 3.9 shows the normalized Cu $2p_{3/2}$, In $3d_{5/2}$, and Ga $2p_{3/2}$ XPS transitions for CIGSSe films selenized at 500 °C for 20 minutes with various alkali contents. Slight attenuation of the Cu $2p_{3/2}$ is observed with samples selenized with alkali fluorides evaporated prior to selenization (15 nm NaF, 10 nm KF, and 20 nm KF) compared to the No Alkali baseline condition. However, this attenuation is much less than what is reported in the literature for CIGSe grown with the 3-stage process where almost complete removal of Cu from the surface is observed [12], [73]. Furthermore, a minor attenuation is also observed for Ga for
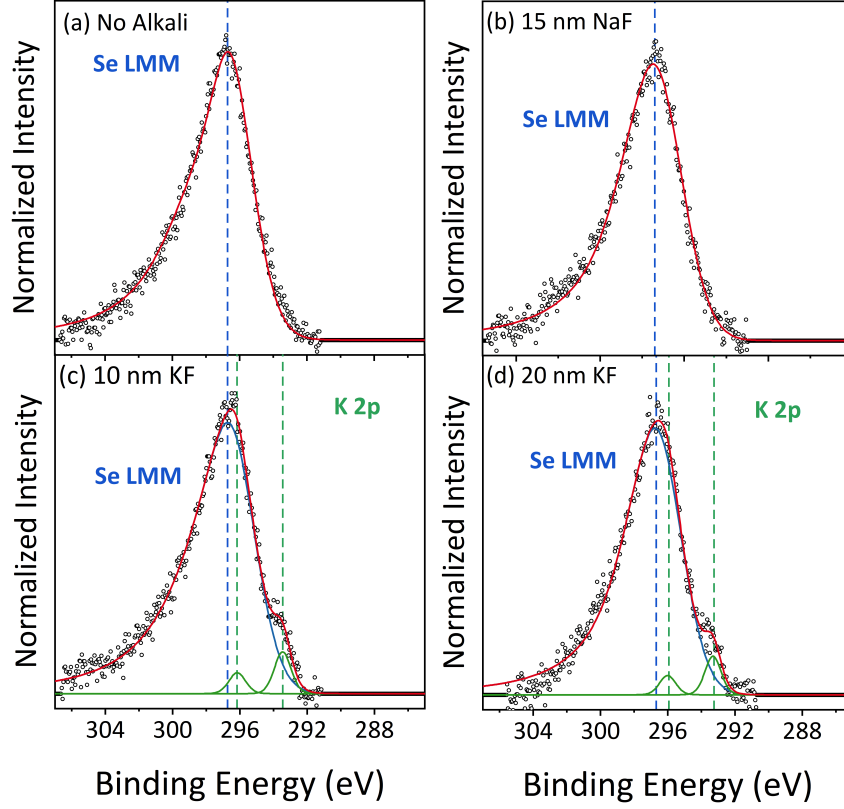
Figure 3.7. Normalized Se LMM Auger transition and K 2p photoelectron transitions of CIGSSe films selenized at 500 °C for 20 minutes with (a) no alkali added, (b) with 15 nm NaF, (c) with 10 nm KF, and (d) with 20 nm KF. K 2p doublet separation is set at 2.70 eV. K 2p peak is fitted with a Voigt profile, while the Se LMM Auger transitions was fitted with an asymmetric peak.

the 15 nm NaF and 20 nm KF conditions, as shown in the Ga $2p_{3/2}$ XPS core level transition on Figure 3.9. The Ga attenuation is also much less than in KF-PDT CIGSe absorber films made using the 3-stage process [12], [73], [74]. A post-selenization K treatment may be necessary to induce Cu and Ga depletion from the surface. Section 3.5 will discuss results related to post-selenization potassium treatments.

3.4 Solar Cell Performance

Devices were completed for the CIGSSe films that were selenized with the different alkali contents and the results are tabulated in Table 3.1. Figure 3.10 (a) shows the light J-V
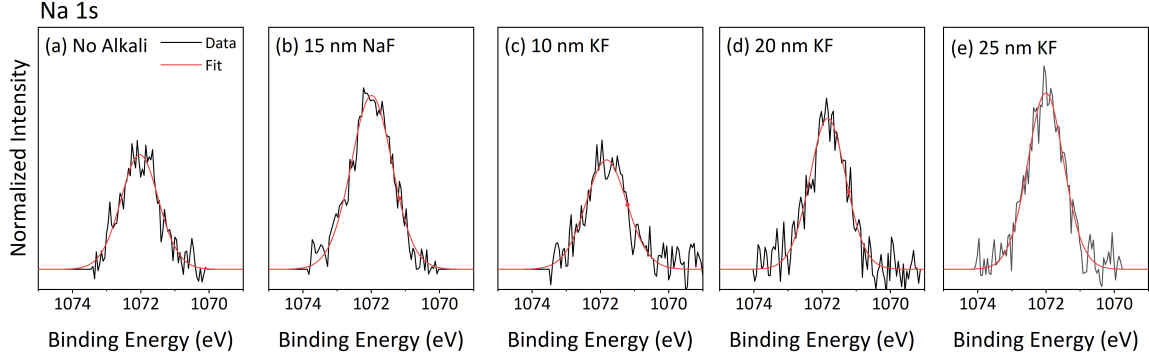
Na 1s

Figure 3.8. Normalized Na 1s XPS core-level spectra of CIGSSe films selenized at 500 °C for 20 minutes with (a) no alkali added, with (b) 15 nm NaF, (c) with 10 nm KF, and (d) with 20 nm KF. All spectra are area-normalized to Se 3d of each respective sample.
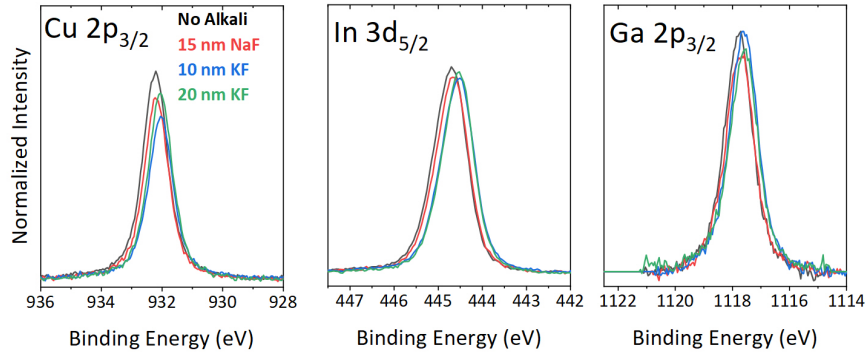
Figure 3.9. Cu $2p_{3/2}$, In $3d_{5/2}$, and Ga $2p_{3/2}$ XPS photoemission spectra of selenized CIGSSe films with no alkali added, 15 nm NaF, 10 nm KF, and 20 nm KF. All spectra are area-normalized to Se 3d of each respective sample.

curves of films that were subjected to a pre-selenization KF treatment only. A significant increase in power conversion efficiency (p.c.e.) is observed, increasing from 8.8% for the No Alkali condition to 11.3% with only 10 nm KF, and to 11.2% for the 20 nm KF condition. The p.c.e. drops to 5.5% for the 50 nm KF condition. The major increase in efficiency is attributed to significant increase in the open circuit voltage V_{oc} from 0.56 V for the No Alkali condition to 0.62 V for both 10 nm KF and 20 nm KF condition. Moreover, the 50 nm KF case exhibited an increased V_{oc} of 0.61 V over the No Alkali condition. We also observed an increase in the short circuit current density J_{sc} from 24.3 mA/cm^2 for the No Alkali case to 27.6 mA/cm^2 and 27.8 mA/cm^2 for the 10 nm KF and 20 nm KF cases, respectively; the 50

nm KF condition also had an increase in J_{sc} to 27.2 mA/cm^2 without a MgF$_2$ anti-reflective coating. The fill factor showed a slight increase to 66% and 64.8% for the 10 nm KF and 20 nm KF conditions, respectively, compared to 64.4% the No Alkali condition. The drop in efficiency for the 50 nm KF is due to the significant drop in FF (33.3%). The reason for the drastic drop in FF for the 50 nm KF case is not entirely clear at this point, but barrier formation as a result of excess K is suspected. Formation of a barrier for injection current has been shown to form as a result of KF-PDT [119]. Moreover, current barrier formation has also been observed for CIGSe films treated with excess Rb [75], [120], [121]. To further explore the effect of alkali on the performance of nanoparticle-based CIGSSe, we
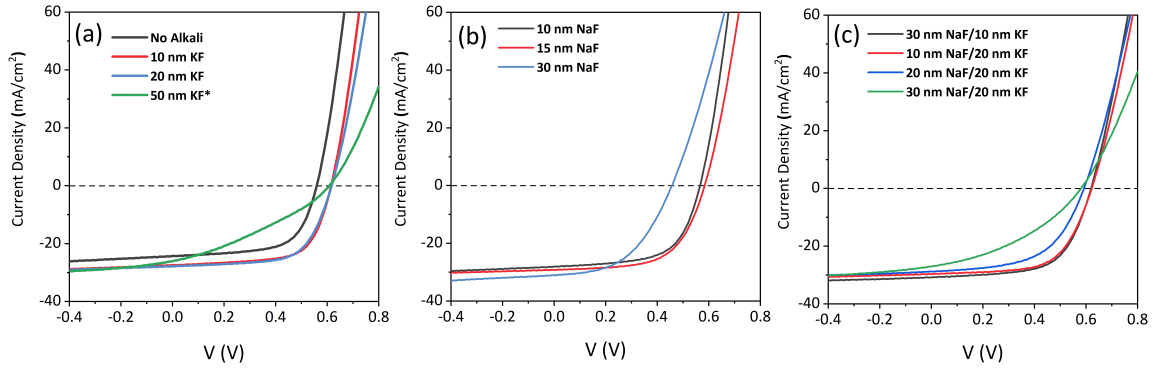
Figure 3.10. Illuminated J-V curves of champion CIGSSe devices with (a) different KF amounts, (b) different NaF amounts, and (c) different NaF/KF combinations. The alkali fluoride thicknesses given correspond to the evaporated thickness onto the nanoparticle film prior to selenization. * denotes samples without MgF$_2$ anti-reflective coating.

also fabricated devices with different NaF treatments prior to selenization. Figure 3.10 (b) shows the light JV curves for NaF-treated devices. An increase in the p.c.e. is also observed with Na, but less drastic than KF-treated films, with an increase in the p.c.e. to 9.3% and 10.7% for the 10 nm NaF and 15 nm NaF, respectively. The increase in V_{oc} is more subtle for the NaF-treated films than the K-treated films, with an increase to 0.59 V for the 15 nm NaF case only. A decrease in FF with increasing NaF thickness is also observed, with the FF decreasing to 53.1% for the 30 nm NaF case which may be a consequence of the pinhole film morphology as seen in the SEM plan view images (Figure 3.2 (d)). The results

above suggest that KF treatments improves the V_{oc} more than NaF treatments, while NaF treatments are more effective in improving the J_{sc}.

CIGSSe solar cells were also fabricated with both NaF and KF treatments. Figure 3.10 (c) shows the light J-V curves for CIGSSe films subjected to both NaF and KF treatments. An efficiency boost was obtained for the cases of both NaF and KF were evaporated with a p.c.e. of 12.0% for the case in which 30 nm NaF+10 nm KF were evaporated prior to selenization. The 10 nm NaF+20 nm KF case also exhibited efficiency increase to 11.6%. Both of these conditions exhibited significant increases in both the V_{oc} and the J_{sc} as compared to the No Alkali case. A significant drop in FF is also observed with increasing alkali content for the NaF+KF cases, with the FF dropping to 55.7% and 36.7% for the 20 nm NaF+20 nm KF and the 30 nm NaF+20 nm KF conditions, respectively.

Table 3.1. Average performance parameters for CIGSSe devices selenized with the different alkali contents. * denotes devices without MgF_2 anti-reflective coating. Values in parentheses indicate parameters for champion devices. All efficiencies are based on total cell area.

Condition	η (%)	V_{OC} (V)	J_{sc} (mA/cm^2)	FF (%)
No Alkali	7.6 (8.8)	0.53 (0.56)	23.8 (24.3)	60.2 (64.4)
10 nm KF	10.1 (11.3)	0.61 (0.62)	25.9 (27.6)	63.6 (66.0)
20 nm KF	10.4 (11.2)	0.61 (0.62)	26.9 (27.8)	63.4 (64.8)
50 nm KF*	5.3 (5.5)	0.61 (0.61)	27.0 (27.2)	32.1 (33.3)
10 nm NaF	9.0 (9.3)	0.56 (0.57)	25.4 (25.6)	62.6 (64.4)
15 nm NaF	9.9 (10.7)	0.57 (0.59)	28.5 (29.2)	57.8 (62.3)
30 nm NaF	6.2 (8.1)	0.43 (0.49)	29.3(31.0)	48.7 (53.1)
30 nm NaF + 10 nm KF	11.3 (12.0)	0.62 (0.62)	28.8 (30.8)	63.5 (62.6)
10 nm NaF + 20 nm KF	11.1 (11.6)	0.62 (0.62)	30.1 (29.6)	59.0 (63.3)
20 nm NaF + 20 nm KF	9.0 (9.5)	0.58 (0.59)	29.0 (28.9)	52.9 (55.7)
30 nm NaF + 20 nm KF	5.3 (6.0)	0.59 (0.59)	26.9 (27.8)	35.0 (36.8)

Series and shunt resistances for champion cells of the different alkali conditions are tabulated in Table 3.2.

Figure 3.11 (a) shows EQE measurements performed at 0 V for KF-only and NaF+KF conditions, while Figure 3.11 (b) shows EQE measurements for NaF-only conditions. Increased EQE response is observed for KF-treated samples compared to the No Alkali baseline condition. Samples that were subjected to both NaF and KF treatments showed significantly

Table 3.2. Calculated series resistances and shunt resistances for champion CIGSSe solar cells selenized with different alkali contents. All parameters are calculated from the light J-V measurement and are based on total cell area.

Condition	R_{Series} ($\Omega \cdot cm^2$)	R_{Shunt} (kΩ cm^2)
No Alkali	0.81	0.22
10 nm KF	0.84	0.34
20 nm KF	1.11	0.33
50 nm KF	0.08	0.25
10 nm NaF	0.97	0.33
15 nm NaF	0.93	0.43
30 nm NaF	1.52	0.24
30 nm NaF + 10 nm KF	1.31	0.53
10 nm NaF + 20 nm KF	1.48	0.31
20 nm NaF + 20 nm KF	1.42	0.39
30 nm NaF + 20 nm KF	1.44	0.16

higher EQE performance than the bare KF and the baseline conditions. Moreover, the cut-off wavelength in the EQE vs. wavelength plots (Figure 3.11 (a) and Figure 3.11 (b)) is also altered for the different alkali cases suggesting slightly differing bandgaps between the different alkali cases. Figure 3.12 shows differential quantum efficiency data for each of the conditions considered [122]. A slight increase in the estimated effective bandgap is observed with alkali treated-devices (ca. 1.23 eV for the 10 nm KF condition) compared with the No Alkali baseline condition (ca. 1.20 eV). The estimated bandgaps from the differential quantum efficiency data are tabulated in Table 3.3.

Table 3.3. Estimated effective bandgaps for CIGSSe solar cells with different alkali contents extracted from of differential EQE data shown in Figure 3.12

Condition	Bandgap (eV)
No Alkali	1.2
10 nm KF	1.23
20 nm KF	1.24
10 nm NaF	1.22
15 nm NaF	1.22
30 nm NaF + 10 nm KF	1.22
10 nm NaF + 20 nm KF	1.22
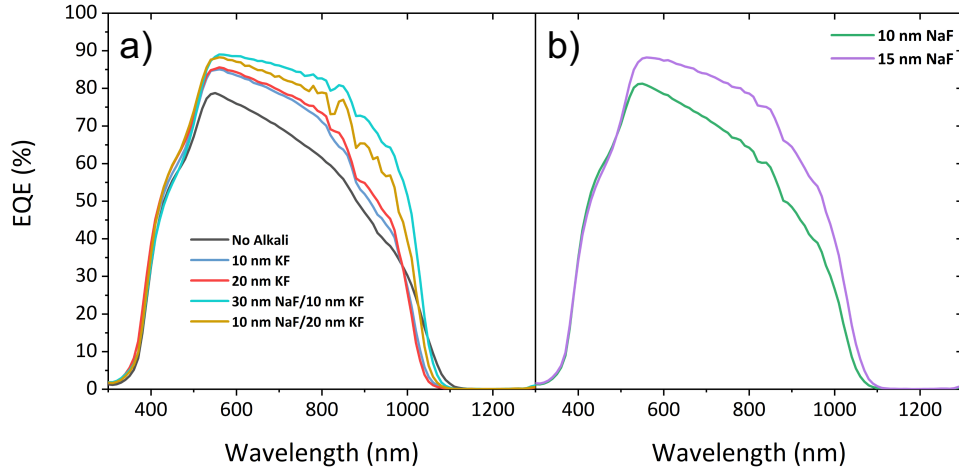
Figure 3.11. EQE measurements of champion CIGSSe devices selenized at 500 °C for 20 minutes with (a) no alkali addition, 10 nm KF, 20 nm KF, 30 nm NaF+10 nm KF, and 10 nm NaF+20 nm KF; (b) 10 nm NaF and 15 nm NaF.

It is apparent from inspection of EQE data in Figure 3.11 that the decay of EQE in the vicinity of the bandgap is different for the different alkali conditions considered. Application of an Urbach tail model to the EQE data allows characterization of the Urbach Energy E_U [122], [123]. The Urbach energy characterizes the magnitude of sub-bandgap absorption (band-tailing) in the film [122]. Figure 3.13 shows a plot of ln[-ln(1-EQE)] vs. Energy applied to EQE data for the different conditions considered; estimated Urbach energies extracted from the slope of ln[-ln(1-EQE)] vs. Energy plot in the sub-bandgap energy range are tabulated in Table 3.4. A reduction in band tailing is observed for films treated with alkali (Na and/or K) compared to the No Alkali baseline condition; E_U is reduced from 19.6 meV for the No Alkali case to 13.6-13.8 meV for the NaF and KF treated case. The results presented in Figure 3.13 and Table 3.4 suggest reduced defect formation and improvements in the bulk properties of the film as a result of alkali addition. Figure 3.14 (a) shows the apparent carrier concentration extracted from capacitance-voltage measurements for devices that were subjected to KF treatments and NaF+KF, while Figure 3.14 (b) shows the apparent carrier concentration for devices subjected to NaF treatment only. Despite the varying optoelectronic performance enhancements and increases in the open circuit voltage with Na and K treatments, little change in the absorber carrier concentration was observed. This
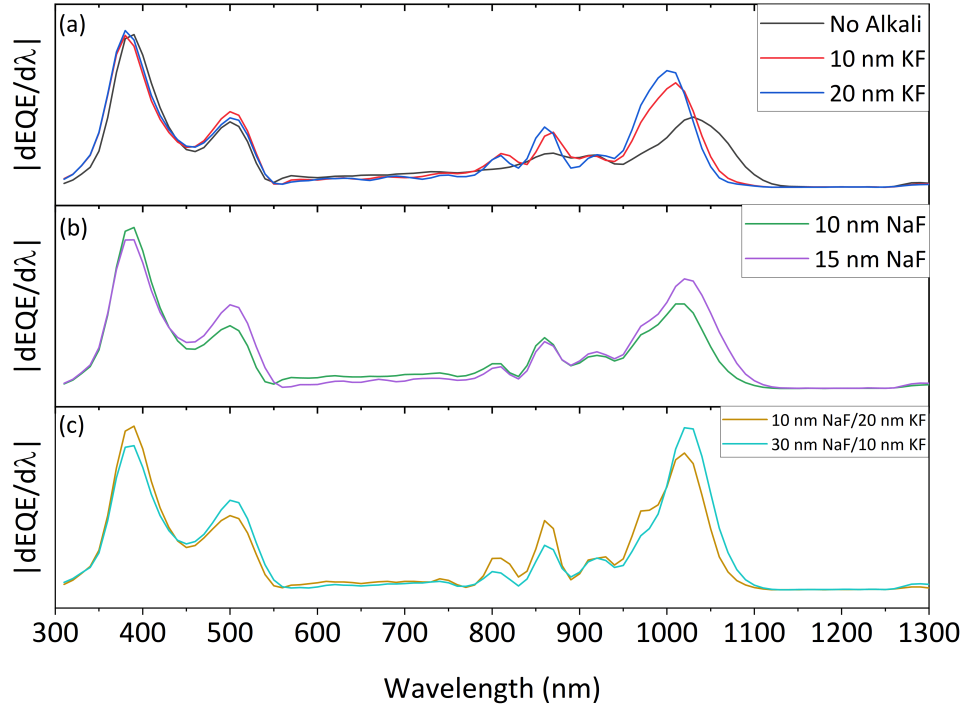
Figure 3.12. Plot of $|dEQE/d\lambda|$ vs. λ of CIGSSe solar Cells selenized with (a) KF only, (b) NaF only, and (c) NaF + KF.

agrees with multiple reports in the literature where the carrier concentration of solution-processed CISe [102], [124], and CIGSSe [54] is not influenced appreciably by Na. However, for vacuum-based CIGSe, increases in carrier concentration with Na and K treatments is widely reported [89], [95], [119].

3.5   Post Selenization Potassium Treatments

One of the beneficial effects of KF-PDT in vacuum-based CIGSe is that it induces the surface depletion of Ga and Cu [12]. This facilitates Cd diffusion into the CIGSSe film during CdS chemical bath deposition, and in practice allows a thinner CdS layer [12], [26]. During the chemical bath deposition of CdS onto a CIGSSe film, Cd diffuses into the CIGSSe surface and occupies V_{Cu} causing a type-inversion in the surface from p-type into n-type thus forming a buried homojunction (with the n-type CdS); Cd_{Cu} defects are donor type [12]. In the previous sections, it was shown that the CIGSSe films that were selenized with KF-evaporated prior to selenization (Figure 3.9), the attenuation in Cu (10 nm KF and 20 nm
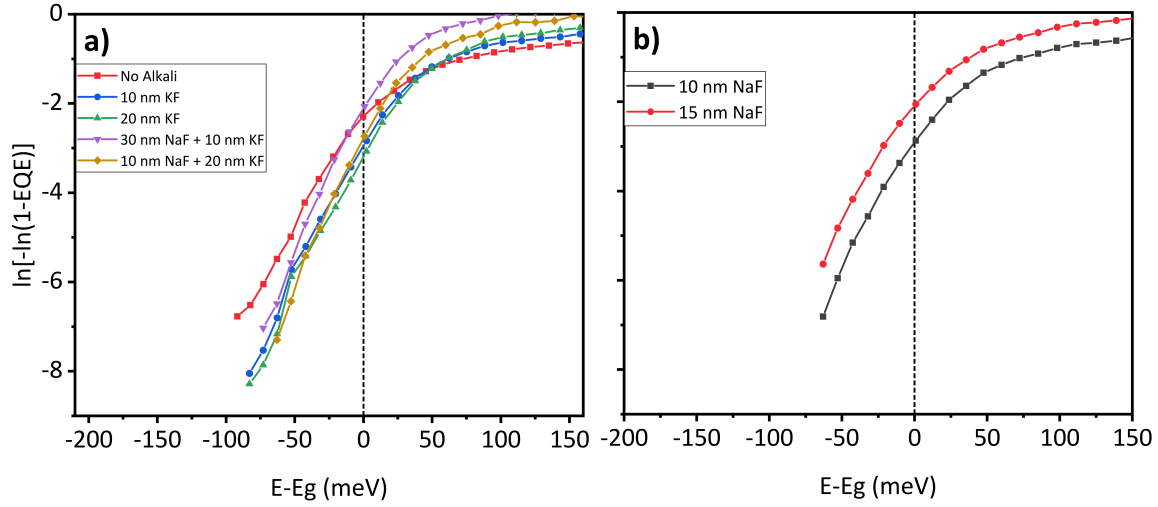
Figure 3.13. Plot of ln[-ln(1-EQE)] vs. E-Eg for CIGSSe solar cells selenized with (a) different KF and NaF+KF thicknesses, and (b) different NaF thicknesses.

Table 3.4. Urbach tail energy extracted from Figure 3.11 for CIGSSe solar cells selenized with different alkali contents.

Condition	E_U (meV)
No Alkali	19.6
10 nm KF	18.8
20 nm KF	15.5
10 nm NaF	15.9
15 nm NaF	17.1
30 nm NaF + 10 nm KF	13.8
10 nm NaF + 20 nm KF	13.6

KF conditions), and with Ga (20 nm KF condition) is significantly less than what is seen for CIGSe films grown with the three-stage process and subjected to a KF PDT [12], [73]; in vacuum-based CIGSSe, potassium treatments are typically done after film formation and growth through a post-deposition treatment at 250-350 °C under Se atmosphere [12], [26], [74], [75]. A potassium post-deposition treatment may be a necessary condition to induce Ga and/or Cu surface depletion.

To investigate if this is the case, a number of CIGSSe devices were fabricated: The first is a CIGSSe film that was selenized twice at 500 °C for 20 minutes, with no external alkali

Figure 3.14 panel a table:

Alkali	Ncv cm⁻³	Width nm
No Alkali	2.77E+16	175
10 nm KF	2.08E+16	170
20 nm KF	2.09E+16	177
50 nm KF	2.98E+16	100
10 nm NaF+10 nm KF	1.74E+16	199
30 nm NaF+10 nm KF	2.54E+16	161
10 nm NaF+20 nm KF	1.97E+16	179

Figure 3.14 panel b table:

Alkali	Ncv cm⁻³	Width nm
10 nm NaF	2.05E+16	184
15 nm NaF	2.35E+16	165
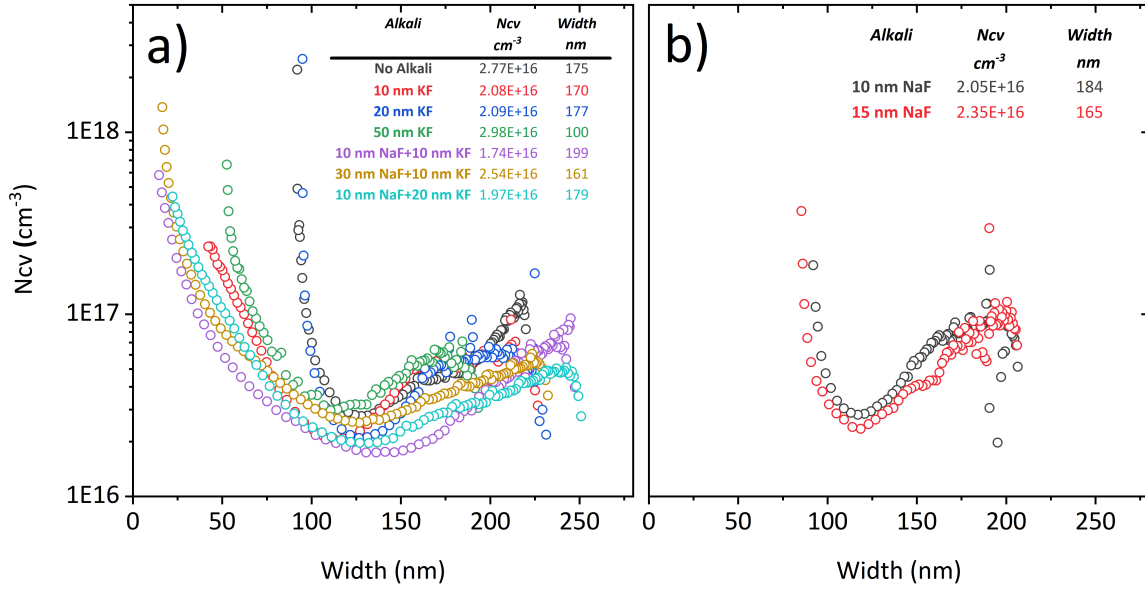
Figure 3.14. Apparent carrier concentration vs. width from capacitance-voltage measurements of CIGSSe devices selenized with (a) different KF thicknesses and different NaF+KF thicknesses; (b) different NaF thicknesses. Tabulated N_{cv} values are taken at the minimum of each N_{cv}-Width curve, and the Width is taken at the 0 V point.

treatment in either selenizations (2x CIGSSe); this will be the control sample. the second is a CIGSSe film that was first selenized without external alkali treatment (500 °C, 20 minutes), and then had 20 nm KF evaporated on it via e-beam evaporation, and then selenized again for 20 minutes at 500 °C (KF 2x CIGSSe). The third is a CIGSSe film selenized at 500 °C for 20 minutes without external alkali, and then underwent a 20 nm KF-evaporation via e-beam followed by annealing the film at 300 °C under a Se atmosphere (20 nm KF PDT). The fourth is a CIGSSe film selenized at 500 °C for 20 minutes without 10 nm NaF evaporated before selenization, and then underwent a 20 nm KF-evaporation via e-beam followed by annealing the film at 300 °C under a Se atmosphere (10 nm NaF + 20 nm KF PDT). Table 3.5 summarizes the selenization conditions for the four films. It is worth noting that the post-selenization treatment conditions discussed here are not optimized for optimal device performance. The main goal of this section was to determine if a post-selenization (PDT) treatment is a necessary condition to induce the Cu and Ga surface depletion effects. The consequence of having a Cu-depleted surface is allowing a thin CdS layer to be deposited

with sacrificing V_{OC} or *FF*, while benefiting from increased light absorption in the CIGSSe film, as discussed in Chapter 2.

Table 3.5. Summary of CIGSSe Selenization Conditions with Post-Selenization Treatments. After the First Stage Annealing, the film is naturally cooled to room temperature under inert Ar atmosphere. In both stages, the films are annealed in a Se-rich atmosphere.

CIGSSe Film	First Stage Annealing		Second Stage Annealing	
	Alkali Amount	Conditions	Alkali Amount	Conditions
2x CIGSSe	No Alkali	500 °C, 20 minutes	No Alkali	500 °C, 20 minutes
KF 2x CIGSSe	No Alkali	500 °C, 20 minutes	20 nm KF, e-beam	500 °C, 20 minutes
20 nm KF PDT	No Alkali	500 °C, 20 minutes	20 nm KF, e-beam	300 °C, 20 minutes
10 nm NaF + 20 nm KF PDT	10 nm NaF, e-beam	500 °C, 20 minutes	20 nm KF, e-beam	300 °C, 20 minutes

To investigate the effects the conditions shown in Table 3.5 have on the CIGSSe film morphology, SEM imaging on the films after the alkali post-annealing. Figure 3.15 shows SEM plan view and cross-sectional images for the KF 2x CIGSSe, 20 nm KF PDT, and 10 nm NaF + 20 nm KF PDT films. All films are characterized by the bilayer morphology seen with selenization of oleylamine-containing nanoparticles, with coarsened film on the surface, and a fine-grain layer at the bottom. The overall grain size is largest for the 10 nm NaF + 20 nm KF PDT, followed by the KF 2x CIGSSe and the 20 nm KF PDT. The reason for the differences in grain size in the 10 nm NaF + 20 nm KF PDT film is attributed to the Na present during the first stage (Table 3.5). Furthermore, the KF 2x CIGSSe film showed markedly larger grain sizes than the 20 nm KF PDT film (Figure 3.15 (a),(d) and (b),(e)), even though both films underwent the same first stage annealing (500 °C. 20 minutes, no external alkali). This result suggests that during the second stage, the KF 2x CIGSSe film did undergo further grain growth at 500 °C, 20 minutes, whereas the 20 nm KF PDT film underwent the second stage at a significantly lower temperature.
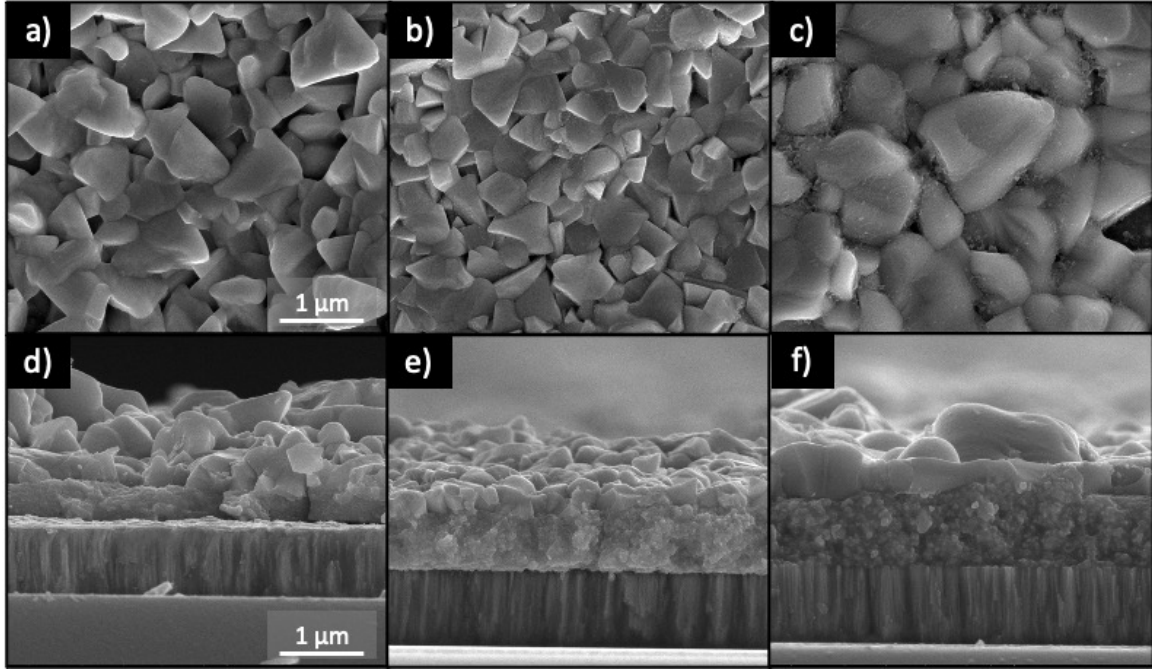
Figure 3.15. SEM plan view (a)-(c) and cross-sectional (d)-(f) images of the CIGSSe films given in Table 3.5: (a),(d) KF 2x CIGSSe; (b),(e) 20 nm KF PDT; and (c),(f) 10 nm NaF + 20 nm KF PDT. Scale bar is same for all images.

Figure 3.16 shows the Cu $2p_{3/2}$, Ga $2p_{3/2}$, and Na 1s XPS core level spectra for the KF 2x CIGSSe, 20 nm KF PDT, and the 10 nm NaF + 20 nm KF PDT films; for comparison, the XPS core level spectra of the No Alkali baseline condition film shown in Figures 3.8 and 3.9 is also included in Figure 3.5. Taking the No Alkali case as a control sample, a slight attenuation in the Cu $2p_{3/2}$ peak intensity is observed for the KF 2x CIGSSe sample, which is similar to the attenuation observed in the 20 nm KF film shown in Figure 3.9. Moreover, the Ga $2p_{3/2}$ signal is also slightly attenuated with respect to the No Alkali film; the amount of attenuation is also similar to the 20 nm KF sample in Figure 3.9. As for the 20 nm KF PDT film, a significant attenuation in both Cu $2p_{3/2}$ and Ga $2p_{3/2}$ XPS signal is observed, which is consistent with reports in the literature regarding CIGSe films that undergo a KF-PDT process [26], [73], [74], [125]. A similar observation can also be seen for the 10 nm NaF + 20 nm KF PDT sample, which is also characterized by an attenuated Cu $2p_{3/2}$ and Ga $2p_{3/2}$ XPS signals.

XPS is a surface analysis technique, and the spectra shown in Figure 3.16 represent the film surface. However, XPS does not provide information on the bulk, i.e. the Cu and Ga signal attenuation may be a result of the bulk of the film being depleted of Cu and Ga, not just the surface. To determine if that is the case, the elemental composition in the bulk of the PDT films is measured using XRF, and the CGI and GGI ratios were 0.86 and 0.26 $\pm$ 0.002, respectively; the CGI and GGI ratios of the nanoparticle films prior to the first stage annealing were 0.92 $\pm$ 0.02, and 0.27 $\pm$ 0.01, respectively. This indicates that the Cu and Ga depletion observed in the XPS spectra are representative of the surface only, and that the bulk of the film is not affected. The aforementioned results suggest that to obtain a surface depletion of Cu (needed for thinning the CdS layer [12], [26]), a potassium post-selenization treatment at low temperature, e.g. 300 °C, is necessary.

Figure 3.16 (c) shows the Na 1s XPS core level spectra for the KF 2x CIGSSe, 20 nm KF PDT, and the 10 nm NaF + 20 nm KF PDT films, along with the No Alkali film for reference. The Na 1s peak intensity for the KF 2x CIGSSe film is comparable to the No Alkali baseline condition indicating that the amount of Na on the surface of both films is comparable. Films that were subjected to a post selenization potassium treatments, i.e., films that were annealed at 300 °C after their K treatment, showed no detectable Na on the surface. This is in contrast to films that were treated with K prior to selenization (Figure 3.8). In Section 3.4 and in Figure 3.8, it was argued that addition of K prior to selenization causes more Na to diffuse from the SLG substrate during selenization at 500 °C, and that the amount of Na on the selenized film surface commensurate with the amount of K evaporated on the nanoparticle film prior to selenization. However, this is not the case for the PDT films where even the film that was selenized with 10 nm NaF evaporated prior to the first stage annealing showed no Na on the surface. The reason for this behavior may be due to the phase that K forms with In and Se on the surface, and that the low temperature at which the PDT films are annealed at compared to the selenization temperature (300 °C vs. 500 °C) decreases the Na diffusion towards the surface. Three-stage co-evaporated CIGSe films that undergo a KF PDT process also show minimal Na on the surface [74].

Figure 3.17 (a) shows the In $3d_{5/2}$ XPS core level spectra for the films shown in Table 3.5. A surface enrichment of In is observed the PDT films (20 nm KF PDT and 10 nm NaF
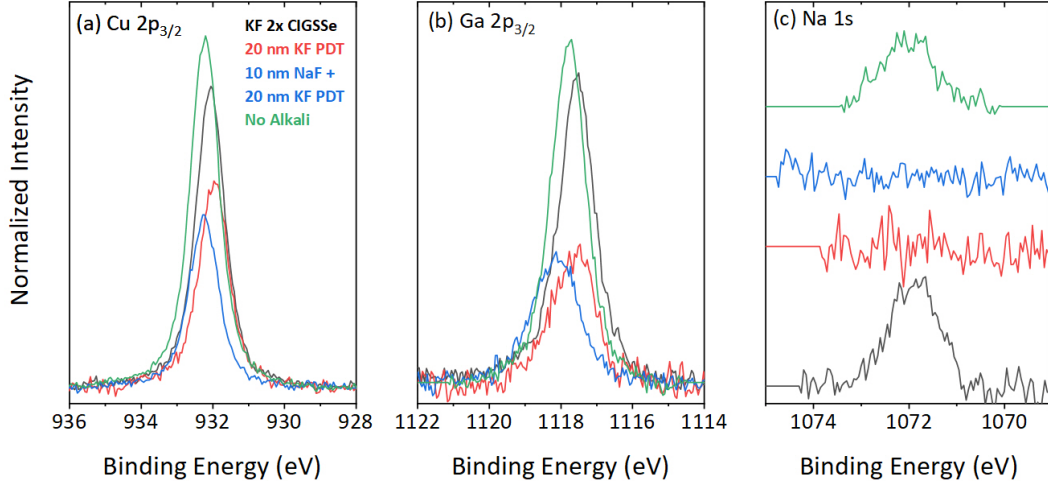
Figure 3.16. Elemental XPS core level spectra for 2x CIGSSe, 20 nm KF PDT, 10 nm NaF + 20 nm KF PDT CIGSSe films. (a) Cu $2p_{3/2}$, (b) Ga $2p_{3/2}$, and (c) Na 1s. The Na 1s spectra for the different films are shifted for clarity. The XPS spectra for the No Alkali CIGSSe film is also provided for reference. All spectra are normalized to the Se 3d peak area of each respective sample.

+ 20 nm KF PDT), compared to the KF 2x CIGSSe and the No Alkali condition baseline condition, which is attributed to the Ga depletion observed for the PDT films. Moreover, for both of the PDT samples, a shift towards higher binding energies in the In $3d_{5/2}$ peak position can also be observed, with the peak shape skewed indicating the presence of more than one In state on the surface. Voigt peak fitting on the In $3d_{5/2}$ for the 20 nm KF PDT and 10 nm NaF + 20 nm KF PDT films show that the In $3d_{5/2}$ XPS core level spectrum is composed of two peaks: In-1 and In-2, as shown in Figure 3.17 (a). In-1 is present in all four films shown in Figure 3.17, and is attributed to the indium in the chalcopyrite chemical environment [74]. The additional In-2 peak present in the PDT films is attributed to the formation of an In-oxide species on the surface of the film. Nicoara et al. have shown that K or KF post-deposition treatment induces rapid oxidation of co-evaporated CIGSe surface forming a stable In_xO_y on the surface of the film, and that further oxidation of the surface is not sensitive to air exposure time [125]. To further confirm the presence of an In-oxide species on the surface of the PDT films, Figure 3.17 (b) shows the O 1s XPS core level spectra for the films described in Table 3.5. All films have oxygen signals at $\sim$ 531.5 - 533 eV binding energies, which is attributed to organics [74], [126]. The PDT films also exhibit

an additional oxygen peak at ~ 530 eV, which is indicative of a metal-oxide species [74]. The intensity of the metal-oxide XPS peak commensurate with the intensity of the In-2 peaks observed in Figure 3.17 (a), that is, the 20 nm KF PDT has the strongest intensity in both the In-2 and the metal oxide peaks. These two observations combined further confirm that the In-2 peak observed is due to an In-oxide species.
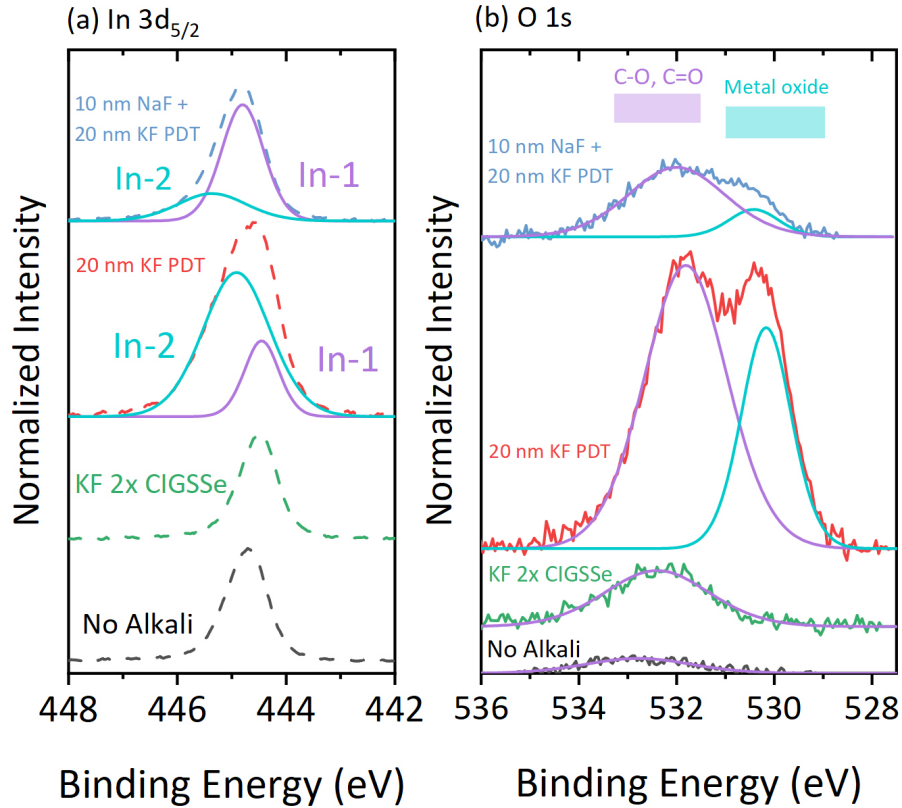
Figure 3.17. Elemental XPS core level spectra for 2x CIGSSe, 20 nm KF PDT, 10 nm NaF + 20 nm KF PDT CIGSSe films. (a) In $3d_{5/2}$ and (b) O 1s. The XPS spectra for the No Alkali CIGSSe film is also provided for reference. All spectra are normalized to the Se 3d peak area of each respective sample.

Figure 3.18 shows the Se 3d XPS core level spectra for the KF 2x CIGSSe, 20 nm KF PDT, and the 10 nm NaF + 20 nm KF PDT films, along with Voigt peak fitting. All three films show the presence of three Se states (three doublets), similar to CIGSe film that was subjected to 20 nm KF prior to selenization shown in Figure 3.6, with Se-1 and Se-2 attributed to Se in the chalcopyrite chemical environment [26], [117], and the low-binding energy Se-3 state attributed to the K-In-Se phase [26], [73], [81].
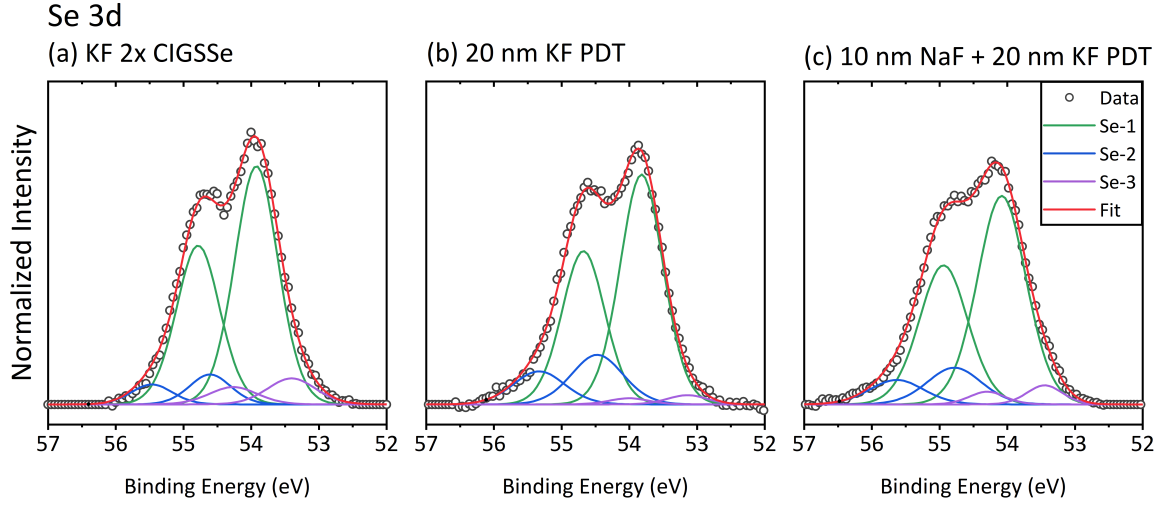
Figure 3.18. Se 3d XPS core level spectra along with fitted Voigt peaks for (a) 2x CIGSSe, (b) 20 nm KF PDT, and (c) 10 nm NaF + 20 nm KF PDT CIGSSe films. All spectra are normalized to Se 3d peak area.

3.5.1 K-PDT Device Performance

CIGSSe devices were fabricated with the CIGSSe films subjected to the conditions shown in Table 3.5 using the standard Mo/CIGSSe/CdS(50 nm)/i-ZnO(80 nm)/ITO(220 nm)/Ni-Al, with the illuminated J-V curves shown in Figure 3.19, and performance parameters summarized in Table 3.6. No MgF$_2$ anti-reflective coating is applied to any of the films.

The 2x CIGSSe device, selenized twice without alkali addition in either selenization, had a p.c.e. of 8.81%, which is expected for a solution-processed CIGSSe device selenized without any external alkali addition. On the other hand, the films that had KF evaporated onto them showed poorer performance, characterized mainly by a much lower fill factor. The KF 2x CIGSSe had comparable V_{OC} and J_{sc} to the 2x CIGSSe film, but much lower FF. The PDT samples (20 nm KF PDT and 10 nm NaF + 20 nm KF PDT) performed poorly, with η around 4.5-5%, and are characterized by much lower J_{sc}, compared to both non-PDT films.

The post-selenization CIGSSe devices represent preliminary and un-optimized PDT conditions for the nanoparticle-based CIGSSe devices. Further optimization is required, especially as KF-PDT effects on CIGSSe device performance is known to be extremely sensitive to the conditions at which the treatment is done [74], [96]. This remains an area of future study.
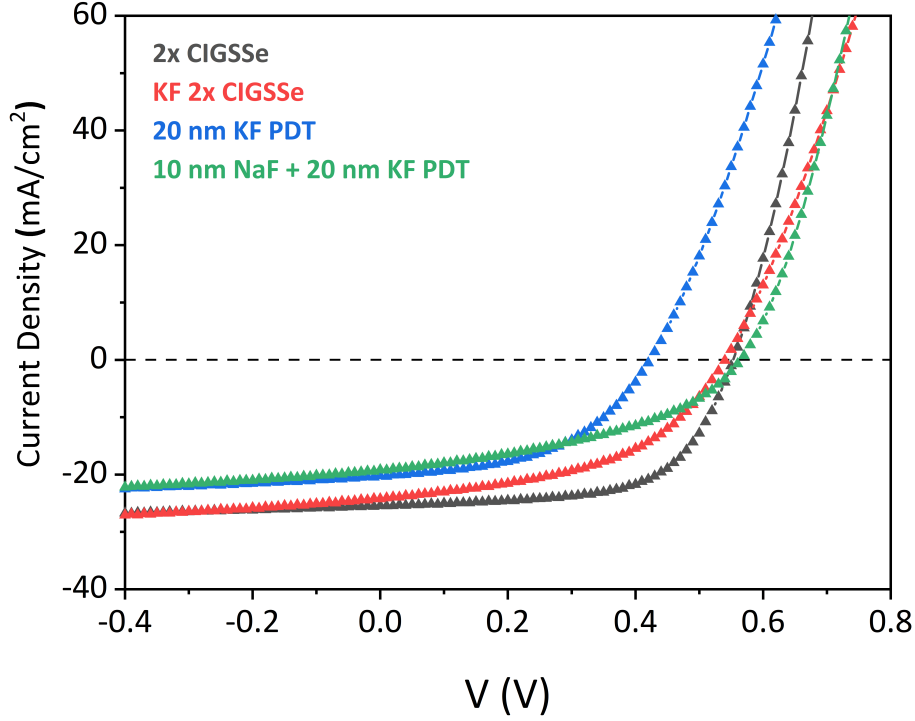
Figure 3.19. Illuminated J-V curves for champion CIGSSe devices selenized according to conditions given in Table 3.5. All devices are measured without MgF$_2$ anti-reflective coating.

3.6 Conclusion

In this work, the effect of pre-selenization alkali treatments on nanoparticle-based solution-processed CIGSSe solar cells was investigated. It was determined that both sodium and potassium enhance CIGSSe grain growth and lead to an increase in coarsened film thickness and a thinner fine-grain material. Additionally, through the use of XPS surface analysis, the presence of an additional Se chemical state at low binding energies was observed for CIGSSe film that had 20 nm KF deposited on prior to selenization, and the film that had undergone a KF post-selenization treatment. This additional Se state is attributed to a K-In-Se surface phase commonly seen in films grown via the 3-stage process and subjected to a KF-PDT. On the other hand, surface Ga and Cu depletion commonly seen in vacuum-based CIGSe films with KF PDT was not observed in films that were selenized with KF added *a priori*, and that a post-selenization potassium treatment, with annealing at low temperatures ($\sim$ 300 °C) is a necessary condition to induce Cu and Ga surface depletion.

Table 3.6. Performance parameters for champion CIGSSe devices selenized with conditions given in Table 3.5. All parameters are measured without a MgF_2 anti-reflective coating, and are based on total cell area (0.47 cm^2, nominal).

CIGSSe Film	η (%)	V_{OC} (V)	J_{sc} (mA/cm^2)	FF (%)
2x CIGSSe	8.81	0.55	25.3	63.2
KF 2x CIGSSe	6.54	0.54	25.1	48.2
20 nm KF PDT	4.44	0.43	20.7	49.8
10 nm NaF + 20 nm KF PDT	4.92	0.57	20.4	42.4

CIGSSe solar cell optoelectronic performance was found to be significantly enhanced with KF-treatments, with the performance increases being mainly in the open circuit voltage, and to lesser degree in the short-circuit current. Likewise, we also found the Na also enhances CIGSSe device performance by mainly enhancing the short circuit current density. Evaporating both NaF and KF on the as-coated CIGS nanoparticle film, we were able to enhance the performance of CIGSSe solar cell by increasing the power conversion efficiency from 8.8% to 12.0%. In contrast with vacuum-based CIGSe devices, we observed little or no change in the carrier concentration with respect to alkali content in the film. These results demonstrate that KF-treatments and NaF + KF treatments provide an avenue to enhancing the optoelectronic performance of solution-processed CIGSSe solar cells.

4. MORPHOLOGICAL AND EFFECTS OF POTASSIUM CYANIDE TREATMENTS ON NANOPARTICLE-BASED CIGSSE FILMS

4.1 Introduction

In Chapter 3, the effect of potassium on nanoparticle-based CIGSSe films and devices was analyzed in terms of grain morphology, surface chemistry, and optoelectronic performance. In this chapter, effects of potassium cyanide treatments on the CIGSSe films is presented. Similarly to the Chapter 3, the CIGSSe films analyzed in this chapter are selenized from OLA-capped CIGS nanoparticle films.

Potassium cyanide treatments have been used widely in CIGSe and CIGSSe processing, both in vacuum-based [14] and in solution-processed films [47], [54]. The main action of KCN treatments on CIGSe (CIGSSe) films is to etch binary Cu_2Se_x that formed during CIGSSe film growth. During CIGSe film growth, formation of Cu_2Se_x, along with α-phase $Cu(In, Ga)Se_2$, is thermodynamically favorable when the Cu content is close to stoichiometry. A Cu-poor film is needed to obtain phase-pure α-$Cu(In, Ga)Se_2$ [19]. However, the development of the three-stage process and the use of Cu-poor stoichiometry has made KCN treatments redundant for vacuum-based CIGSe (CIGSSe). As for solution-processed nanoparticle-based CIGSSe, Guo et al. treated the precursor sulfide CIGS nanoparticle films (synthesized with stoichiometric elemental ratios) with KCN on the as-coated film prior to selenization to remove binaries and render the films Cu-poor; performance enhancements were observed with devices that were subsequently made from KCN-treated nanoparticle films [54]. The enhanced device performance of the KCN-treated films was attributed to the Cu deficiency caused by the KCN treatment, and thus the thermodynamics of the selenization reaction is shifted away from the formation of binary Cu_2Se_x [54]. However, McLeod et al. have observed performance enhancements due to KCN treatments with sulfide nanoparticles that were synthesized Cu-poor ([Cu]/[In]+[Ga] = 0.89) [47], [127]. Despite those improvements in solution-processed CIGSe (CIGSSe) films and devices with KCN treatments, the

specific effects of KCN on the growth and performance of CIGSSe devices selenized from sulfide CIGS nanoparticles is not clear from the available literature. In this section, the action of KCN is investigated further to ascertain the specific effects of KCN, and whether it is needed in nanoparticle-based CIGSSe devices.

4.2 Experimental

OLA-capped CIGS nanoparticle films were coated using Cu-poor CIGS nanoparticles ([Cu]/[In]+[Ga] = 0.92) for a total of two coating passes, followed by annealing at 300 °C for 1 minute after each pass, as described in the experimental section. After each film anneal, the nanoparticle film was soaked in a KCN solution. Three different KCN solution concentrations were tested: 0.25 M, 0.5 M, and 1.0 M. For each concentration, three different etching durations were tested: 1 minute, 2 minutes, and 5 minutes. Furthermore, an additional nanoparticle film was etched with KCN (0.5 M, 2 minutes) and subsequently treated with 10 nm KF evaporated via e-beam (KCN + 10 nm KF); both treatments were done on the nanoparticle film prior to selenization.

Unless otherwise noted, selenization was conducted in a tubular furnace at 500 °C for 20 minutes. CIGSSe devices were fabricated using similar methods as in Chapter 3. No MgF_2 anti-reflective coating was applied.

Raman spectroscopy data was collected at room temperature using a Horiba/Jobin Yvon HR800 confocal microscope (633 nm laser excitation, 50x objective lens). Elemental compositions were measured via X-ray fluorescence using a Fischerscope XAN-250 XRF.

4.3 Results

Figure 4.1 (a) and (b) show the CGI and GGI ratios, respectively, of the CIGS nanoparticle films subjected to the KCN treatments at different solution concentrations and for different durations. The CGI ratio decreases 13-16% from 0.9 in the as-coated CIGS nanoparticle film to 0.75-0.78 after the KCN treatment. Further, the amount of decrease in the Cu-ratio does not differ appreciably when higher concentrations and/or longer duration KCN etchings are used, e.g. the CGI ratio is 0.78 ± 0.01 and 0.73 ± 0.01 for the 0.25 M1/1 minute and 1.0
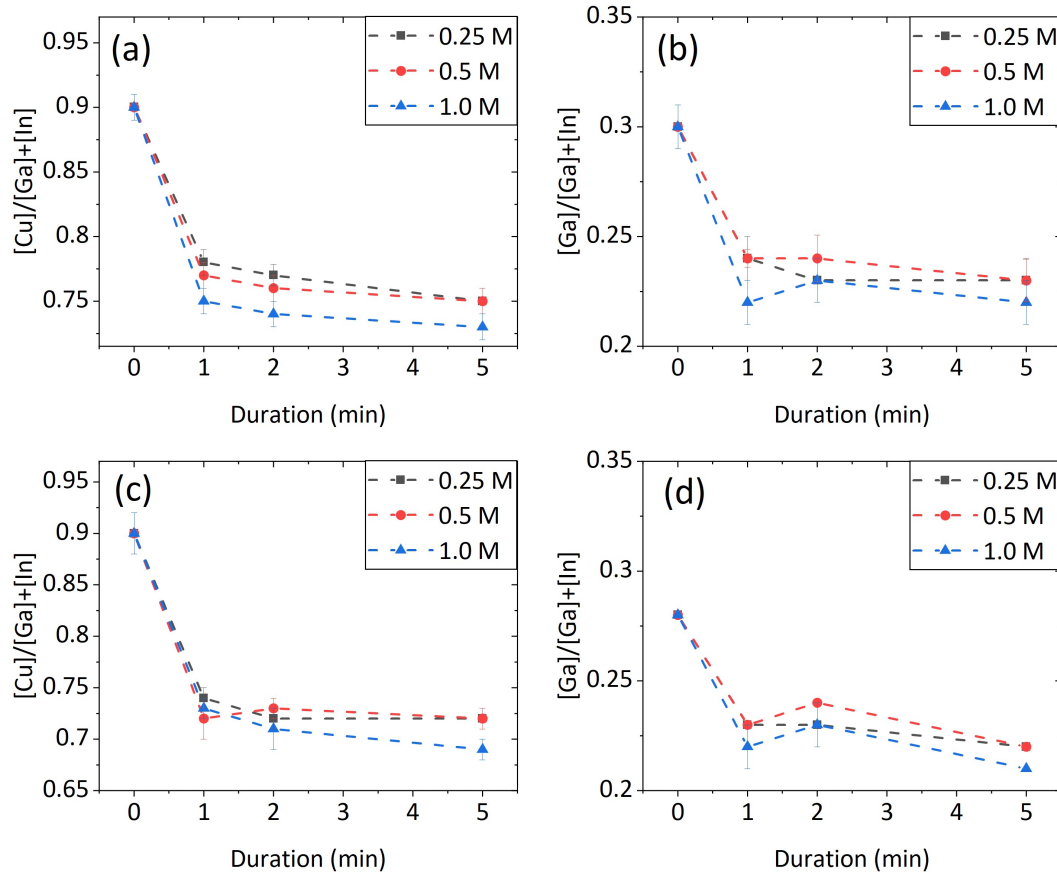
Figure 4.1. Elemental ratios of OLA-capped CIGS nanoparticle films soaked in a KCN solutions at different concentrations and for different durations, as measured by XRF. (a) [Cu]/[In]+[Ga] in CIGS nanoparticle film, (b) [Ga]/[In]+[Ga] in CIGS nanoparticle film, (c) [Cu]/[In]+[Ga] in selenized CIGSe film, and (d) [Ga]/[In]+[Ga] selenized CIGSe film.

M/5 minute conditions, respectively, whereas it the CGI ratio decreases from 0.9 ± 0.01 to 0.78 ± 0.01 for the 0.25 M/1 minute condition.. The Ga amount in the film is also affected with KCN etching, with the GGI ratio decreasing from 0.3 in the as-coated nanoparticle film to 0.22-0.24 after KCN treatments. Figure 4.1 (c) and (d) shows the CGI and GGI ratios, respectively, after the selenization of the nanoparticle film at 500 C for 20 minutes in a tubular furnace.

Figure 4.2 (a), (b), and (c) show the Raman spectra of selenized CIGSSe films (500 °C, 20 minutes) from KCN-treated nanoparticle films. All films show characteristic chalcopyrite CIGSe peaks at 176-178 cm^{-1} [66], [116]. Moreover, a prominent peak at ca. 155 cm^{-1} is
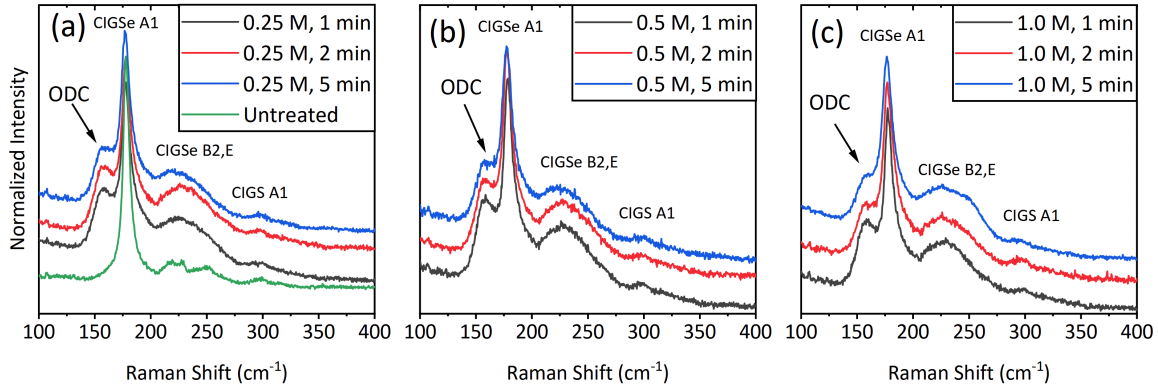
Figure 4.2. Raman spectra of CIGSSe films selenized from OLA-capped CIGS nanoparticle films (500 °C, 20 minutes) subjected to KCN solution soak prior to selenization: (a) 0.25 M KCN solution, (b) 0.5 M KCN solution, and (c) 1.0 M KCN solution. Raman spectra of an untreated CIGSSe film (selenized at the same conditions) is include in (a) for comparison.

observed for all KCN-etched samples, but not for the untreated film; this peak is attributed to the low-Cu ordered-defect-complex (ODC), which is a low Cu defect phase of the chalcopyrite lattice; this phase is observed for CIGSSe films with CGI ratios ≤ 0.80, further confirming the low CGI ratios obtained from XRF measurements (Figure 4.1) [26], [66], [74], [116]. The presence of both the CIGSe A1 (ca. 178 cm^{-1}) and the ODC (ca. 155 cm^{-1}) peak suggests that the CIGSSe film is composed of a mixture of two phases: the chalcopyrite α-Cu(In, Ga)Se$_2$ phase and the defect chalcopyrite β-Cu(In, Ga)$_3$Se$_5$ phase [116].

Figure 4.3, 4.4, and 4.5 show the SEM plan-view and cross-sectional images of the selenized CIGSSe films. All films show grain morphology composed of faceted grains, with a bi-layer grain/fine-grain cross-section. Furthermore, an apparent increase in the grain size is also observed when going from low-concentration/short-duration treatments to high concentration/long-duration treatments. The main action of KCN in nanoparticle-based CIGSSe films was attributed to the Cu-etching of the film leading to a Cu-poor stoichiometry [47], [54]. However, combined with the results from Chapter 3 on the effect of KF on CIGSSe grain growth, it is reasonable to conclude that KCN treatments also enable alkali-assisted growth via K doping.
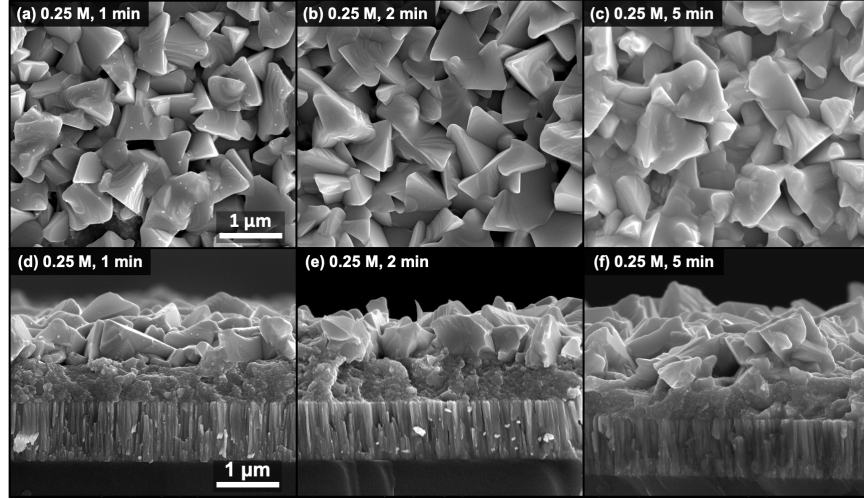
Figure 4.3. (a)-(c) Plan-view and (d)-(f) cross-sectional SEM images of CIGSSe films selenized from CIGS nanoparticle films subjected to a 0.25 M KCN treatment post-annealing for (a),(d) 1 minute; (b),(e) 2 minutes; and (c),(f) 5 minutes. Scale bar is same for all images.

4.3.1 Device Performance

CIGSSe devices were fabricated from the KCN-treated (0.5 M, 2 minutes) nanoparticle films and the results are summarized in Table 4.1 and Figure 4.6. Device parameters and illuminated J-V plots for The No Alkali baseline condition and the 10 nm KF, which was shown in Table 3.1 and Figure 3.10 (a) above, are also tabulated in Table 4.1 and plotted in Figure 4.6 for comparison; note that the data for the No Alkali and 10 nm KF case in Table 4.1 and Figure 4.6 are measured without MgF_2 anti-reflective coating. The device that was treated with KCN with no other alkali treatment shows significant performance enhancement over the untreated No Alkali baseline condition with an increase in the p.c.e. from 7.4% to 9.8% for the No Alkali and KCN-treated devices, respectively. The V_{OC}, J_{sc}, and FF all have increased markedly as a result of the KCN-treatment. Treating the KCN-treated nanoparticle film with 10 nm KF evaporated through e-beam on the as-coated film (after etching in 0.5 M KCN, 2 minutes) results in a slight increase in efficiency to 10.2%, and an increase in J_{sc} of 1.7 mA/cm^2 over the KCN-only case. The slight increase in J_{sc} over the KCN-only case is likely due enhanced grain growth during selenization caused by the
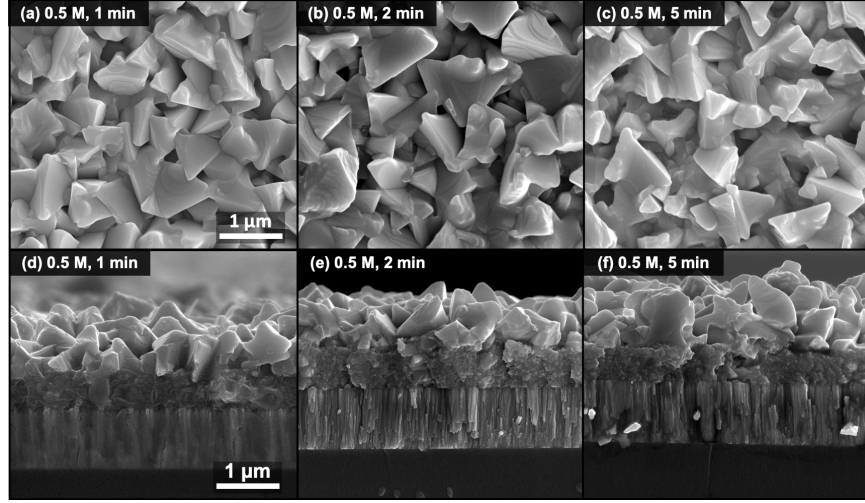
Figure 4.4. (a)-(c) Plan-view and (d)-(f) cross-sectional SEM images of CIGSSe films selenized from CIGS nanoparticle films subjected to a 0.5 M KCN treatment post-annealing for (a),(d) 1 minute; (b),(e) 2 minutes; and (c),(f) 5 minutes. Scale bar is same for all images.

additional KF. The performance enhancements realized by KCN-etching may be attributed to potassium treatment of the film.

In Table 4.2, the series and shunt resistances of the KCN-treated devices are tabulated, along with 10 nm KF and No Alkali devices (measured without MgF_2). KCN-treated devices have significantly higher shunt resistances over the non-treated devices, including the devices treated with KF only; ca. an order of magnitude increase in shunt resistance is observed for devices that had undergone KCN treatments, compared to the untreated devices, or the devices that were treated with KF only.

Table 4.1. Device Parameters of CIGSSe devices selenized from KCN-treated nanoparticle films. Also included are device parameter for the No Alkali baseline condition. All devices were measured without MgF_2 anti-reflective coating.

Condition	η (%)	V_{OC} (V)	J_{sc} (mA/cm^2)	FF (%)
No Alkali	7.4	0.55	21.5	62.3
10 nm KF	10.6	0.61	26.0	66.7
0.5 M, 2 min KCN	9.8	0.60	24.1	68.1
0.5 M, 2 min KCN + 10 nm KF	10.2	0.60	25.8	66.3
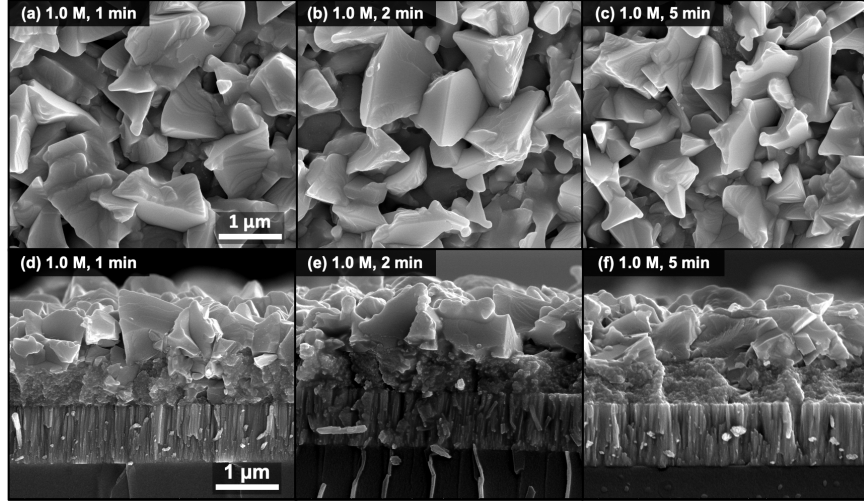
Figure 4.5. (a)-(c) Plan-view and (d)-(f) cross-sectional SEM images of CIGSSe films selenized from CIGS nanoparticle films subjected to a 1.0 M KCN treatment post-annealing for (a),(d) 1 minute; (b),(e) 2 minutes; and (c),(f) 5 minutes. Scale bar is same for all images.

Table 4.2. Calculated series resistances, shunt resistances, and reverse saturation currents for CIGSSe solar cells selenized with different alkali contents. All parameters are calculated from the dark J-V measurements and are based on total cell area.

Condition	R_{Series} ($\Omega \cdot cm^2$)	R_{Shunt} ($k\Omega \cdot cm^2$)	J_0 (mA/cm^2)
No Alkali	0.81	0.34	2.7×10^{-5}
10 nm KF	0.81	0.47	7.1×10^{-6}
0.5 M, 2 min KCN	1.20	9.04	5.3×10^{-6}
0.5 M, 2 min KCN + 10 nm KF	1.56	2.90	3.2×10^{-5}

4.4 Discussion

The aforementioned results suggest that potassium treatment alone does not explain the marked increase in shunt resistance gained by KCN, and that another mechanism may be responsible. Binary Cu_2Se_x may be the culprit for the low shunt resistances of the devices that are not treated with KCN. The presence of Cu_2Se_x will introduce shunting as it is significantly more conductive than chalcopyrite CIGSe (CIGSSe) [18]. The existence region of α-CuInSe$_2$ is relatively narrow, and obtaining a pure-phase α-CISe requires a Cu-poor film [19]. When the Cu-content is close to stoichiometry, phase segregation into α-CuInSe$_2$

83
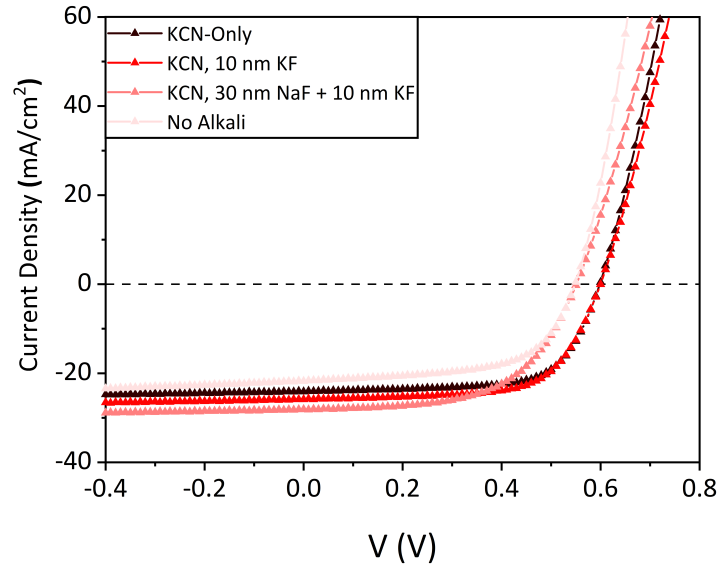
Figure 4.6. Illuminated J-V plots CIGSSe devices selenized at 500 °C for 20 minutes from KCN-treated CIGS nanoparticle films. Also included is the illuminated J-V for the No Alkali baseline condition. All J-V plots are measured without MgF_2 anti-reflective coating.

and Cu_2Se is thermodynamically favorable [19]. Even though the precursor nanoparticles were synthesized Cu-poor and the selenization is conducted on a Cu-poor nanoparticle film, some copper selenides may have formed during selenization. CIGS nanoparticle selenization and growth begins with metal diffusion from the nanoparticle film bulk to the surface, where nucleation and subsequent growth begins at the free interface [55]. Cu diffusion within the nanoparticle film is faster than both In and Ga [18], [55], thus leading to the formation of local Cu-rich regions where formation of Cu-Se binaries is favorable. In Figure 4.7, a STEM-EDS analysis of a selenized CIGSSe film from a Cu-poor OLA-capped CIGS nanoparticle film (CGI = 0.92 by XRF) shows that the carbonaceous fine grain layer contains a significant amount of Cu, along with carbon and Se, and minimal amounts of In and Ga. This suggests that during selenization, some Cu is selectively rejected to the fine grain layer, along with carbon and selenium. The rejected Cu is likely in the form of binary Cu-Se compounds [57]. Some of the originally formed Cu-Se binaries may still be present on grain boundaries, and contribute to shunting. Treating the Cu-poor CIGS nanoparticle film with KCN prior to selenization reduces the Cu content more, and shifts the selenization further away from

84

the α-CuInSe$_2$ and Cu$_2$Se two-phase region in the phase diagram [19]. The presence of Cu in the fine grain layer is known to occur for solution-processed CIGSSe fabricated from nanoparticles or molecular precursors [57], [128].

Region	Cu at%
Coarsened Layer	22.4
Fine Grain Layer	49.5
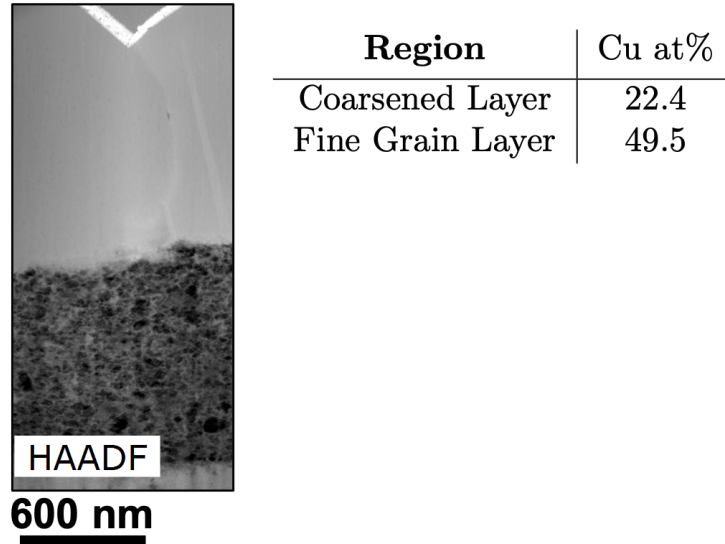
Figure 4.7. HAADF image on a FIB-obtained cross-section of a CIGSSe film selenized oleylamine-capped at 550 °C for 15 minutes, along with Cu at% obtained through STEM EDS data. FIB film ablation and STEM imaging was conducted at Brookhaven National Lab.

4.5   Conclusion

In this chapter, the effect of potassium cyanide on the morphology and device performance of CIGSSe devices fabricated from OLA-capped CIGS nanoparticles. It was found that the KCN treatments, applied on the as-coated CIGS nanoparticle films prior to selenization, induce selective Cu and Ga etching leading to a Cu and Ga poor films.

Raman spectra on the selenized films show the presence of a peak at ca. 155 cm^{-1}, which is attributed to the ODC Cu-poor phase. This suggests that the selenized CIGSSe films are composed of a mixture of two phases: chalcopyrite α-Cu(In, Ga)Se$_2$ and Cu-poor β-Cu(In, Ga)$_3$Se$_5$. The beta ODC phase formed due to the low [Cu]/[In]+[Ga] ratio of the film induced by the KCN treatments. Moreover, increases in grain size is also observed for films treated with KCN, and that the higher concentration KCN treatments results in larger grains,

suggesting that KCN-treatments contribute growth-assisted behavior of CIGSSe films, most likely by K inclusion in the film. Devices fabricated from the KCN-treated films show significant performance enhancements, compared to the untreated case, with increases in V_{oc}, J_{SC}, and *FF*.

5. INVESTIGATIONS INTO SELENIZATION AND GROWTH OF LOW-CARBON DAS-CAPPED CIGS NANOPARTICLE FILMS

5.1 Introduction

In CIGSSe processing, the selenization and grain growth step is arguably the most important step in the fabrication of CIGSSe absorbers and devices. Careful control of this process is crucial for higher quality films [22], [55].

McLeod et al. have studied the growth of CIGSSe films selenized from a oleylamine-capped sulfide CIGS nanoparticle precursor film [55]. Starting with a sulfide $Cu(In, Ga)S_2$ nanoparticle film, the selenization is a two-step process the first of which is the conversion of $Cu(In, Ga)S_2$ into $Cu(In, Ga)(S, Se)_2$, and the second is the growth of the CIGSSe film. The grain growth proceeds by the diffusion of metals towards the film surface, which can act as a free interface for nucleation, and combines with selenium forming the initial CIGSSe nuclei [55]. The grain growth proceeds towards the back of the film as a growth front consuming metals in the nanoparticle film. Moreover, McLeod et al. have found that when selenization is conducted without external alkali (Na and/or K), the grain growth will stagnate upon reaching a certain thickness, and have attributed that to carbon impurities accumulating between the nanoparticles, impeding the growth and hindering elemental diffusion [55].

As discussed in Chapter 1, selenized films of oleylamine-capped nanoparticles, both CIGSSe and CZTSSe, will result in a bi-layer morphology consisting of a coarsened top layer and 'fine grain' bottom layer that is mainly composed of carbon and selenium. The carbon originates mainly from the high-boiling oleylamine that is used during the synthesis of the nanoparticles [47], [55], [122]. Figure 5.1 shows a HAADF image along with STEM-EDS mapping of a FIB-obtained cross-section of a CIGSSe film selenized at 550 °C for 10 minutes from oleylamine-capped sulfide CIGS nanoparticles, showing the bi-layer morphology (Figure 5.1 (a)). STEM-EDS analysis of the coarsened layer shows no detectable carbon contributions, whereas the EDS analysis of the fine grain layer contains much more signifi-

cant carbon counts, along with selenium and copper; the presence of Cu in the fine grain has been seen extensively in solution-processed CIGSSe films from both the nanoparticle and the molecular precursor routes [57], [124], [128].
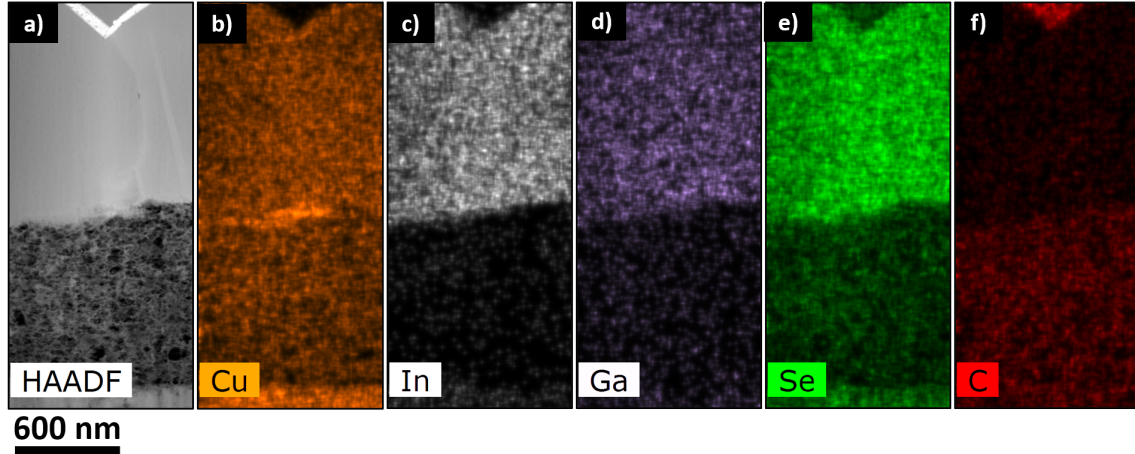
Figure 5.1. STEM-EDS on a FIB-obtained cross-section of a CIGSSe film selenized at 550 °C from OLA-capped CIGS nanoparticles. (a) HAADF Image, (b) Cu K-Series mapping on HAADF image, (c) In L-Series Mapping on HAADF image, (d) Ga K-Series mapping on HAADF image, (e) Se K-Series mapping on HAADF image, and (f) C K-Series mapping on HAADF image. Scale bar is same for all images. FIB film ablation and STEM imaging and analysis for this film was conducted at Brookhaven National Lab.

Wu et al. have studied the effect of the thickness of the fine grain layer on CZTSSe devices that were selenized from sulfide nanoparticle precursors [129]. They noted that the thickness of the this layer has no adverse impact on the performance of the device, and that the fine grain layer forms an ohmic contact with the Mo ($MoSe_2$) back contact layer. However, Wu et al. did not investigate how the presence of the fine grain layer affects the device, only that the thickness of it does not show any adverse effects [129]. That being said, the presence of fine grain adds an extra layer of impurity in the device stack, and is expected to contribute to the series resistance across the device. Williams et al. have also investigated the effect of the amount of carbon on the microstructure and growth of sulfide CZTS nanocrystals through the addition of polystyrene into their nanocrystal ink [111]. They found that the amount of carbon present in the coating affects the microstructure development, and that increasing the carbon concentration promotes abnormal grain growth

characterized by a bimodal distribution of grain sizes, particularly at the coating surface [111]. Furthermore, Rehan et al. have investigated the effects of carbon on $CuInSe_2$ films selenized from molecular precursor, and noted that the amount of carbon present in the film prior to growth significantly altered the elemental diffusion within the coarsened final film [128].

5.1.1 Scope

Multiple reports in the literature have shown that the presence and amount of carbon in the precursor film affects the microstructure development and elemental distribution during selenization and grain growth [55], [111], [128], and thus will ultimately impact the final device properties [22], [128]. In this chapter, the growth behavior of CIGSSe films selenized from almost carbon-free diammonium sulfide (DAS)-capped $Cu(In, Ga)S_2$ precursors is investigated. Different selenization conditions and growth regimes are explored to assess the microstructure development of CIGS nanoparticles containing minimal amount of carbon, into coarsened CIGSSe films. The nanoparticles are initially synthesized with oleylamine to provide size control, and then undergo a ligand exchange procedure to remove the bulky oleylamine ligand and replace it with diammonium sulfide (DAS), as outlined by Ellis et al. [57]. It is found that DAS-capped CIGS nanoparticles are very resistant to growth, compared with the conventional OLA-capped CIGS nanoparticles [55], even when grown in a liquid-assisted selenium regime, despite being almost carbon-free. Moreover, we find that the use of external Na alkali treatment can significantly enhance the growth and cause a step-change in the coarsened film thickness, and in the device performance, which differs from carbon-containing OLA-capped CIGSSe (Chapter 3) where a gradual change in the film thickness and device performance is observed with increasing alkali content [56].

5.2 Surface Capping Ligands in Nanocrystal Synthesis

The high surface-to-volume ratio exhibited by nanoparticles and nanocrystals due to their nanometer dimensions result in a high surface energy, driving the particles together into agglomeration and growing into larger clusters [61]. Also owing to their very high surface-

to-volume ratio, the surface properties of the nanoparticles and nanocrystals greatly affect their behaviors [61], [130]. To prevent aggregation and to stabilize nanoparticle suspensions, a capping ligand or a surfactant is used, which attaches to the nanoparticle surface saturating dangling bonds and providing steric hindrance shielding the particle from its environment [61]. Capping ligands are used extensively in nanocrystal syntheses as they control the nucleation and growth kinetics of the synthesis reaction [51], [54], [61]. They can also take various forms such as organic, inorganic, and polymers to name a few [61].

5.2.1 The Use of Oleylamine as a Surface Capping Ligand

Oleylamine, an organic 18-carbon primary amine, is a commonly used surfactant in nanocrystal synthesis and fabrication, and has proven to be very suitable for controlling the size and kinetics of the syntheses of various nanoparticle materials and system such as $Cu(In, Ga)S_2$ [47], [54], [55]; Cu_2ZnSnS_4 [50], [51], [131]; and Ag_2ZnSnS_2 [60]. However, because of its elevated boiling point (364 °C), oleylamine will remain attached to the nanocrystal surface, and does not leave the nanoparticle film even after annealing and selenization. Carbon from oleylamine and is left behind as a 'fine grain' layer in the final absorber film as graphitic carbon [111].

5.2.2 Ligand Exchange

The leftover carbonaceous 'fine grain' layer is mainly a consequence of the oleylamine ligand used in the nanocrystal synthesis. One way to prevent the formation of the carbonaceous fine grain layer in the coarsened film is to exchange the long chain oleylamine ligand that is attached to the nanocrystal with a shorter chain ligand that does not contain carbon, and has a relatively low boiling point; The low boiling point allows it to evaporate during the annealing (300 °C - 350 °C) and selenization ($\geq$ 450 °C) steps. One commonly used ligand to exchange oleylamine with is diammonium sulfide (DAS) (b.p. 40 °C).

As discussed in Section 5.1, McLeod et al. have investigated the selenization of CIGSSe from OLA-capped CIGS nanoparticles, and have argued that film growth will stagnate early in the growth, and have attributed that stagnation to the presence of carbon in the film

(from the oleylamine ligand) impeding the elemental transfer in the film [55]. Ellis et al. have shown that when using exchanging oleylamine with diammonium sulfide (DAS) on the CIGS nanoparticles, the majority of the carbon leaves the system, and a mostly carbon-free coarsened CIGSSe film can be obtained, when selenized at the proper conditions [57].

5.3 Experimental Section

5.3.1 Nanoparticle Synthesis and Exchange

Selenide $Cu(In, Ga)(S, Se)_2$ films and devices used in this were selenized and grown from DAS-capped sulfide $Cu(In, Ga)S_2$ nanoparticle films. Oleylamine-capped CIGS nanoparticles were first synthesized followed by a ligand exchange procedure to remove the OLA ligand and replace it with diammonium sulfide.

5.3.2 Synthesis of OLA-Capped Nanoparticles

The oleylamine-capped CIGS nanoparticles were synthesized using a heat-up synthesis with amine-thiol according to methods outlined by Deshmukh et al. [63]. Briefly, Two precursor solutions were first prepared separately in an inert environment. The first solution was prepared in a N_2-filled glovebox, and consists of Cu_2S (powder, 99.99% metals basis, Sigma-Aldrich) in a propylamine (PA)-1,2-ethanedithiol (EDT), with a concentration of 0.90 M and PA:EDT mole ratio of 2:1; the solution was left in the N_2-filled glovebox at room temperature with constant stirring until complete dissolution is achieved ($\sim$ 3 hours). The second precursor consists of In (100 mesh powder, 99.99% metals basis, Sigma Aldrich) and Ga (pellets, 99.99999% metals basis, Alfa Aesar) dissolved in PA-EDT with an overall (In + Ga) metallic concentration of 0.4 M and PA:EDT mole ratio of 2:1; The [Ga]/[Ga]+[In] ratio was 0.3. The In+Ga precursor solution was also prepared in a N_2-filled glovebox but the dissolution was conducted on a Schlenk line under Ar atmosphere at 45 °C with constant stirring and refluxing, with complete dissolution occurring within 2-3 days.

After complete dissolution is achieved in both precursor solutions, the solutions are then mixed together in a three-neck flask such that the [Cu]/[In]+[Ga] is 0.92. Oleylamine (70%, ≥98% primary amines, Sigma-Aldrich) was added to the flask with a concentration of 5.86

ml per In + Ga mmol. The three-neck flask containing the metallic solutions and OLA was prepared and sealed in a N_2 glovebox. The flask was then taken out of the glovebox and attached to a Schlenk line on which the synthesis will preformed under Ar atmosphere. The reaction solution is heated to the reaction temperature of 285 °C at which temperature the synthesis was allowed to proceed for 90 minutes. The solution was then allowed to cool naturally under inert Ar to room temperature. Following, the synthesized nanoparticles were washed in a solvent:anti-solvent mixture of hexanes and isopropyl alcohol to remove excess organics. During the washing procedure, careful care was taken to ensure that the nanoparticles are not exposed to air. The nanoparticles were then dried under Ar and stored in an inert atmosphere.

5.3.3 Ligand Exchange Procedure

Ligand exchange was conducted according to hybrid-ligand exchange methods provided by Ellis et al. in which the non-polar oleylamine ligand is exchanged with the polar diammonium sulfide [57]. 150 mg of the OLA-capped nanoparticles were dispersed in toluene and mixed with pyridine in a N_2 glovebox with a total concentration of 10 mg/ml. The mixture was then heated in a microwave reactor at 150 °C for 30 minutes with 900 rpm stirring. The resulting mixture was then centrifuged with hexanes to precipitate the nanoparticles. Following, the particles were dispersed 7.5 ml in N-methylformamide (NMF) and diammonium sulfide (DAS) (40% in H_2O, Sigma Aldrich) with a NMF:DAS ratio of 10:1 by volume, forming the polar phase; an equal amount of hexanes (non-polar phase) was also added to the solution. The solution was left stirring for 90 minutes at 900 rpm stirring, at room temperature. Following, the polar phase (NMF/DAS + particles) was extracted and added to a fresh 7.5 ml hexanes, and left stirring for 30 minutes at room temperature to further the exchange. Figure 5.2 shows an image of the solution after the exchange, showing the clear separation between the polar (NMF/DAS) and non-polar (hexanes) phases, with the particles concentrating in the polar phase. The polar phase is then extracted and washed with acetone and acetonitrile and dried under inert atmosphere. As was the case in the nanoparticle synthesis, careful care was taken to ensure that the nanoparticles are not exposed to air.
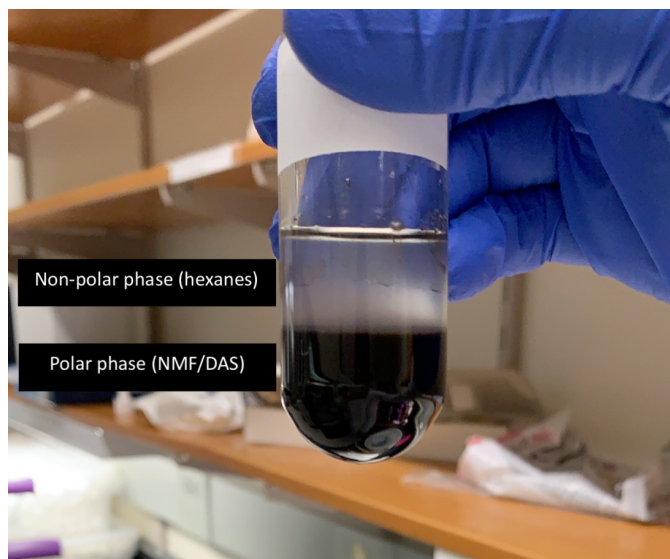
Figure 5.2. NMF/DAS (polar) and hexane (non-polar) solution, along with exchanged DAS-capped $Cu(In, Ga)S_2$ nanoparticles suspended in the polar phase.

5.3.4 DAS-Capped CIGS Nanoparticle Film Coating

Nanoparticle films are coated onto Mo-coated SLG substrates in N_2-filled glovebox using an automated blade-coating technique. The inks are formed by suspending the DAS-capped CIGS nanoparticles in dimethyl sulfoxide (DMSO) (225 mg nanoparticles per ml DMSO). On each film, 48 μl of ink is coated using four passes of 12 μl in each pass giving a final nanoparticle film thickness of 1.2-1.4 μm. For films that had external alkali treatments, alkalies were either supplied by evaporating alkali fluorides on the nanoparticle film prior to selenization (e-beam), or through soaking the nanoparticle films into a NaSCN in acetone solution.

Throughout this chapter, DAS-capped CIGS nanoparticle films refer to coated films of $Cu(In, Ga)S_2$ nanoparticles that are DAS-capped, while OLA-capped CIGS nanoparticle films refers to coated films of $Cu(In, Ga)S_2$ nanoparticles that are capped with oleylamine.

5.3.5   Selenization and Growth

In this chapter, selenization and grain growth is conducted in a tubular furnace under excess selenium atmosphere or in a three-stage rapid thermal processing furnace (RTP)

5.3.5.1   Selenization and Grain Growth in Rapid Thermal Processing Furnace

To investigate the selenization and growth of the DAS-capped nanoparticle films, a three-zone rapid thermal processing furnace is used (RTP) with argon flow serving as the carrier gas. Figure 5.3 shows a diagram of the RTP. The RTP is composed of a graphite tray on which the sample and Se are placed, and covered with graphite lids. The tray is placed inside a quartz chamber, and the heating is done through the use of banks of 500 W lamps placed on top and below the the quartz chamber.

The benefits gained from the use of the RTP is that each zone's temperature and heating/cooling rate is independently controlled via PID controllers, as is the argon (carrier gas) flow. By adjusting the temperature difference between the sample and selenium zones, selenium saturation in the vapor passing over the sample can be controlled. Moreover, adjusting the argon flow also allows us to further control selenium delivery to the sample. To ensure that the temperatures of the Se and the sample do not overlap, Se pellets are placed in a ceramic boat in Zone 3, while the sample is placed downstream in Zone 1, with Zone 2 being an intermediate zone where the temperature of the Ar stream is gradually decreased from the its setpoint in Zone 3 (Se zone) to the its setpoint in Zone 1 (sample zone). In all selenization runs, Zone 1 and Zone 2 temperatures are kept equal. A set of SLG glass shims are placed in the vicinity of the sample (same thickness as sample), with thicker shims (2x sample thickness) placed on the edges to act as a flow resistance and force the Ar stream to flow over the sample. See Appendix A for more information on the RTP furnace and representative temperature profiles.

In a typical configuration, the sample and selenium are placed in different heating zones, with selenium heated to a higher temperature than the sample, e.g. difference between T_{Se} and T_{sample} is 25 - 50 °C. T_{Se} and T_{sample} denote the selenium (Zone 3) and sample temperatures (Zone 1), respectively. Argon flows over the selenium vapor in Zone 3, at vapor

pressure of $P_{Se}(\text{T}_{\text{Se}})$, and carries over to the sample in Zone 1, where the lower temperature will cause the Se to condense on the sample due to the lower temperature and selenium vapor pressure $(P_{Se}(\text{T}_{\text{sample}}) < P_{Se}(\text{T}_{\text{Se}}))$.
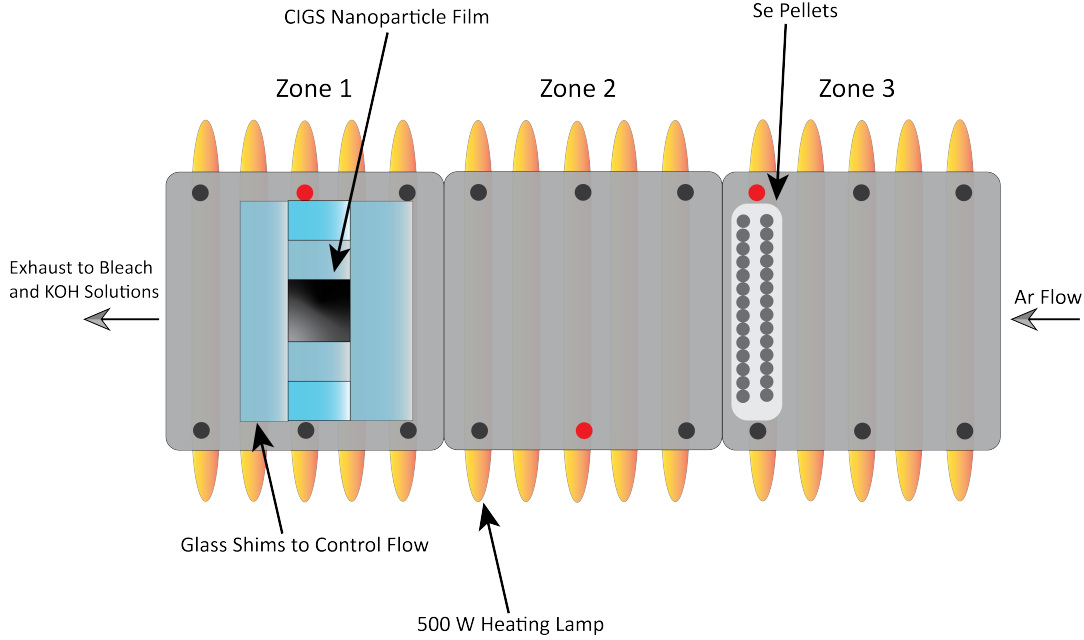
Figure 5.3. Top-down diagram of three-zone rapid thermal processing furnace (RTP). Banks of 500 W heating lamps are placed above and below Red circles denote thermocouple positions.

5.3.6 Device Fabrication and Characterization

Devices were fabricated in a similar manner to what is done in Chapter 3 using the conventional SLG/Mo(800 nm)/CIGSSe(1.2-1.4 μm)/CdS(50 nm)/i-Zno(80 nm)/ITO(220 nm)/Ni-Al stack. Devices are fabricated and measured without the use of MgF_2 anti reflective coating.

Plan-view and cross-sectional scanning electron microscopy images were obtained using a FEI Quanta electron microscope (10 keV accelerating voltage). Overall Elemental analysis was conducted via X-ray fluorescence using a Fisherscope XAN 250 X-ray Fluorescence instrument. EDS elemental analysis was also conducted on some films using an Oxford INCA X-stream 2 silicon drift detector attached to the SEM instrument, with an accelerating

voltage of 20 keV. Raman Spectroscopy measurements were performed using a Horiba/Jobin Yvon HR800 confocal microscope (50x) with a 633 nm He:Ne laser for excitation. X-ray diffraction scans were conducted in Bragg-Brentano mode using Cu K_α radiation using a Rigaku Smart-Lab diffractometer.

J-V measurement on completed devices was conducted using an Oriel SOL3A solar simulator under AM1.5 conditions. J-V data was analyzed using the model by Hegedus et al. [7].

5.4 Results

Figure 5.4 shows a plan-view and a cross-sectional image of a representative image of a DAS-capped $Cu(In, Ga)S_2$ nanoparticle film on a Mo-coated SLG substrate. The nanoparticle films exhibit no cracks in the film, and a relatively flat morphology, with a thickness of ~ 1.3 μm.
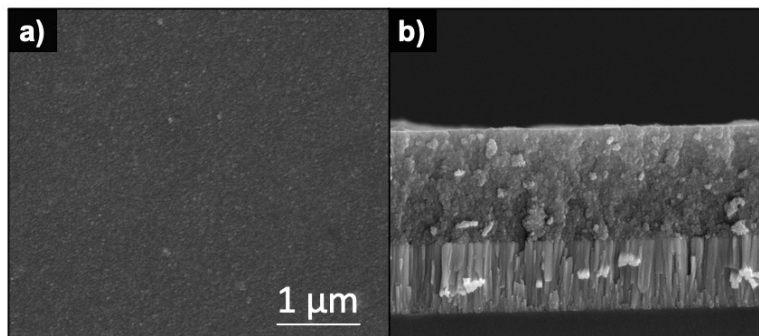
Figure 5.4. (a) Plan-view and (b) cross-sectional images of a CIGS nanoparticle film coated with DAS-capped CIGS nanoparticles suspended in DMSO. Scale bar is same for both images.

As a starting point to investigate the growth of DAS-capped CIGS nanoparticle, the films were selenized using a conventional tubular furnace at 500 °C, similar to what is done for the selenization of OLA-capped CIGS (see Chapter 3). Initially, the films were selenized without the addition of external alkali.[1] Films were selenized in a tubular furnace under a Se atmosphere at 500 °C for 20, 30, and 40 minutes. Figure 5.5 shows SEM plan view

---

[1]Some Na does diffuse from the soda-lime glass substrate into the film during the 500 °C selenization. See Figure 3.8 in Chapter 3 and refs. [18], [71]

and cross-sectional images of those films. In Figure 5.5 (a)-(c), the plan view images show that all films are characterized by a dense morphology of coarsened grains. Moreover, going from 20 to 40 minute selenization, minimal changes are observed in the grain morphology, even when doubling the selenization duration. The cross-sectional images of the same films, shown in Figure 5.5 (d)-(f), show that almost the entire thickness of the film (~ 900 nm) consists of an uncoarsened fine grain layer, with a thin coarsened layer (~ 350 nm) at the top. Figure 5.6 shows EDS mapping on the CIGSSe film that was selenized for 20 minutes at 500 °C (Figure 5.5 (a), (d)). EDS mapping shows that this fine grain layer is composed of unsintered metal, i.e. Cu, In, Ga, and Se that did not incorporate into the coarsened layer at the top.
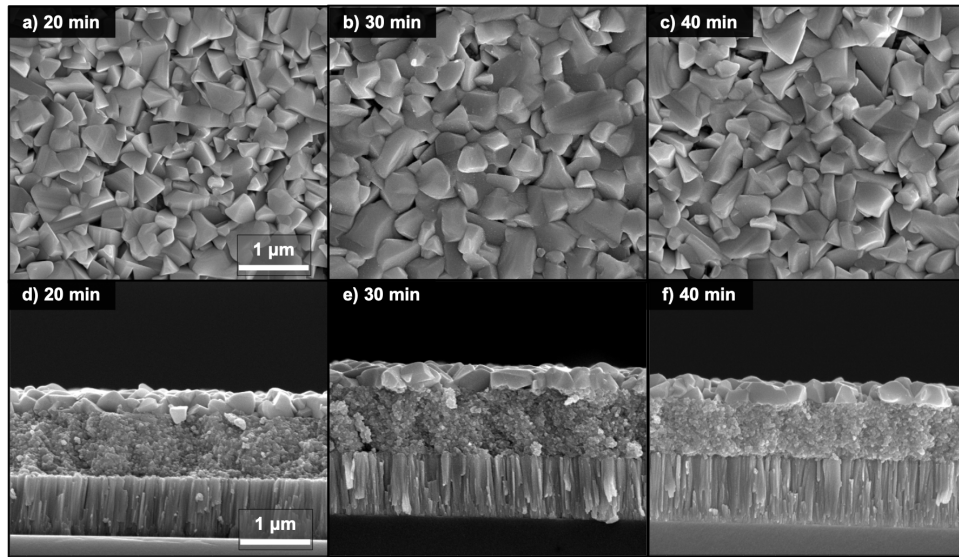
Figure 5.5. (a)-(c) Plan-view and (d)-(f) cross-sectional images of CIGSSe films selenized in a tubular furnace with excess Se from a DAS-capped CIGS nanoparticle film. Films were selenized at 500 °C for (a),(d) 20 minutes; (b),(e) 30 minutes; (c),(f) for 40 minutes. Scale bar is same for all images.

The films shown in Figure 5.5 indicate that the duration of selenization at 500 °C has little effect on the selenized film size and coarsened thickness, suggesting that the films have reached a thermodynamic limit (at 500 °C) preventing them from growing further, and resulting in a bi-layer morphology unsintered fine grain layer consisting mainly of unreacted metals. The DAS-capped CIGS nanoparticle films in Figures 5.5 also show similarity to the selenization of high carbon OLA-capped $Cu(In, Ga)S_2$ nanoparticles in that the films
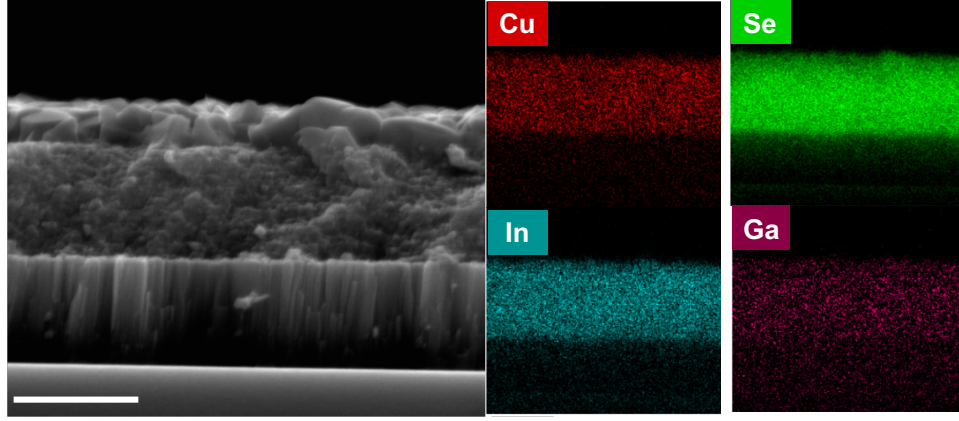
Figure 5.6. EDS mapping on CIGSSe film selenized from DAS-capped CIGS nanoparticles at 500 °C for 20 minutes in a tubular furnace. EDS data was collected under an accelerating voltage of 20 keV. Scale bar denotes 1 μm.

will stagnate upon reaching a certain thickness provided that there is no external alkali supply.[55].

Figure 5.7 shows illuminated J-V curves for CIGSSe devices fabricated from the films shown in Figure 5.5; performance parameter are summarized in Table 5.1. The device parameters of CIGSSe devices fabricated from DAS-capped films, without any alkali addition, shows very poor performance, with a markedly low V_{oc} and J_{sc}. This is in contrast to OLA-capped films where films selenized without external alkali at the same conditions (20 minutes, 500 °C, See Table 3.1 in Chapter 3) show significantly better performance (3.4% vs. 8.8% (with MgF$_2$) for the DAS-capped and OLA-capped films, respectively.

Table 5.1. Performance parameters for CIGSSe devices selenized from DAS-capped CIGS nanoparticles at 500 °C (SEM plan-view and cross-sections shown in Figure 5.5). All efficiencies are based on total cell area, and are measured without MgF$_2$ anti-reflective coating.

Condition	η (%)	V_{OC} (V)	J_{sc} (mA/cm^2)	FF (%)
20 min	3.4	0.38	17.1	53.1
30 min	3.9	0.46	15.9	53.1
40 min	4.9	0.43	22.3	50.7
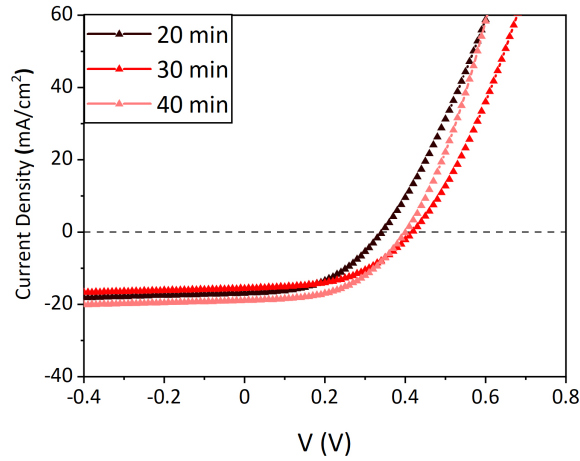
Figure 5.7. Illuminated J-V curves for CIGSSe devices selenized from DAS-capped nanoparticle films at 500°C for 20, 30, and 40 minutes without external alkali addition.

As described in the introduction of this chapter, McLeod and co-workers have suggested that OLA-capped CIGS nanoparticles' growth stagnation is due to the carbon accumulation in the film [55]. In their OLA-capped CIGS nanoparticle selenization and growth model, Cu, In, and Ga diffuse towards the surface, which serves as a free interface for nucleation, and combine with the growing front [55]. As the growth proceeds, more and more metals diffuse to the surface leaving behind carbon from the OLA ligand [55]. They suggest that the accumulation of carbon will impede the growth causing it to eventually stagnate. However, CIGS nanoparticle films from DAS-capped nanoparticles do stagnate despite that the nanoparticles and the nanoparticle films have minimal amount carbon. This suggests that another mechanism may be at play preventing the DAS-capped nanoparticle films from growing further.

To investigate the growth behavior of DAS-capped nanoparticles, the rapid-thermal processing furnace is utilized, which allows significantly more control of the selenization process.

5.5 Grain Growth and Selenization using Rapid Thermal Processing Furnace

In the previous section, the selenization and growth behavior of DAS-capped $Cu(In, Ga)S_2$ nanoparticles was investigated using a tubular furnace, where only the selenization duration was varied. it was found that under selenization conditions of 500 °C, DAS-capped CIGS

nanoparticles showed minimal growth into CIGSSe films, with corresponding devices performing poorly. To gain more insight into the growth behavior, a three-zone rapid thermal processing furnace was used. As described in Section 5.3, the use of the RTP allows more control over the selenization process as the Se vapor pressure, Se delivery, sample temperature, and Se temperature can be varied.

In this section, different selenization and growth conditions are explored in order to deduce under which conditions can the DAS-capped CIGS films be sintered and grown into fully coarsened CIGSSe grains. Process growth variable explored in this chapter are the sample temperature, Se temperature, and argon flowrate. In all conditions, the samples and Se were heated rapidly to their respective setpoints (~ 10 °C/s). When cooling, a controlled profile was used that ensures that Se temperature is always higher than the sample's, until 300 °C. This is to prevent selenium loss from the CIGSSe film [41]. Table 5.2 below lists the parameters that are varied and their corresponding effects on the selenization process.

Table 5.2. Controllable furnace parameters in the RTP furnace, and their corresponding effects on the selenization process

Parameter	Controlled process variable
Sample temperature	Selenization and growth temperature
Se temperature	Se vapor pressure and saturation over the sample
Argon flowrate	Selenium delivery to sample

Figure 5.8 shows the SEM plan view and cross-sectional images of CIGSSe films selenized in the RTP from DAS-capped CIGS nanoparticles at $T_{sample} = 500$ °C, and $T_{Se} = 525$ °C. In both 0.1 l/min and 0.6 l/min flowrates, very low nucleation and growth is observed.

In Figure 5.8, a decrease in the grain size and nucleation is observed when going from 0.1 l/min to 0.6 l/min flowrate. This behavior is attributed due to the differences in Se saturation between the two conditions. In an ideal case, the Se is heated to a higher temperature than the sample to ensure a Se oversaturation over the sample, i.e. the Se vapor pressure around the selenium pellets in Zone 3 is higher than the Se vapor pressure around the sample, thus forcing condensation of liquid Se on the sample surface. In a typical run, the temperature of Zone 1 and Zone 2 are kept the same, with Zone 3 usually at a higher temperature. As the

Ar stream is heated to T_{Se} when it enters the furnace quartz chamber, it will need a finite amount of time to reach T_{Se}. Since higher flowrates will have shorter residence times in each zone, the 0.6 l/min stream temperature will not be reach T_{Se} when the Ar flows over the Se pellets, and as such will not be saturated with Se. See Appendix A for more information.
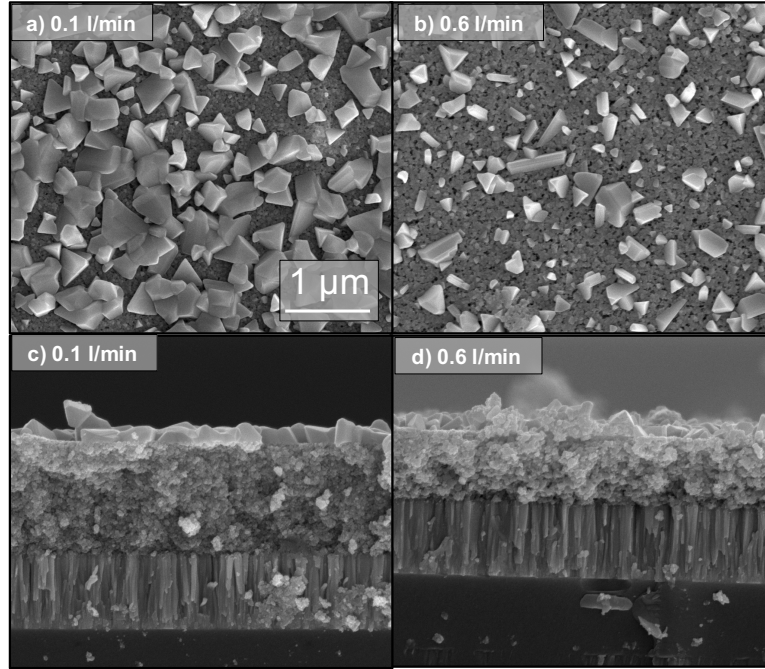
Figure 5.8. Plan-view (a),(b) and cross-sectional (c),(d) SEM images of CIGSSe films selenized from DAS-capped CIGS nanoparticles in the RTP for 15 minutes at 500 °C, with Se at 525 °C, with different Ar flowrates: (a),(c) 0.1 l/min; (b),(d) 0.6 l/min. Scale bar is same for all images.

Figure 5.9 shows the SEM plan-view and cross-sectional images of CIGSSe films selenized at 550 °C (Se at 575 °C) for 10 minutes. Increased nucleation and grain sizes are observed for these films, over the films that were selenized at 500 °C (Figure 5.8). This consistent of increasing growth rate with temperature and Se partial pressure over the film. Varying the Se partial pressure over the sample also has little effect on the resulting film morphology. Figure 5.10 shows CIGSSe films selenized at different Se temperatures (partial pressures). The same sparse grain morphology on the surface, combined with a significantly large un-sintered fine grain layer.

Figure 5.11 shows the effect of selenization duration on the film morphology (T_{sample} = 550 °C, T_{Se} = 575 °C, 0.1 l/min Ar flow). Varying the selenization duration has some effect

on the surface morphology of the film in that a step increase in the grain coverage area is observed as the duration is increased from 5 minutes to 10 (Figure 5.9 (a), (c)) to 15 minutes. That being said, the same bi-layer morphology remains. Moreover, in the 5 min, 550 °C film (Figure 5.11 (a)), very few nuclei are observed on the surface of the film despite the film being at 550 °C, and exposed to a Se oversaturation. McLeod and co-workers have shown that in the selenization of OLA-capped nanoparticles, nucleation is very rapid when selenized in Se overaturation, with the surface of the film being completely covered with CIGSe nuclei within the first 20 seconds of selenization [55]. Figure 5.11 (e) shows the Raman spectra of the films shown in Figure 5.11, which indicates that both films are completely selenide $Cu(In, Ga)Se_2$, with no detectable sulfide $Cu(In, Ga)S_2$ present in the film.
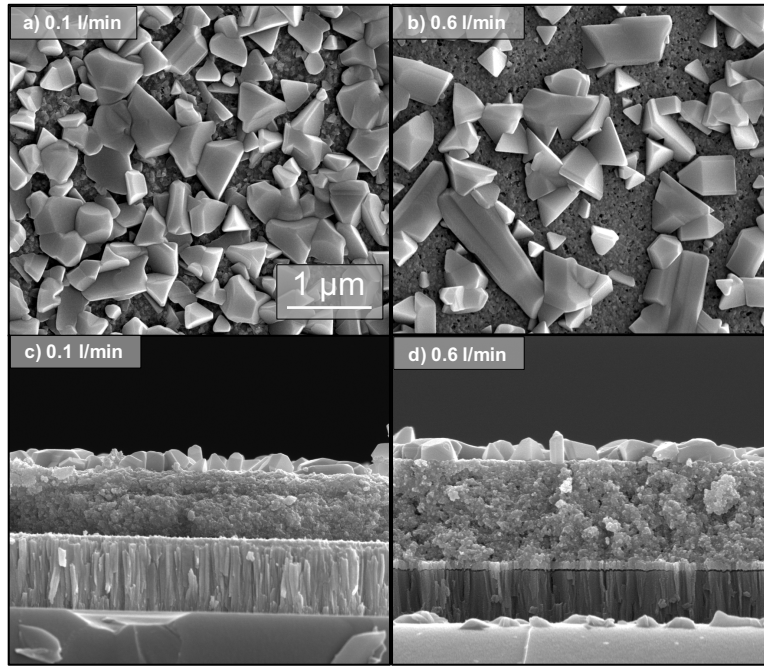
Figure 5.9. Plan-view (a),(b) and cross-sectional (c),(d) SEM images of CIGSSe films selenized from DAS-capped CIGS nanoparticles in the RTP for 10 minutes at 550 °C, with Se at 575 °C, with different Ar flowrates: (a),(c) 0.1 l/min; (b),(d) 0.6 l/min. Scale bar is same for all images.

It is apparent from the observations above that DAS-capped $Cu(In, Ga)S_2$ nanoparticles are resistant to growth. The growth of these nanoparticle films is limited, even at elevated selenization temperatures, e.g. 550 °C. Moreover, the bi-layer morphology is retained with variation of the Se vapor pressure over the sample. The films shown above are selenized
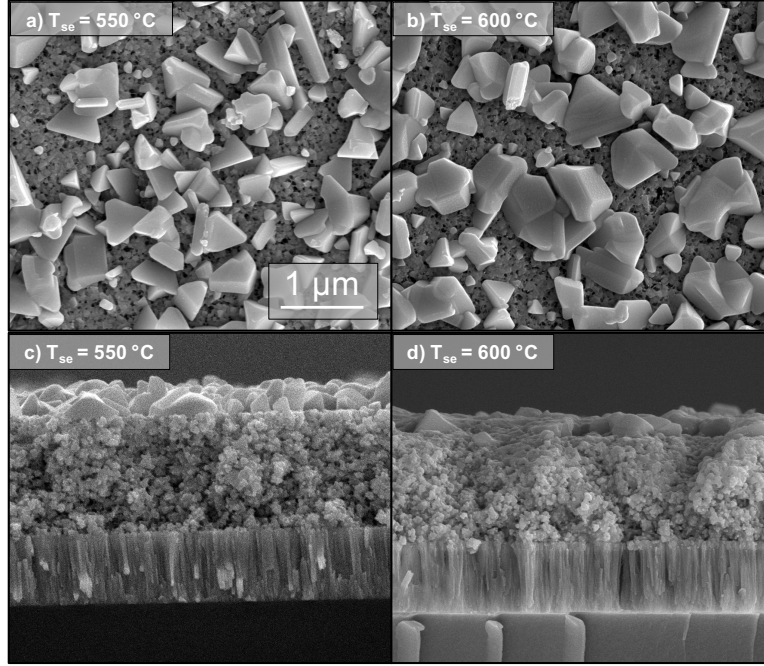
Figure 5.10. Plan-view (a),(b) and cross-sectional (c),(d) SEM images of CIGSSe films selenized from DAS-capped CIGS nanoparticles in the RTP for 10 minutes with 0.1 l/min Ar flow, at T_{sample} = 550 °C, and T_{Se}: (a),(c) 550 °C; (b),(d) 600 °C. Scale bar is same for all images.

without the use of any external alkali treatments. Introducing Na into the system may provide a liquid-flux that may lead to further coarsening of the film.

Figure 5.12 shows the SEM plan-view and cross-sectional images of CIGSSe films selenized from DAS-capped CIGS nanoparticles, with 15 nm NaF evaporated onto the nanoparticle film prior to selenization. A step-change in the grain size and coarsened film thickness is observed with the addition of 15 nm NaF, compared with films selenized at the same conditions without external Na addition (Figure 5.9). The 0.1 l/min film (Figure 5.12 (a),(c)), that was selenized at 550 °C (Se at 575 °C) with the Na addition shows very dense morphology with $\sim 2\mu$m-wide grains, and a cross-section that is characterized by single grains that span the entire film thickness. Minimal fine grain layer thickness is observed in the films shown in Figure 5.12 due to the precursor nanoparticle film being composed of low-carbon DAS-capped $Cu(In, Ga)S_2$ nanoparticles. Similar grain morphology is also observed for CIGSSe films selenized in the tubular furnace at 500 °C for 20 minutes, with 15 nm NaF treatments (Figure 5.12 (e),(f)).

103
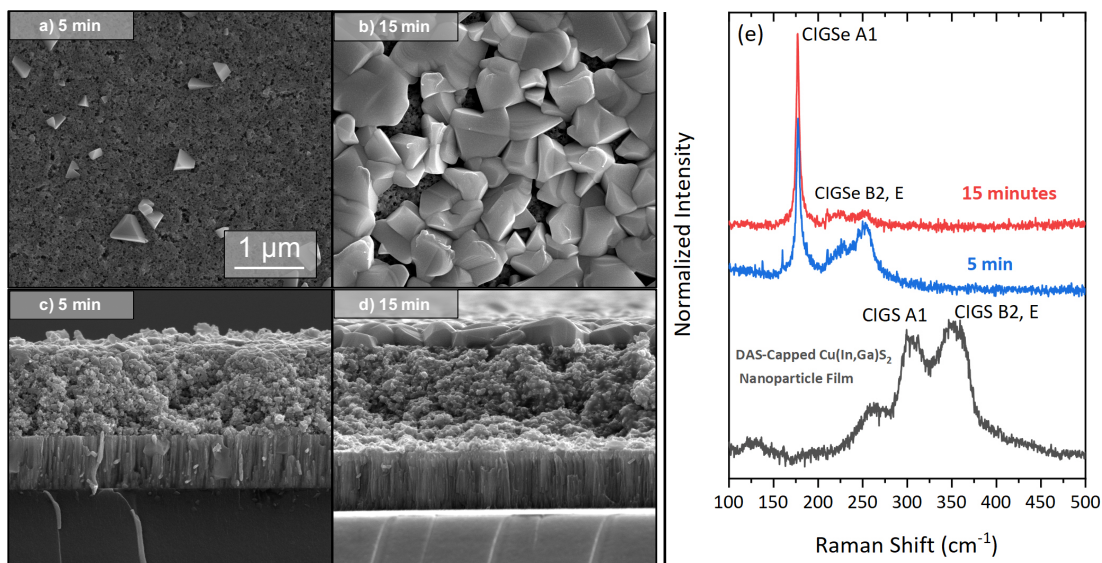
Figure 5.11. Plan-view (a),(b) and cross-sectional (c),(d) SEM images of CIGSSe films selenized from DAS-capped CIGS nanoparticles in the RTP 0.1 l/min Ar flow, at T_{sample} = 550 °, and T_{Se} = 575 °C for (a),(c) 5 minutes, (b),(d) 15 minutes. (e) Raman spectra of films shown in (a)-(d), along with the spectrum of DAS-capped $Cu(In, Ga)S_2$ film. Scale bar is same for all SEM images.

5.6   Discussion

From the aforementioned observations, it is apparent that selenization and grain growth, at 500 °C and 550 °C, of DAS-capped $Cu(In, Ga)S_2$ nanoparticle films into a coarsened $Cu(In, Ga)(S, Se)_2$ film is poor without the use of external alkali, resulting in films characterized by a very thin coarsened layer at the top and significantly larger fine-grain layer at the bottom. The fine grain layer is composed of metals that were not incorporated into the growing grains, and Se. External Na alkali treatments to the film prior to selenization results in a step increase in the coarsened layer thickness, and results in a dense film morphology, with single grains spanning the thickness of the films and minimal fine grain layer. This is not the case with OLA-capped films (Chapter 3 and ref. [55]) where a gradual increase in grain size and in coarsened layer thickness is observed [55]. Furthermore, CIGSSe solar cell devices selenized from DAS-capped CIGS nanoparticles show poor performance, this is also differs from OLA-capped nanoparticles in that CIGSSe devices fabricated using the same
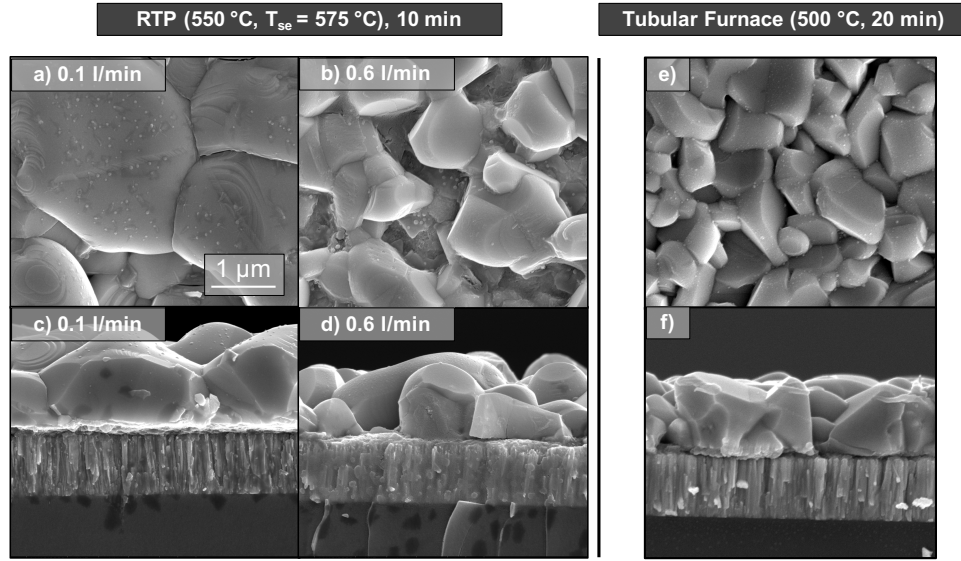
Figure 5.12. Plan-view (a),(b) and cross-sectional (c),(d) SEM images of CIGSSe films selenized from DAS-capped CIGS nanoparticle films in the RTP for 10 minutes at 550 °C, with Se at 575 °C, with different Ar flowrates: (a),(c) 0.1 l/min; (b),(d) 0.6 l/min. (e),(f) CIGSSe film selenized in tubular furnace at 500 °C for 20 minutes. Prior to selenization, nanoparticle films had 15 nm NaF evaporated onto their surface via e-beam evaporation. Scale bar is same for all images.

conditions show considerably better performance (Chapter 3 and ref. [56]), despite having carbon present in the film.

From the observations in the films that were selenized without alkali (Figures 5.8 - 5.11), the hypothesis is that the grain growth of DAS-capped CIGS nanoparticles follows a top-down growth model, similar to the model proposed by McLeod et al. for OLA-capped CIGS nanoparticles [55]; their growth model was extended from an earlier CZTS nanoparticle growth model proposed by Carter et al. and Hages et al. using EDXRD measurements [115], [132]. In the model proposed by McLeod et al., the selenization of $Cu(In, Ga)S_2$ nanoparticles proceeds with surface nucleation of $Cu(In, Ga)Se_2$ grains forming a coarsened growth front [55]. Metals (Cu, In, Ga) diffuse from the nanoparticle film bulk and incorporate into the growing front leading to further coarsening of the film (See Figure 5.13 below) [55].

Hages et al. reported similar observations regarding the growth of DAS-capped CZTS nanoparticle films, obtained through a ligand exchange process from OLA-capped CZTS nanoparticles [115]. They reported film resistance to selenization and growth, and attributed
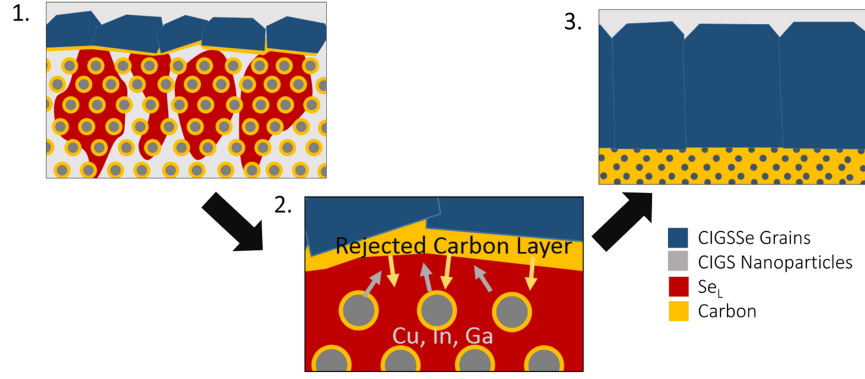
Figure 5.13. Diagram illustrating liquid-assisted growth model for the selenization and growth of OLA-capped $Cu(In,Ga)S_2$ nanoparticle films [55]. Reprinted with permission from McLeod, S.; Alruqobah, E.; Agrawal, R. Liquid Assisted Grain Growth in Solution Processed $Cu(In,Ga)(S,Se)_2$. Sol. Energy Mater. Sol. Cells 2019, 195 (February), 12–23. [55].

that to the inability of liquid selenium to diffuse into the film through capillary action, due of the smaller inter-particle distance of the DAS-capped nanoparticles compared to the OLA-capped nanoparticles [115]. While the inter-particle distance between DAS-capped nanoparticles is indeed smaller than that of OLA-capped nanoparticles (due to the smaller DAS ligand compared with the bulky oleylamine ligand), it does not explain the fact that the growth resistance can be overcome with the addition of alkali. One of the actions of Na is that it provides a liquid flux, in the form of Na_2Se_x, in the film that accelerates diffusion and growth. If the smaller inter-particle distance of DAS-capped nanoparticles is the culprit of the reduced growth resistance, than adding a liquid flux agent, i.e. Na_2Se_x, should not affect the growth appreciably. Moreover, CIGSSe films selenized from sulfide CIGS molecular precursor films (Figure 5.14), where the film porosity and inter-particle spacing in the film is smaller than in a DAS-capped nanoparticle films, do not exhibit growth the resistance observed herein. Note that the tri-layer morphology observed in Figure 5.14 (b) is typically observed in selenized films from amine-thiol-based sulfide molecular precursor films. McLeod and co-workers have shown that during the selenization of oleylamine-capped $Cu(In,Ga)S_2$, rapid nucleation occurs (within the first ~ 20 seconds when selenized at 500 °C) [55]. They also observed growth stagnation in OLA-capped nanoparticles, and attributed that to carbon (from oleylamine) accumulation between the particles. However, in the present case, despite

106
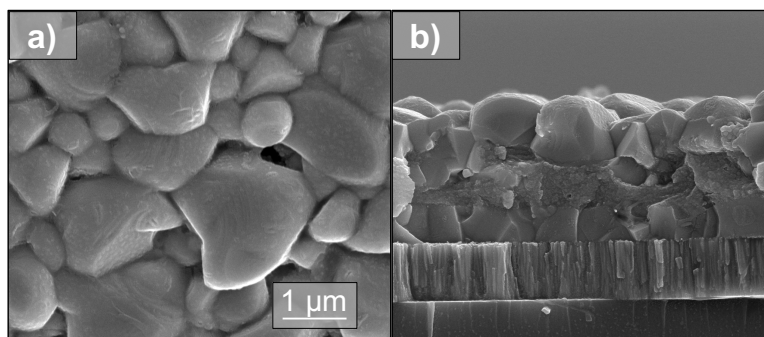
Figure 5.14. (a) SEM plan-view and (b) cross-sectional image of a CISSe film selenized from amine-thiol-based CuInS$_2$ molecular precursor film at 560 °C in a tubular furnace for 6 minutes. Scale bar is same for both images. Figure courtesy of Swapnil D. Deshmukh.

that there is minimal amount of carbon present in the film [57], the growth is severely hindered. Moreover, surface nucleation is also limited in that complete film coverage with coarsened grains is difficult to achieve (without the use of Na), even with Se oversaturation.

The hypothesis is that the growth resistance is due to the nanoparticle surface. Going from Oleylamine-capped CIGS nanoparticles to sulfide-capped CIGS, the surface environment around the nanoparticles is changed (Figure 5.15). This in turn will affect how the film interacts with selenium; sufficient amounts of selenium are needed for growth [55]. To test this hypothesis, a DAS-capped CIGS nanoparticle film is coated with a thin layer of oleylamine-capped CIGS nanoparticles, and selenized in the RTP for 15 minutes at 500 °C, with Se oversaturation (Similar to the selenization conditions of the films shown in Figure 5.8); Figure 5.16 shows the SEM images of this film. Although the film top-down morphology still shows sparse grains, the grain sizes are notably larger than in the films selenized with DAS-capped nanoparticle only, further suggesting that the growth issue is due to different nanoparticles.

Introducing Na externally into the film leads to significant changes in the extent of growth. Sodium is known to have a high affinity to selenium, and has been shown to improve the Se sticking coefficient onto the CISe surface [113]. The fact that surface nucleation with DAS-capped CIGS nanoparticles is limited, and adding sodium in the film leads to a step change in both the film coverage and coarsened film thickness suggest that the issue with
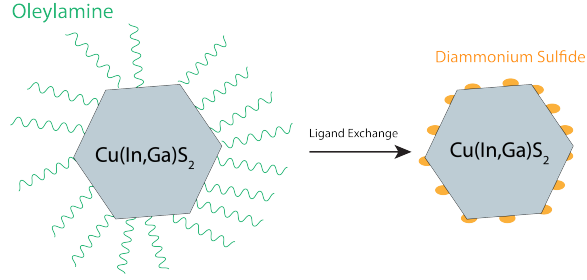
Figure 5.15. Simple diagram of oleylamine-capped (left) and sulfide-capped (right) $Cu(In, Ga)S_2$ nanoparticles.
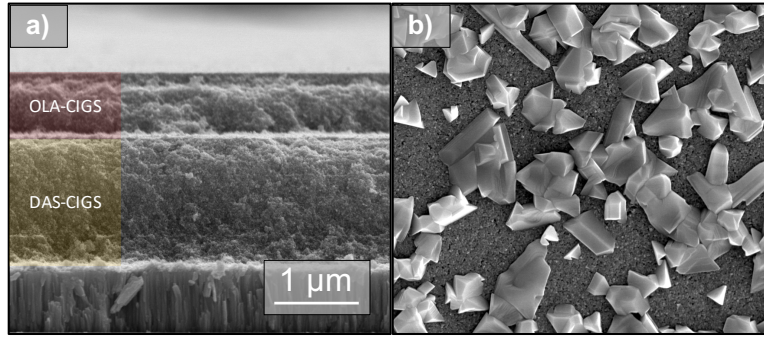
Figure 5.16. (a) Cross-sectional SEM image of a bi-layer nanoparticle film composed of diammonium sulfide-capped $Cu(In, Ga)S_2$ nanoparticle film (bottom) and oleylamine-capped $Cu(In, Ga)S_2$ nanoparticle film. (b) SEM plan-view image of CIGSSe film selenized in the RTP from the film shown in (a), at 500 °C (T_{Se} = 525 °C) for 15 minutes. Scale bar is same for both images.

DAS-nanoparticles are related to Se incorporation into the film. Moreover, the results above suggest that post-deposition (selenization) treatments of Na, or other alkali, as is done in vacuum-based CIGSe and CIGSSe processing is not adequate for the selenization of low-carbon DAS-capped nanoparticle films, and external alkali treatments, *prior to selenization*, are a requirement for high-quality absorber films.

5.7 Conclusion

In this chapter, the growth and selenization behavior of low-carbon diammonium sulfide-capped $Cu(In, Ga)S_2$ nanoparticle films is investigated. It was found that these particles are resistant to growth, and that films grown under various selenization and annealing conditions are characterized by a bi-layer morphology that is composed of a coarsened thin layer at the top of the film, with a much larger 'fine grain' layer that is composed of unincorporated metals (Cu,In,Ga), and Se. Moreover, surface nucleation is also limited, compared to conventional oleylamine-capped $Cu(In, Ga)S_2$.

The growth resistance and limited surface nucleation was attributed to the difficulty of adequate amounts of Se, a requirement for appreciable growth, to be incorporated into the DAS-capped CIGS nanoparticle films. Introducing external sodium treatment, in the form of 15 nm evaporated NaF onto the nanoparticle film, has significantly enhanced the growth, with resulting films having a dense top-down morphology, and cross-section morphologies that are characterized by single grains spanning the thickness of the film. These results demonstrate that for appreciable growth of low-carbon DAS-capped $Cu(In, Ga)S_2$ nanoparticle films, alkali treatments introduced prior to selenization are a requirement.

6. RUBIDIUM FLUORIDE TREATMENTS FOR DAS-CAPPED NANOPARTICLE-BASED CIGSSE SOLAR CELLS

6.1 Introduction

As mentioned in Chapter 2, one of the most significant developments in $Cu(In, Ga)Se_2$ and $Cu(In, Ga)(S, Se)_2$ solar cell fabrication is the inclusion of heavy alkali treatments (K, Rb, Cs) [11]. Chirilă and co-workers have demonstrated enhanced performance of CIGSe solar cell devices when subjected to a KF-PDT, significantly surpassing CIGSe devices treated with Na only [12]. However, Jackson et al. demonstrated significant performance enhancements with CIGSe films treated with a RbF post-deposition treatments, with a gain in the p.c.e. from 20.3% (Na only, diffused from SLG substrate) and 20.8% (KF-PDT) to 22.6% using RbF-PDT [133], [134]. The benefits of Rb have also been applied to low bandgap near-stoichiometric $CuInSe_2$ solar cells [135]. Feurer et al. reported significant device performance enhancment of high Cu $CuInSe_2$ as a result of Rb treatments, where the device efficiency increased from 14.3% to 19.2% as a result of RbF-PDT [135].

Enhanced absorber quality and CIGSe/CdS interface is also reported with Rb-treated CIGSe films [97], [136]. Using calibrated photoluminescence measurements, Wolter et al. reported increased quasi-Fermi level splitting and reduced non-radiative recombination for CIGSe films treated with Rb [97]. Furthermore, Rb treatments have been reported to induce modifications of the CIGSe grain boundaries, and on the CIGSe/CdS interfaces [136]. Cu-depletion of the grain boundaries as a result of RbF treatments was demonstrated by Raghuwanshi and co-workers; this is believed to be beneficial to the CIGSe device performance as Cu-depleted grain boundaries act as a hole barrier [136].

Rubidium treatments and effects on CIGSe and CIGSSe films and devices have only been reported on vacuum-based devices grown via co-evaporation [75], [100], [134] and two-step [42] routes. No reports on Rb treatments on solution-processed CIGSe (CIGSSe) are published. In this chapter, preliminary results on the effects of Rb treatments on solution-processed CIGSSe films, fabricated from DAS-capped $Cu(In, Ga)S_2$ nanoparticles is presented. It was found that Rb treatments, when applied on the as-coated films prior to

selenization and grain growth, show growth-assisting behavior, similar to Na and K, an observation which is not reported in the literature. Moreover, reduced non-radiative recombination is also reported for films treated with RbF in the form of enhanced PL response.

6.2   Experimental

$Cu(In, Ga)(S, Se)_2$ films used in this chapter are grown from a 1.2 μm DAS-capped $Cu(In, Ga)S_2$ nanoparticle films. Details on the synthesis, ligand exchange, and coating of the DAS-capped CIGS nanoparticle ink are given in Chapter 5. Rb treatments were delivered to the as-coated film, prior to selenization, through the thermal evaporation of RbF powder (Alfa-Aesar, 99.975% metals basis). Selenization and grain growth was conducted in a tubular furnace under an inert atmosphere, with the sample placed in a rectangular graphite box with Se pellets (~ 300 mg). The selenized films had a CGI ratio of 0.93 ± 0.01, and a GGI ratio of 0.29 ± 0.005.

Scanning electron microscope plan-view and cross-sectional images were obtained using a FEI Quanta electron microscope. Elemental analysis on the overall film were obtained using a Fischerscope XAN 250 X-ray fluorescence instrument. Raman Spectroscopy and photoluminescence (PL) measurements were performed at room temperature via a Horiba/Jobin Yvon HR800 confocal microscope with a 50x objective lens. A 633 nm He:Ne laser was used for excitation. PL spectra of all films were collected at the same conditions.

6.3   Results

Figure 6.1 shows the SEM plan-view and cross-section of CIGSSe films selenized at 500 °C for 20 minutes, with different evaporated RbF thicknesses; note that 'No RbF' film is the same film that was shown in Figures 5.5 (a),(d) in Chapter 5, and is included for comparison. As shown in Figure 6.1, increasing the evaporated RbF thickness on the as-coated film has led to a marked increase in the grain size and the cross-sectional coarsened film thickness. As was demonstrated in Chapter 5, DAS-capped CIGS nanoparticle films are resistant to growth when selenized without any additional alkali treatments, with the

growth stagnating. Achieving significant grain growth requires the addition of sodium into the film, even at elevated growth temperatures, e.g. 575 °C.

The films in Figure 6.1 below suggest that Rb does show growth assisting behavior, with similar observations to Na (Chapter 5), and K (Chapter 3). This growth-assisting behavior of Rb treatments has not been reported in the literature, to the best of our knowledge. Moreover, Like Na, The film undergoes a step change in the coarsened thickness, with minimal difference between the 'No RbF' baseline and the 10 nm RbF samples. Increasing the RbF thickness to 20 nm increases the coarsened film thickness considerably, with a single grain that spans the thickness of the film. Figure 6.2 shows the atomic percentages of the films treated with RbF, extracted from XRF. The atomic percentages of RbF as a function of film thickness are markedly high, even with 10 nm RbF condition. Avancini et al. reported Rb at% for a CIGSe film grown via three-stage co-evaporation and subjected to RbF-PDT to be 0.1-0.2 at%, with evaporation of $\sim$ 30 nm RbF [75].
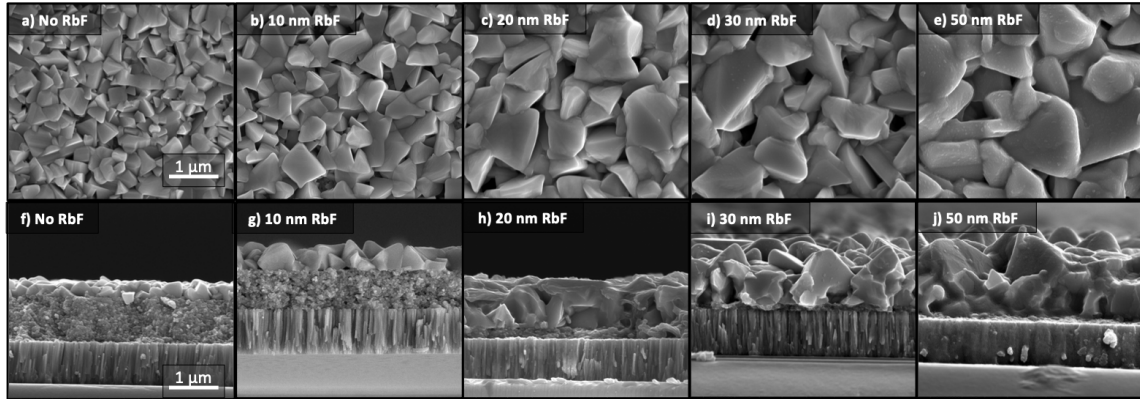
Figure 6.1. (a)-(e) Plan-view and (f)-(k) cross-sectional SEM images of CIGSSe films selenized from DAS-capped CIGS nanoparticle films at 500 °C for 20 minutes with different evaporated RbF film thicknesses prior to selenization: (a),(f): No RbF baseline; (b),(g) 10 nm RbF; (c),(h) 20 nm RbF; (d),(i) 30 nm RbF; (e),(j) 50 nm RbF. Scale bar is same for all images.

Figure 6.3 (a) the PL response of the films shown in Figure 6.1. Large increases in the PL intensity for the films treated with 20 nm and 30 nm, and 50 nm RbF, compared to the 10 nm RbF case. This suggests enhanced absorber quality and reduced non-radiative recombination in the films. Moreover, a red-shift in the PL of the 50 nm RbF sample, compared to all the other films, is observed. It is not clear at the moment what the source of this red shift is,
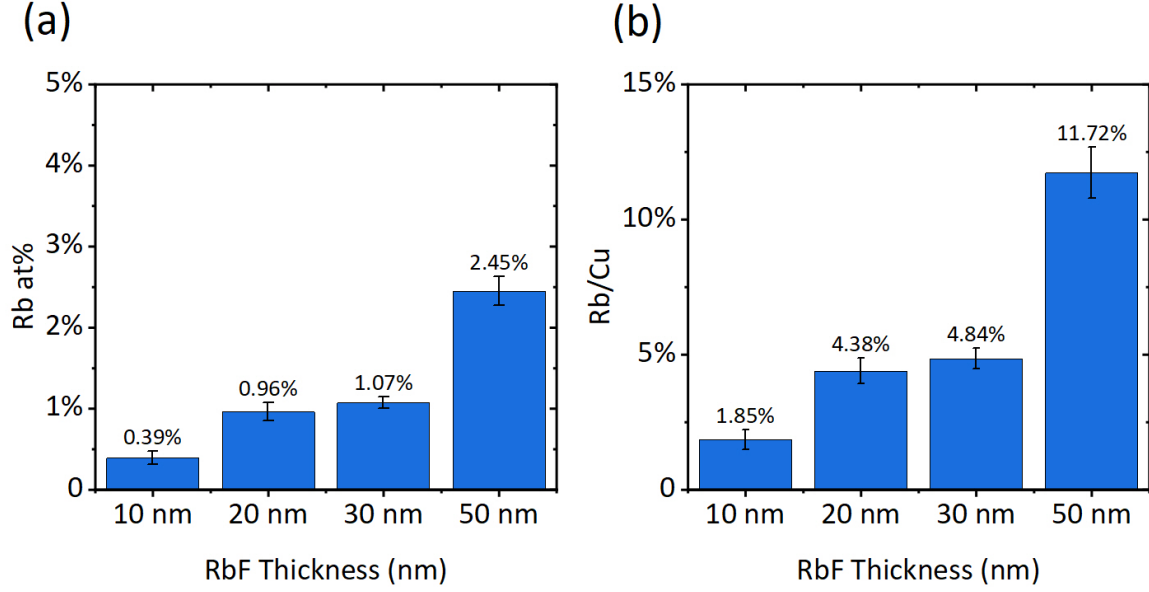
Figure 6.2. (a) Rb at% in CIGSSe film selenized at 500 °C for 20 minutes with different evaporated RbF thicknesses. (b) (Rb at%)/(Cu at%) of the same films shown in (a). Elemental ratios are measured with XRF, and assumed film is composed of Cu, In, Ga, Se, and Rb.

but similar observations were seen in that bandgap difference (from differential EQE data) were observed as result of Na and K alkali treatments (Chapter 3). Furthermore, a widening in the PL peak is also observed in the 50 nm RbF case, which may be due defects in the film as a result of the elevated Rb content. That being said, it remains an area of study. Figure 6.3 (b) shows the Raman spectra of the RbF-treated films with peaks characteristic of chalcopyrite $Cu(In, Ga)Se_2$ [66].

The results shown in this chapter and in Chapter 3 suggest that for low-carbon DAS-capped CIGS nanoparticles, alkali treatments are required for a decent performing device, and that alkali post deposition (selenization) treatments (at low temperature) to obtain the electronic enhancements exclusively as is done in vacuum-based CIGSSe films, will not be adequate in CIGSSe films selenized from ligand-exchanged DAS-capped CIGS nanoparticle layers. The results above show that Rb can be utilized to obtain both the grain assisting effects required to fully grow the films, and obtain the electronic enhancements resulting from Rb treatments. That being said, CIGSSe devices selenized from Rb-treated DAS-capped CIGS nanoparticles are currently an area of study.
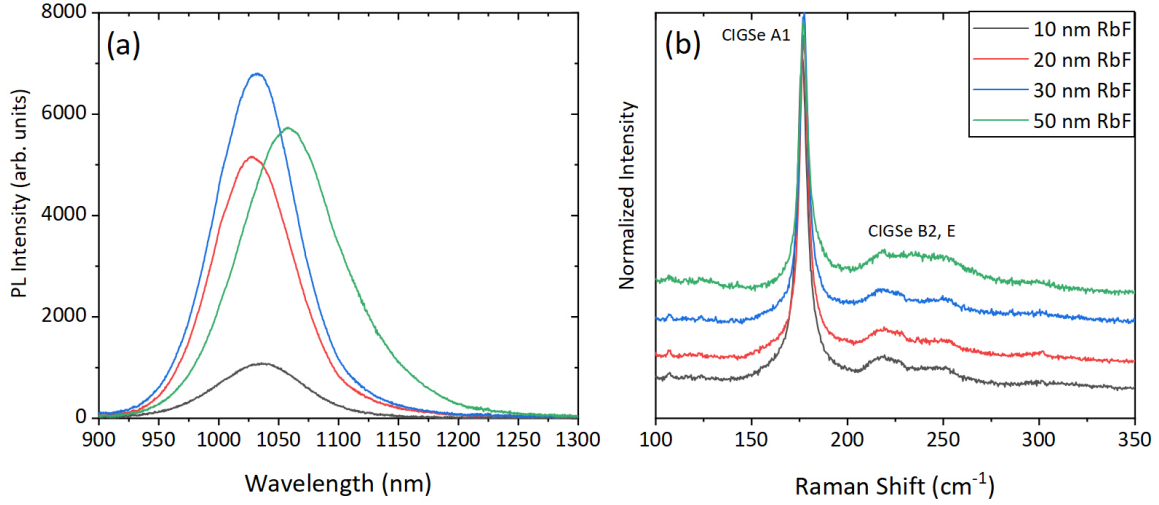
Figure 6.3. (a) PL spectra of CIGSSe films selenized from DAS-capped CIGS nanoparticle film at 500 °C for 20 minutes, with different RbF film thicknesses evaporated on the as-coated nanoparticle films. (b) Raman spectra of the films shown in (a).

6.4 Conclusion

In this chapter, Rb treatments are applied, pre-selenization, to DAS-capped $Cu(In, Ga)S_2$ nanoparticles. It was found that Rb, like Na and K, contributes to growth-assisting behavior of CIGS into CIGSSe, and that a CIGSSe with larger coarsened grain size and minimal unsintered 'fine grain' layer is achieved with Rb treatments. Moreover, enhanced CIGSSe film quality is obtained with Rb treatments, characterized by enhanced PL responses. CIGSSe solar cell devices with Rb treatments are currently an area of study.

7. PRELIMINARY WORK ON THE IMPLEMENTATION OF A GALLIUM GRADIENT IN CIGSSE FILMS SELENIZED FROM OLA-CAPPED CIGS NANOPARTICLES

7.1 Introduction

One of the beneficial properties of the $Cu(In, Ga)(S, Se)_2$ system is the ability to tune the bandgap by adjusting the gallium content, relative to indium, with pure-phase $CuInSe_2$ and $CuGaSe_2$ having bandgaps of 1.0 eV and 1.7 eV, respectively [137]. To date, the most common and the most successful routes to fabricate CIGSe absorber layers are vacuum-based processes such as the well-known three-stage co-evaporation process [3], [17], [33]. As described in Chapter 1, the three-stage process consists of the evaporation of Cu, In, and Ga metals, in the presence of Se, onto a Mo-coated substrate in a vacuum chamber at an elevated temperature (T $\geq$ 550 °C) [17], [18]. One of the reasons that the three-stage co-evaporation process produces high efficiency CIGSe devices is that the kinetics of the process introduces a double gradient in Ga throughout the thickness of the film, so-called 'double graded profile', where the GGI ratio (bandgap) decreases from the back contact to a minimum just before the space-charge region, after which it increases towards the junction [18].

Having a gradient in the Ga content relative to In produces a graded bandgap variation structure the depth of the absorber layer. This in turn produces an electrical field that drives away the photoelectrons from regions with higher probability of surface recombination, i.e. Mo-CIGSe and CIGSe-CdS junctions, and thus reducing interfacial recombination. However, the larger bandgap near the junction will also lead to reduced carrier collection. That being said, the graded bandgap also provides field-assisted carrier collection for photoelectrons generated in the bulk region away from the SCR. The effects of Ga grading in CIGSe solar cells is analogous to the back-surface field that is utilized in Si solar cells, where a higher doped region close to the back contact is utilized to drive away minority carriers.

Figure 7.1 shows a simple band-diagram schematics of an ungraded, single-graded, and a double-graded CIGSSe films, and their corresponding gallim profiles. In general, increasing

the amounts of heavier group III elements, e.g. In, will lower the bandgap by lowering the conduction band minimum [138].
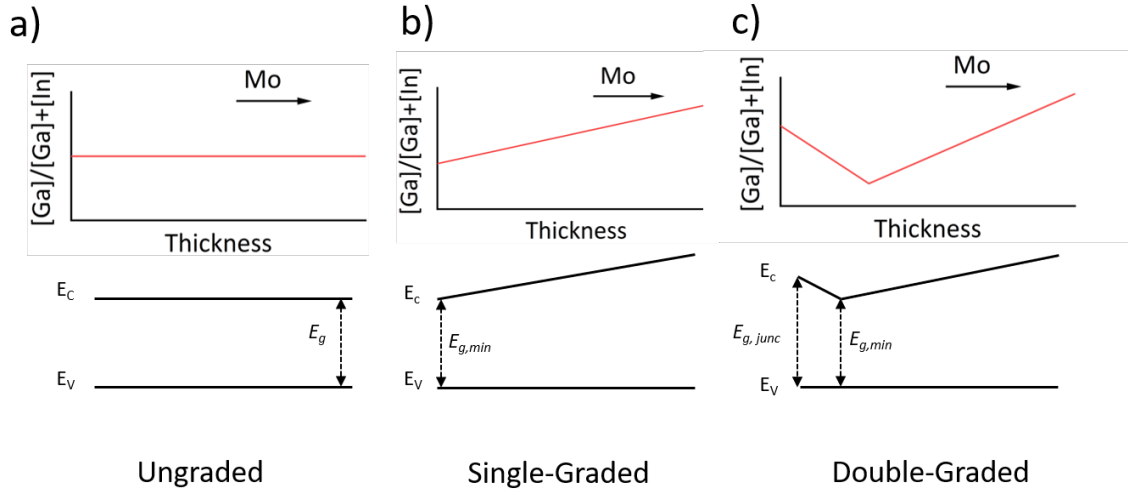
Figure 7.1. GGI ratios as a function of CIGSe film thickness and corresponding band diagrams of (a) ungraded CIGSe, (b) single graded CIGSe, and (c) double graded CIGSe. E_C, E_V, and E_G refer to the conduction band minimum, valence band maximum and bandgap, respectively. $E_{g,\ min}$ and $E_{g,\ junc}$ refer to the minimum bandgap in the absorber and the bandgap at the p-n junction, respectively.

High performance CIGSe devices typically employ a 'double graded' structure, in which the Ga content, or bandgap, decreases towards the space-charge region reaching a minimum at 500 nm before the junction, and increases again towards the junction. Dullweber et al. have shown the effect of different grading profiles on the performance CIGSe grown by co-evaporation [139]. They have shown that devices with a single linear grading, such as the one shown in Figure 7.1 (b), had substantial effects on both the V_{OC} and J_{sc} of the final device. The Ga grading mainly improves the open-circuit voltage of the device by decreasing the recombination at the interfaces. However, having a large bandgap near the interface will also lead to lower photo-carrier generation, and to a decrease in the short-circuit current. Dullweber et al. have also shown that the J_{sc} of the final device is mainly determined by the minimum bandgap (minimum Ga content) in the device, while the V_{OC} is determined by the bandgap at the CIGS surface (p-n interface) [140]. Varying the S-to-Se ratio can also be used to introduce a graded bandgap profile. The world-record 23.35% CIGSSe by Solar

116

Frontier employs a double graded bandgap profile using both Ga and chalcogen variation with their Sulfurization-After-Selenization process; Ga decreases monotonically towards the junction (single Ga gradient, Figure 7.1 (b)), while the top-layers of the film are sulfurized in H_2S, thus increasing the S-to-Se ratio, i.e. bandgap, close to the surface [21], [31].

For solution-processed solar cells, the 15% nanoparticle CIGSSe solar cell reported by McLeod et al. employs an unintentional Ga single gradient, with Ga amounts higher near the back-contact [47]. Moreover, Zhang et al. also reported an increase in efficiency of 2.5% absolute of a double graded hydrazine-based solution-processed CIGSSe over an ungraded device fabricated using the same manner [46]. The improvements are mainly manifested in an increase in V_{OC}, J_{sc}, and FF.

7.2   Scope of this chapter

A graded bandgap profile is a requirement for high-efficiency CIGSSe devices [18]. An important feature of the three-stage co-evaporation process is that the metal deposition and film growth occur simultaneously, and that the elemental profiles in the final film can be altered by altering their deposition (evaporation) rates *as the film is grown.* In solution-processed routes, the material (metal) deposition is done prior to film growth at high temperature. To introduce a Ga gradient in fully-grown film, the Ga profile in the precursor film must be designed to account for elemental diffusion that occurs in the final coarsened film, especially when using liquid-assisted growth regimes [47], [55], [115]. The grading profile in the film will need optimization as it is a trade-off between high current collection and high open-circuit voltage. However, the goal of this chapter is to investigate how the Ga (bandgap) profile develops during selenization and grain growth, when starting from the extreme case of a bi-layer CGS/CIS nanoparticle film. The graded nanoparticle film is composed of a thin $CuGaS_2$ nanoparticle layer underneath a thicker $CuInS_2$. We found that the graded profile is annihilated during the selenization and grain growth process, and that the time required for Ga equalization is a function of the selenization temperature, with equalization occurring earlier in the growth process when selenized at higher temperatures. Employing a two-step selenization and grain grain growth process was found to preserve, to a degree, the

117

Ga gradient, and at the same time produce a large-grained CIGSSe film. Finally, devices with single graded profiles are fabricated.

7.3 Methods and Materials

The methods described herein are adapted from McLeod et al. [47] and Guo et al. [54], [109] with modifications. The experimental outline is given below.

7.3.1 Nanoparticle Synthesis

Graded $Cu(In, Ga)(S, Se)_2$ absorber layers were fabricated from thermally sintering stacked nanoparticle layers of $CuGaS_2$ (CGS) and $CuInS_2$ (CIS) in the presence of excess selenium. The CGS and CIS nanoparticles were synthesized in separate hot-injection reactions. Reagents used in nanoparticle synthesis are sulfur (99.99%, Sigma Aldrich), copper(II) acetylacetonate ($Cu(acac)_2$, 99.9%, Sigma-Aldrich), indium acetylacetonate ($In(acac)_3$, 99.99%, Sigma-Aldrich), gallium acetylacetonate ($Ga(acac)_3$, 99.99%, Sigma Aldrich), oleylamine (OLA, $\geq$ 98% primary amines, Sigma Aldrich). All reagents were stored in a nitrogen-filled glovebox, and were used as received with the exception of oleylamine. The OLA was first degassed via freeze-pump-thaw process, and then stored in a N_2-filled glovebox. In the CIS nanoparticle synthesis, a three-neck flask containing 1.38 mmol of $Cu(acac)_2$, 1.5 mmol of $In(acac)_3$, and 12 ml of degassed OLA was prepared and sealed in a N_2-filled glovebox. Simultaneously, a 6 ml solution of sulfur in oleylamine (S-OLA) solution (1 M) was also prepared in a separate flask and sealed in a N_2-filled glovebox. The two flasks were taken out of the glovebox, and the three-neck flask was attached to a Schlenk line, and set on a stir plate and a heating mantle. The 15 ml flask was stirred and kept on a hotplate at 65 °C to dissolve all the sulfur.

To ensure an inert atmosphere during the reaction, a total of six vacuum/Ar purge cycles were performed on the metal-OLA solution in the flask, three of vacuum/Ar purge cycles were conducted at room temperature, and the other three were performed at 140 °C. After the sixth Ar purge cycle at 140 °C, the reaction temperature was increased to 285 °C. At 285 °C, 4.5 ml of the 1 M S-OLA solution was injected into the flask containing the metal

118

salts and oleylamine. The temperature of the flask was maintained at 285 °C for 30 minutes under an inert Ar atmosphere. After the reaction, the heating mantle was removed and the flask was cooled naturally to room temperature, also under Ar atmosphere. During the initial Ar purges, heat up, reaction, and cooldown segments, the flask contents were stirred with a magnetic stir bar at 800 rpm.

The reaction product was then extracted from the flask and mixed with a solution of hexanes and alcohols (isopropanol and methanol), and centrifuged three times to remove excess OLA and any unreacted precursors. The nanoparticles were then dried under inert Ar for 20 minutes, and subsequently stored in an inert atmosphere.

CGS nanoparticles are synthesized using the same method and process as the CIS nanoparticles, with the only change being the replacement of In(acac)$_3$ by Ga(acac)$_3$.

7.3.2 Nanoparticle Film Coating and Growth

The synthesized CIS and CGS nanoparticles were suspended in hexanethiol forming the CIS and CGS colloidal nanoparticle inks, respectively. The concentration of the nanoparticle suspension is 250 mg/ml for the CIS nanoparticle ink and 236 mg/ml for the CGS nanoparticle ink. Figure 7.3 (a) shows a schematic of the nanoparticle film stack. The nanoparticle film was formed by coating four layers of 15 μl each of the nanoparticle ink onto a Mo-coated soda lime glass substrate using the doctor blade technique. To achieve the Ga gradient in the nanoparticle film, 15 μl of CGS nanoparticle ink is coated as the bottom layer. The top three layers were coated with 15 μl of CIS nanoparticle ink each. After each coating, the film was heated at 300 °C to evaporate the hexanethiol and excess organics. The CIS and CGS nanoparticles were OLA-capped, and used as-synthesized without a ligand exchange procedure. Prior to selenization 20 nm of NaF is evaporated onto the nanoparticle film via electron-beam evaporation to enhance grain growth [55], [56], [112]. The graded nanoparticle films were selenized in the rapid thermal processing furnace (RTP) as outlined in Chapter 5, and Appendix A.

7.3.3 Device Fabrication

For device fabrication, 50 nm of CdS was deposited onto the selenized CIGSSe films via chemical bath deposition to form the p-n junction. Following, 80 nm of ZnO and 220 nm indium-doped tin oxide TCO layers were deposited by RF sputtering. Lastly, devices were finished with deposition of Ni-Al metallic grids via e-beam evaporation. No MgF_2 anti-reflective coating is used.

7.3.4 Characterization

Theta-2theta powder x-ray diffraction is performed using a Rigaku SmartLab Diffractometer in Bragg- Brentano mode with Cu K_α radiation at 40 kV and 44 mA. FEI Quanta 3D FEG Dual-beam scanning electron microscope (SEM) with an energy dispersive X-ray (EDS) detector was used for imaging top-down and cross-sectional images of the films, as well as to conduct EDS elemental analysis of the films. All measurements were taken at room temperature. Unless otherwise stated, all EDS line-scans were performed using 10 keV accelerating voltage, and utilizing L-lines exclusively for In and Ga to reduce probed depth. Cross-sectional EDS linescans compositions for each film are average values of compositions from three different regions of the each respective film.

7.4 Results
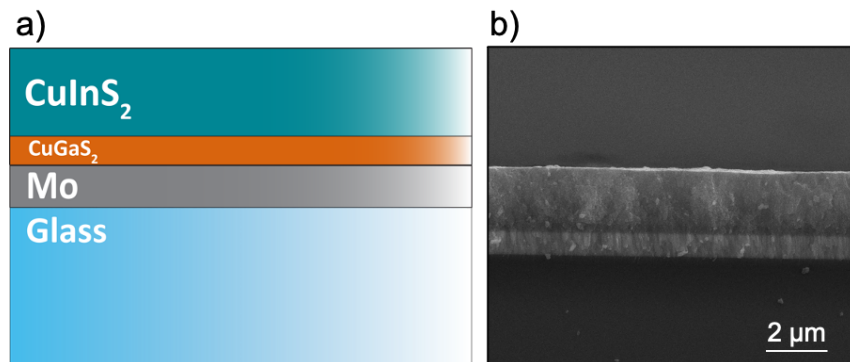
Figure 7.2. (a) Diagram of the graded nanoparticle film stack. (b) SEM cross-sectional image of the nanoparticle film stack.

Figure 7.3 (a) shows a schematic of the graded nanoparticle film composed of a thin layer of $CuGaS_2$ below a thick layer of $CuInS_2$. Figure 7.3 (b) shows an SEM cross-sectional image of graded film prior to growth. The film is relatively flat with a thickness of ≈ 2 μm. Figure 7.3 (a) shows the XRD pattern of the as-coated nanoparticle film, with peaks attributed to chalcopyrite $CuInS_2$ and $CuGaS_2$, with no other crystalline phases observed. Figure 7.3 (b) shows the [Ga]/[In]+[Ga] (GGI) and [In]/[Ga]+[In] ratios, extracted from EDS line scans of the film cross-section, as a function of thickness of the as-coated nanoparticle film showing a sharp decrease in Ga towards the film surface. Note that the theoretical spatial resolution of the EDS scan at 10 keV accelerating voltage (used here) is $\approx$ 400 nm.[1].
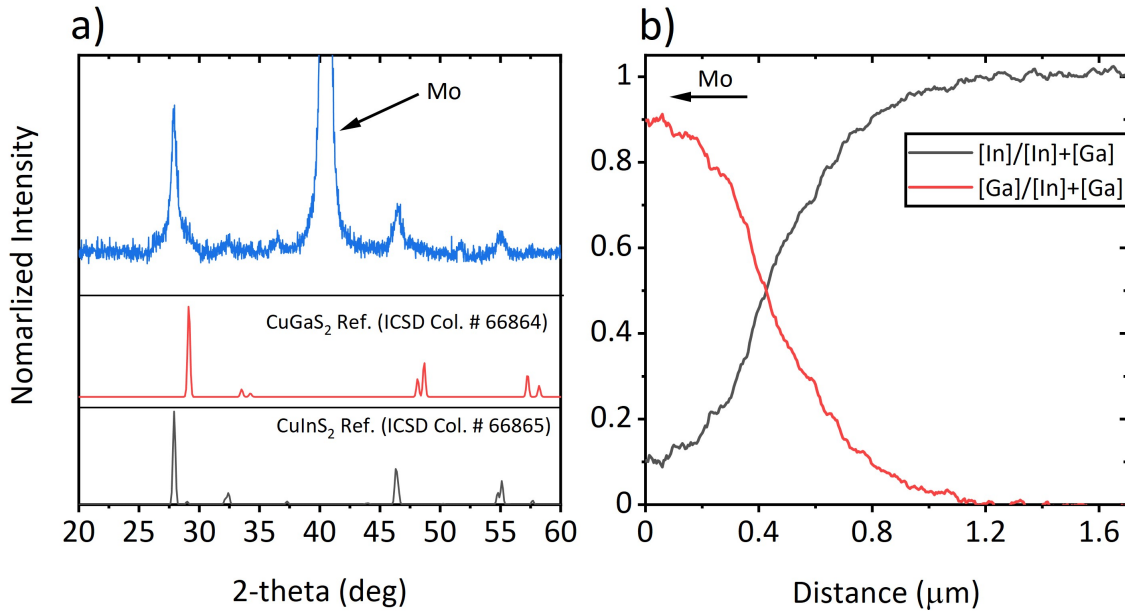
Figure 7.3. (a) XRD pattern of as-coated graded nanoparticle film, with $CuInS_2$ and $CuGaS_2$ references. (b) [Ga]/[In]+[Ga] and [In]/[Ga]+[In] as function of the film thickness, extracted from EDS linescans of the film cross-section.

To investigate how the Ga gradient develops during selenization, the nanoparticle film is selenized for 2 minutes, 4 minutes, and 10 minutes at 500 °C and 550 °C sample temperatures. The sample was selenized in a three-zone rapid thermal processing furnace (shown in Chapter 5. See Appendix A for a representative temperature-time plot of an RTP run). During the

---

[1]Calculated using CASINO electron trajectory simulation software, made available by Dominique Drouin of the University of Sherbrooke [141]

run, the Se temperature is maintained 25 °C higher than the sample to ensure adequate Se delivery to the film. After the selenization run, the substrate is cooled naturally ($\approx$ 25 °C/min) using the RTP.

Figure 7.4 (a), (b), and (c) show the [Ga]/[In]+[Ga] ratio with respect to the depth of the film for selenized for 2, 4, and 10 minutes, respectively, at 500 °C substrate temperature. In the 2-minute selenized sample (Fig 7.5 (a)), the Ga (GGI) profile is shallower compared to the precursor nanoparticle film (Fig. 7.4 (b)), indicating that as the selenization and grain growth proceeds, Ga is diffusing within the film. As the selenization duration increases to 4 minutes (Fig 7.5 (b)), the Ga gradient is reduced significantly across the film thickness as the Ga profile is equilibrated due to metal diffusion during the high-temperature treatment. For the 10-minute selenization condition (Fig. 7.5 (c)), the Ga gradient is almost annihilated across the thickness of the film. However, an 'inversion' in the Ga gradient is observed, with the [Ga]/[In]+[Ga] increasing towards the surface of the film rather than decreasing. The source of this 'inversion' of the grading is not entirely clear. It may be a result of how grain growth starts and proceeds in OLA-capped sulfide-based nanoparticle films [55], [115]. As the selenide grains nucleate on the surface of the film, metals (Cu, In, Ga) diffuse from the bulk towards the surface and incorporate into the growing front [55].
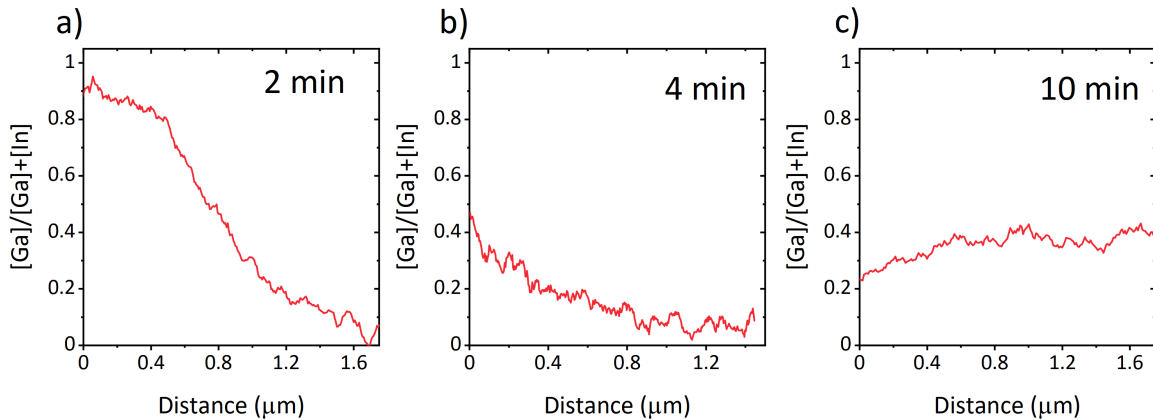
Figure 7.4. [Ga]/[In]+[Ga] ratios as a function of thickness of CIGSSe films selenized from a graded CIGS nanoparticle film at 500 °C with Se at 525 °C for (a) 2 minutes, (b) 4 minutes, and (c) 10 minutes. In all plots, zero point on the x-axis refers to the Mo-CIGSSe interface.

Figure 7.5 (a), (b), and (C) show the [Ga]/[In]+[Ga] ratio with respect to the depth of the film for selenized for 2, 4, and 10 minutes, respectively, for nanoparticle films selenized at 550 °C, with Se at 575 °C. Similar observations as in the 500 °C set of samples (Fig 7.5) can be deduced for the 550 °C case. The gallium diffuses throughout the film, and the grading is annihilated earlier when compared to the 500 °C set. This is expected due to the increased diffusion rate at the higher temperature. The Ga content throughout the film is almost uniform even for the 2-minute selenized sample. By reaching 4-minutes, the Ga profile is flat, and no grading can be observed from EDS data indicating that the Ga content is uniform throughout the entire film. The Ga profile in the film that was selenized for 10 minutes does not show any appreciable difference from the sample selenized for 4 minutes indicating an equilibrium state is reached within 4 minutes of selenization at 550 °C.
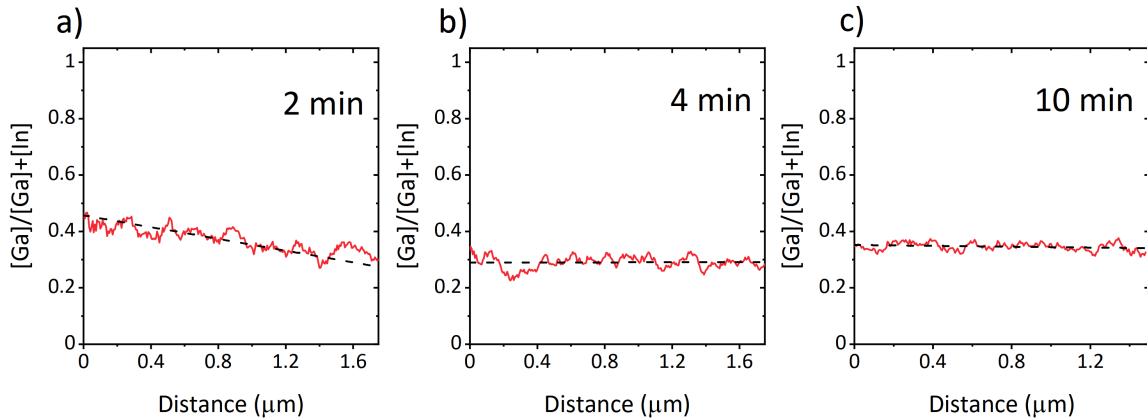
Figure 7.5. [Ga]/[In]+[Ga] ratios as a function of thickness of CIGSSe films selenized from a graded CIGS nanoparticle film at 550 °C with Se at 575 °C for (a) 2 minutes, (b) 4 minutes, and (c) 10 minutes. In all plots, zero point on the x-axis refers to the Mo-CIGSSe interface.

7.5   Discussion

The preceding results suggest that during selenization and grain growth of OLA-capped CIGS nanoparticles into coarsened CIGSSe grains, Ga diffusion and equalization within the film occurs early during film growth, earlier than the full coarsening of the film. This issue is not observed in the three-stage co-evaporation process where a single Ga gradient is

developed (at the end of the Cu-rich second stage) due to the lower diffusion of Ga in the film compared to In [142]–[144]. In the present case, the fact that a precursor film has to be deposited prior to selenization and grain growth presents challenges as diffusion of metals has to be taken into account. Moreover, the 'top down' growth behavior of CIGS nanoparticles also influences the gradient development. Hages et al. and McLeod et al. have suggested that during the selenization of OLA-capped nanoparticles, liquid-phase selenium penetrates the film through capillaries in the film [55], [115]. Metals would then diffuse through the liquid Se in the nanoparticle towards the surface and incorporate into the growing grains, and simultaneously rejecting carbon towards the bottom of the film [55], [115]. This is in contrast to bulk-growth seen in vaccuum-based CIGSe growth [144]. Zhang et al. did show that solution-processed CIGSSe cell fabricated using the hydrazine route also retained the Ga gradient post-selenization [46]. However, their exact selenization method and conditions are not reported [46].

7.6   Two-step Selenizations

The current hypothesis is that the annihilation of the gradient after selenization may be a result of top-down growth behavior observed in sulfide-based nanoparticle selenization and growth growth. The selenization and grain growth of sulfide-base $Cu(In, Ga)S_2$ is a two step process: the first is the selenization step in which the sulfide $Cu(In, Ga)S_2$ is converted to selenide $Cu(In, Ga)Se_2$, and the second is the coarsening of the selenide $Cu(In, Ga)Se_2$ into large grains. The top-down growth regime has been suggested to be a result of the sulfide to selenide transition, as the sulfide CIGS breaks down and re-constitutes into selenide CIGSe, and that grain growth happens at a free surface in the presence of Se [55], [115].

The hypothesis is that conducting the selenization and grain growth steps separately as a two-step process will suppress some of the intermixing. The anneling process will consist of a low temperature selenization step (pre-growth step), and a high temperature grain growth step (growth-step). The initial CIGS nanoparticle film is relatively porous allowing liquid Se to penetrate into the film, which would accelerate diffusion and intermixing [55], [115]. In low-temperature selenization (pre-growth) step, the film is converted from sulfide $Cu(In, Ga)S_2$ to selenide $Cu(In, Ga)(S, Se)_2$, and the nanoparticle film is coarsened to reduce

its porosity. In the high temperature step, grain growth occurs. Diffusion is hypothesized to be reduced due to lower liquid Se penetration into the film because of the lower porosity.

7.6.1 Pre-Growth Stage

To investigate the pre-growth step and its impact on the gradient development, a graded CIGS nanoparticle film is selenized at temperatures (300 °C $\leq$ T_{sample} $\leq$ 450 °C) for 5 minutes, with Se 10 °C higher than the sample temperature. Figure 7.6 shows the SEM plan view and cross-sectional images of CIGSSe films subjected to the pre-growth conditions. In the 300 °C, 350 °C, and 400 °C, very little nucleation is seen on the surface of the films, and no grains can be seen in the cross-section of the films. However, in the 450 °C condition, grain nucleation can be observed on the film surface, similar to what is observed during the initial stages of liquid-assisted grain growth of CIGS nanoparticles into CIGSe coarsened grains [55]. Figure 7.7 shows the XRD patterns of the films after pre-growth treatments. At 300 °C and 5 minutes pre-growth condition, very little change is observed in the crystallinity (peak FWHM), and no shift towards low 2-theta corresponding to CIGS to CIGSe is observed. At 350 °C, peaks at lower 2-theta degree begin to appear indicating formation of selenide CIGSe, along with presence of sulfide CIGS. At 400 °C, the selenide peak is sharper indicating increased crystallinity of the selenide phase. At 450 °C, 5 minutes, the sulfide-to-selenide transition is complete, as shown by the (112) and (220/204) peaks in the PXRD pattern at 26.8°and 44.8°, respectively. Figure 7.8 shows the GGI profile of the films shown in Figure 7.6. In all pre-growth temperature conditions, the gradient is retained. With the exception of the 450 °C condition, little change in the Ga profile is observed, compared to the precursor nanoparticle film shown in Figure 7.3 (b).

Selenizing the sulfide-based graded nanoparticle film at 400 °C for 5 minutes results in a selenide film with minimal nucleation on the surface and in the bulk, while also maintaining the gallium profile. Pre-growth at 400 °C (Se at 420 °C) is further explored. Figure 7.9 shows the SEM plan-view and cross-sectional images of CIGSSe films subjected to annealing in a Se atmosphere at 400 °C (Se at 420 °C) for 3, 10, and 20 minutes. In the 3-minute (Figure 7.9 (a),(d)) and 5-minute (Figure 7.6 (c),(g)) conditions, only minimal surface nucleation is observed, whereas formation of a thin coarsened layer can be seen in the 10 and 20 minutes
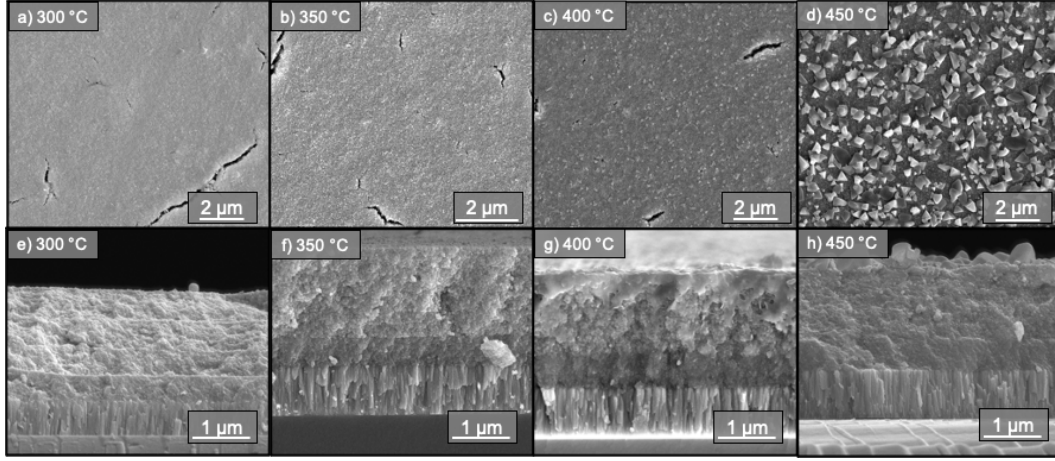
Figure 7.6. Plan view and cross-sectional SEM images of CIGSSe films selenized from a CIGS nanoparticle film for 5 minutes at (a),(e) 300 °C; (b),(f) 350 °C; (c),(g) 400 °C; and (d),(h) 450 °C. In all conditions, Se temperature is 20 °C higher than the sample temperature.

conditions. Figure 7.10 shows the PXRD patterns of the films shown in Figures 7.7 (c),(g) and 7.10. The 10 and 20 minute conditions show are significantly more crystalline than the 3 and 5-minute conditions, with sharper and more prominent peaks. CISe and CGSe phase segregation is still present as shown by shoulder peak at $\sim 28°$in Figure 7.10. Figure 7.11 shows the GGI ratios of the CIGSSe films shown in Figure 7.9 and 7.7 (c),(g), extracted from EDS data. In all durations, the Ga gradient is still present and not completely annihilated. However, small amounts of Ga can be detected on the surface of the films for the 10 and 20-minute conditions.

The goal of the pre-growth step is to convert the sulfide film to selenide, while minimizing Ga diffusion within the film at this stage. The 400 °C, 5 minute condition is suitable as we observe CIGS-to-CIGSe conversion while still maintaining the Ga profile in the film.

7.6.2 Grain Growth Stage

The goal of the grain growth stage in the present context is to coarsen the film (minimize grain boundaries) and preserve the Ga gradient. To investigate the behavior of Ga and the development of the Ga grading as the sample is heated to $T \geq 500$ °C, a set of different grain growth conditions were attempted: 500 °C, 15 minutes; 550 °C, 5 minutes; and 550

126
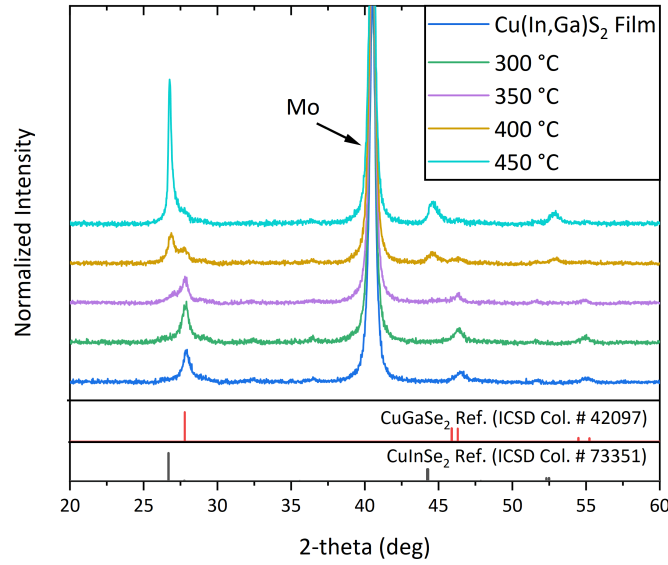
Figure 7.7. PXRD patterns of CIGSSe films subjected to a pre-growth annealing step in the RTP at different temperatures for 5 minutes. In all conditions, the Se temperature is set 20 °C higher than the sample. PXRD pattern of sulfide nanoparticle film is also added for comparison.

°C, 10 minutes. In all conditions, the Se temperature is set 10 °C higher than the sample temperatures, and all sample conditions were subjected to a pre-growth stage of 400 °C (Se at 420 °C) for 5 minutes. Figure 7.12 shows a representative temperature heating profile.

Figure 7.13 shows the SEM plan-view and cross-sectional images of the different grain growth conditions attempted, while Figure 7.14 shows the GGI ratios of the various conditions, extracted from EDS measurements on the film's cross-section. The $Cu(In, Ga)(S, Se)_2$ films obtained at the end of the grain growth stage show a film with bi-layer morphology that is characterized by large-sized grains (especially the samples that were grown at 550 °C) that span most of the thickness of the film, atop a fine grain layer. EDS measurements of the GGI ratio show that for the 15-min, 500 °C and the 10-min 550 °C conditions, the initial Ga profile that was present before the second stage (Figure 7.11 (b)) is annihilated, and that the same Ga inversion is seen here, as was present in the single step 10-min, 500 °C condition (Figure 7.4 (c)). The GGI profile for the 5-min, 550 °C condition (Figure 7.14 (c)) does exhibit a Ga-graded profile decreasing towards the surface of the film, while its film

127
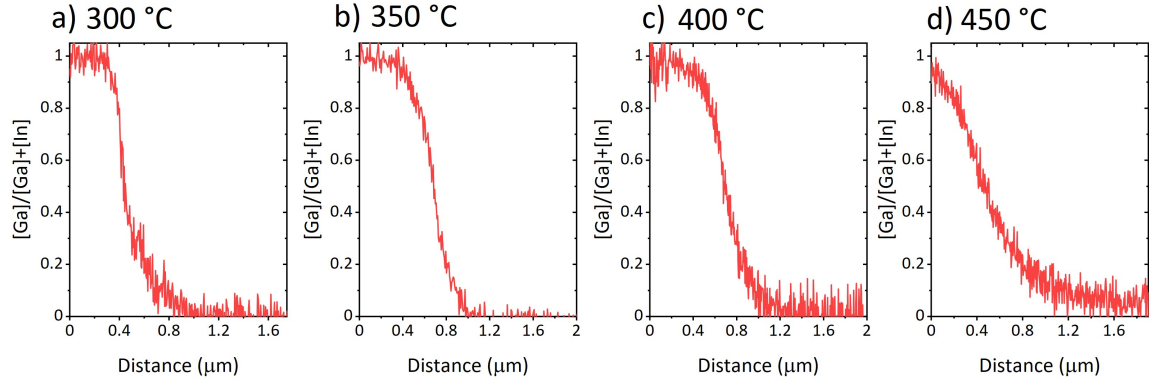
Figure 7.8. [Ga]/[In]+[Ga] profiles of CIGSSe film selenized from a graded CIGS nanoparticle film annealed in a Se atmosphere for 5 minutes at (a) 300 °C, (b) 350 °C, (c) 400 °C, and (d) 450 °C. In all conditons, Se temperature is 20 °C higher than the sample temperature.

morphology is characterized by a coarsened CIGSSe layer (Figure 7.13 (b),(e)). Comparing the GGI ratios of the films that were selenized via the two-step growth (Figure 7.14 (b)) to the films that were selenizied via a single step (Figure 7.4 and Figure 7.5) suggest that diffusion is reduced, while film morphologies are representative of a fully coarsened CIGSSe film.

Implementing a Ga gradient to a film that is selenized and grown after the whole precursor film is coated (i.e. overall material of the film is present when the film is grown) is challenging. One approach to mitigate this is to alternate between coating and annealing for each layer, with different layers having different GGI ratios, similar to what is demonstrated by Zhang et al.[46]. However, the presence of carbon in the film would render this approach difficult to implement for OLA-capped nanoparticles as the excess carbon from the oleylamine would segregate in between different layers. A possible solution is to rely is utilize ligand-exchanged nanoparticles that contain minimal amounts of carbon, or to utilize a moelcular precursor approach rather than a nanoparticle-based approach.

7.7   Device Performance

Devices were fabricated using the conventional stack Mo/CIGSSe/CdS/i-Zno/ITO/Ni-Al. Figure 7.15 shows the illuminated J-V plots of an ungraded CIGSSe film compared to
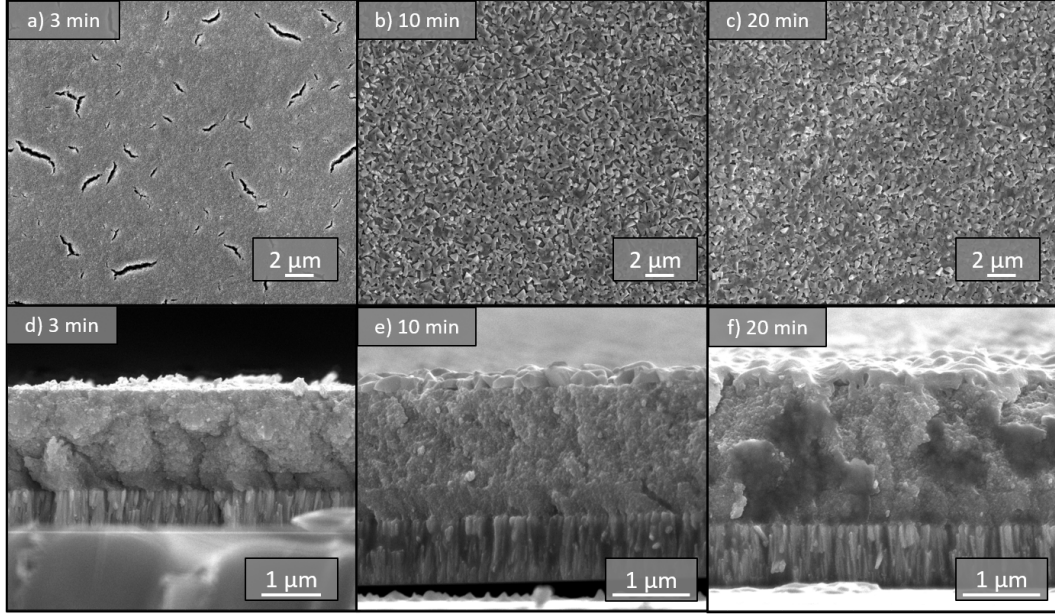
Figure 7.9. SEM plan-view and cross-sectional images of CIGSSe film selenized from a graded CIGS nanoparticle film at 400 °C (Se at 420 °C) for (a),(d) 3 minutes; (b),(e) 10 minutes; and (c),(f) 20 minutes.

a graded film with the same thickness (SEM cross-sectional images of the absorber layer is shown in Figure (b),(e)). The graded device shows higher short-circuit current density (31.2 mA/cm²) compared to the ungraded device (29.8 mA/cm²), however the open circuit voltage and the fill factor are higher in the ungraded device. Figure 7.16 shows EQE and differential EQE data for both devices. The graded device shows higher current collection in the low-energy (high wavelength) regions, compared to the ungraded case. The *effective* bandgap of the device can be estimated from the inflection point, in the vicinity of the bandgap, of the EQE vs. wavelength plot, i.e. the maximum in a plot of $|d(EQE)/d\lambda|$ vs. wavelength [56], [115]. The estimated bandgap is 1.13 eV and 1.18 eV for the graded and ungraded cases, respectively.

The higher J_{sc} and higher current collection in the graded case may be explained by its lower bandgap compared to the ungraded case. However, the effective bandgap extracted from EQE data represents the minimum bandgap in the absorber film, i.e. the bandgap that corresponds to the lowest GGI ratio within the film [140]. Since both films have similar GGI ratios (from EDS and XRD data), it can be deduced that the increased current collection is
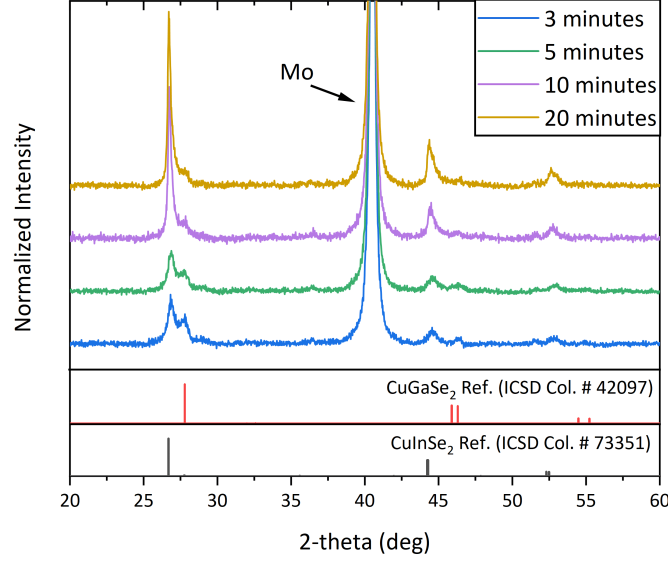
Figure 7.10. PXRD patterns of CIGSSe films subjected to a pre-growth annealing step in the RTP at 400 °C, with Se at 420 °C, for different durations.

due to the presence of a Ga grading within the film. That also explains the low V_{OC} value of the graded film as the films in the present case are single-graded, and the V_{OC} of the device is determined by the bandgap at the p-n (CIGS-CdS) interface [140]. Table 7.1 summarizes device performance data for each condition.

Table 7.1. Device performance parameters for CIGSSe devices selenized from a graded and an ungraded nanoparticle layer. All efficiencies are based on total cell area. No MgF_2 anti-reflective coating is used.

Condition	η (%)	V_{OC} (V)	J_{sc} (mA/cm^2)	FF (%)	$E_{g,min}$ (eV)
Graded 2 μm	7.0	0.44	31.2	50.7	1.13
Ungraded 2 μm	9.5	0.54	29.8	58.8	1.18

7.8 Conclusion

Preliminary investigation on the development of single Ga gradient during the selenization process was conducted. Starting from an extreme case of bi-layer $CuGaS_2$ and $CuInS_2$
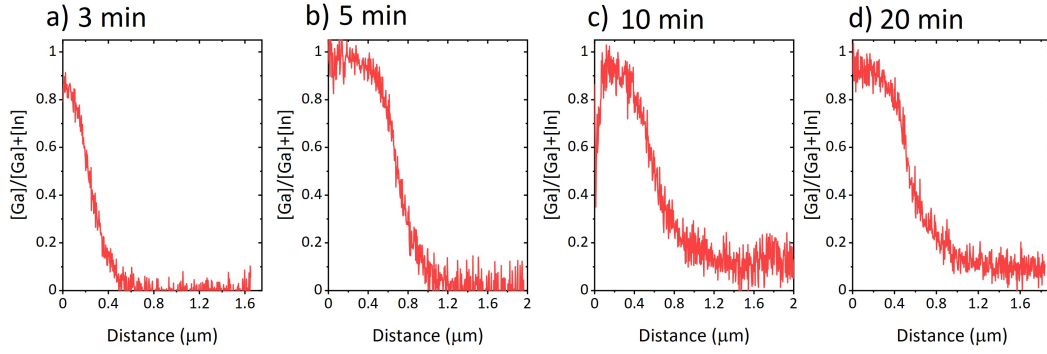
Figure 7.11. [Ga]/[In]+[Ga] profiles of CIGSSe film selenized from a graded CIGS nanoparticle film at 400 °C (Se at 420 °C) for (a) 3 minutes, (b) 5 minutes, (c) 10 minutes, and (d) 20 minutes.

nanoparticle film, it was found that the Ga profile that is present in the film is annihilated relatively fast during the selenization and grain growth process. Ga equalization was found to be a function of the anneal temperature and duration, with higher temperatures leading to faster elemental equalization within the film. The hypothesis is that the annihilation is caused by the very high rates of metal diffusion at the high temperatures used in the grain growth process.

Pre-annealing the nanoparticle film at a lower temperature prior to growth has shown to be effective in slowing the elemental diffusion within the film and in preserving the gradient. The hypothesis is that the pre-annealing coarsened the film reducing its porosity, which would reduce liquid Se penetration into the film, and thus reduce elemental diffusion. The two-step annealing resulted in a film characterized by large grains, and a bi-layer morphology consisting of a single-grain coarsened layer above a carbonaceous fine grain layer. Fabricating devices, it was found that the graded film has higher current collection due to the gradient, but lower V_{OC} and *FF*.
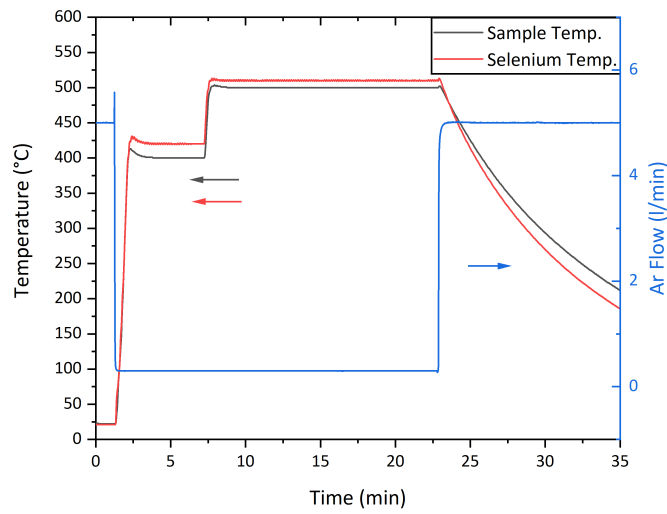
Figure 7.12. Temperature profile of a selenization and grain growth experiment conducted in the RTP of CIGSSe film selenized from a grade CIGS nanoparticle via two-step annealing, with the first step conducted at 400 °C (Se at 420 °C), for 5 minutes; and the second step at 500 °C (Se at 510 °C), for 15 minutes. Ar flow is set at 0.3 l/min during both heating steps.
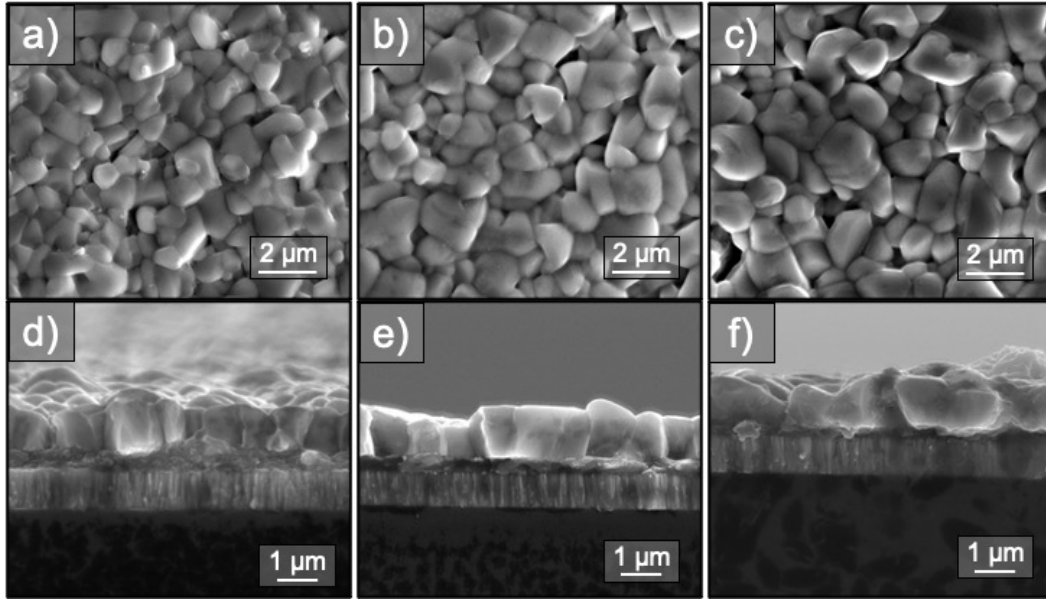
Figure 7.13. SEM plan-view and cross-sectional images of CIGSSe films selenized from a graded CIGS nanoparticle film via two-step selenization with different grain growth step conditions: (a), (d) Sample at 500 °C, Se at 510 °C, for 15 minutes; (b), (e) Sample at 550 °C, Se at 560 °C, for 5 minutes; (c), (f) Sample at 550 °C, Se at 560 °C, for 10 minutes. In all conditions, the pre-growth step is at 400 °C (Se at 420 °C) for 5 minutes. All films had 20 nm NaF evaporated prior to selenization.
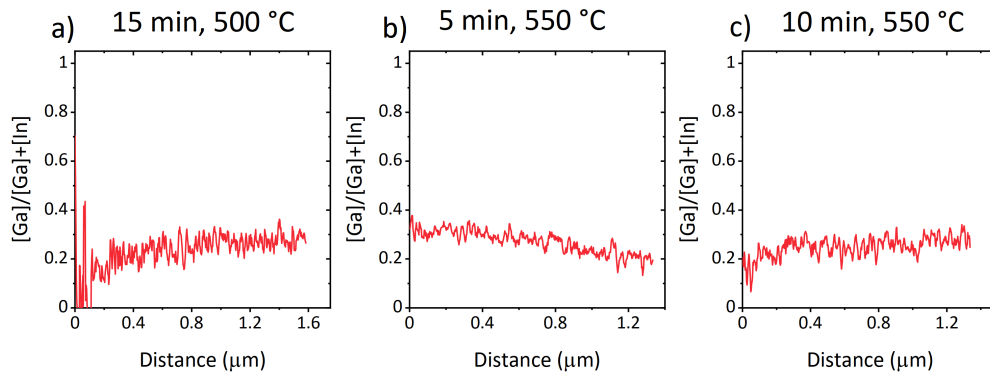
Figure 7.14. [Ga]/[In]+[Ga] ratios of CIGSSe films selenized from a graded CIGS nanoparticle film via two-step selenization with different grain growth step conditions: (a) Sample at 500 °C, Se at 510 °C, for 15 minutes; (b) Sample at 550 °C, Se at 560 °C, for 5 minutes; and (c) Sample at 550 °C, Se at 560 °C, for 10 minutes. In all conditions, the pre-growth step is at 400 °C (Se at 420 °C) for 5 minutes. All films had 20 nm NaF evaporated prior to selenization. Zero-distance indicate the CIGSSe-Mo interface.
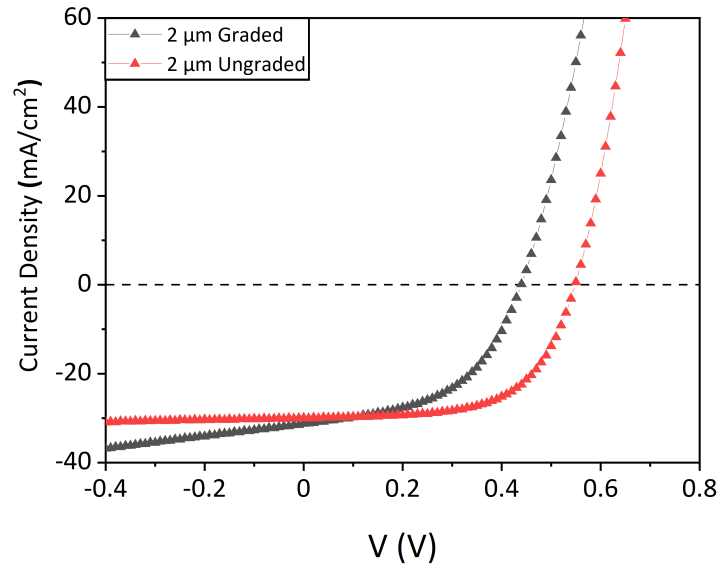
Figure 7.15. Illuminated current-voltage plots of CIGSSe devices fabricated from a 2 μm Ga-graded CIGSSe film and a 2 μm ungraded CIGSSe film. Both films were selenized using the same manner.
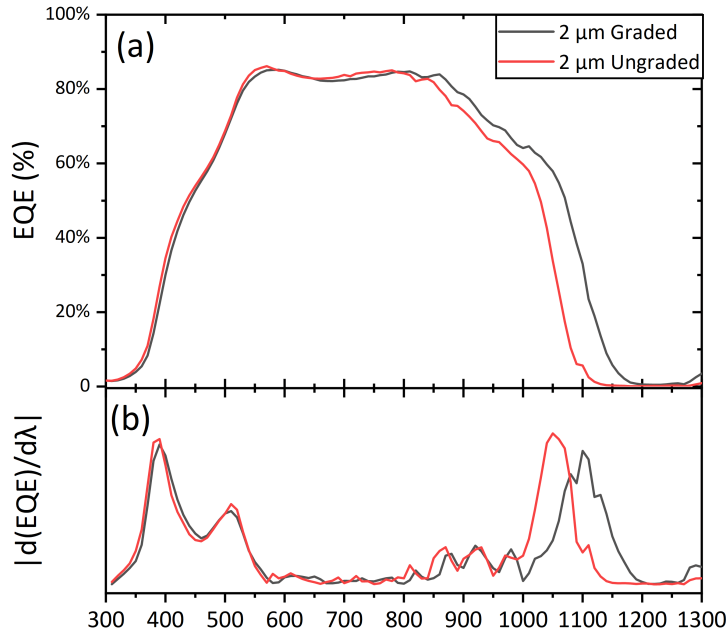
Figure 7.16. (a) EQE vs. wavelength plots of CIGSSe devices fabricated from a 2 μm Ga-graded CIGSSe film and a 2 μm ungraded CIGSSe film. (b) $|d(EQE)/d\lambda|$ vs. wavelength for the films shown in (a).

8. SUMMARY AND FUTURE RESEARCH

8.1 Summary of Key Results

In this dissertation, effects of different alkali treatments on nanoparticle-based solution-processed $Cu(In, Ga)(S, Se)_2$ films and devices were presented. These treatments have led to improvements in both the film morphology and in the optoelectronic performance of solution-processed nanoparticle-based CIGSSe films and devices. Starting with potassium, it was found that the treatment of the CIGS nanoparticle film prior to selenization has led to considerable improvements in the performance of CIGSSe devices fabricated from the K-treated films. These improvements are explained through enhanced grain growth, enhanced film bulk properties, and presence of a K-In-Se phase on the surface. Furthermore, a potassium post-deposition (selenization) was found to be a necessary condition for Cu and Ga surface depletion. Cu depletion represents one of the benefits gained from potassium treatments in vacuum-based CIGSe absorbers in that it increases the tolerance for thinning the CdS n-type layer [12].

Moving on onto the low-carbon sulfide-capped $Cu(In, Ga)S_2$ nanoparticles, growth stagnation and limited surface nucleation was observed when sintering and growing sulfide-capped CIGS nanoparticle films. It was found that the addition of alkali treatments into the system enhances the growth considerably, with dense coarsened CIGSe films with a cross-sectional morphology characterized by single grains that span the thickness of the film are obtained. Rubidium treatments on sulfide-capped CIGS nanoparticle were also investigated. It was observed that Rb, like Na, does show growth assisting behavior. Moreover, enhanced film quality and bulk properties as a result of rubidium treatments were also observed.

The results shown in the previous section offer insights into the growth of nanoparticle-based CIGSSe films, and the effects of different alkalies on the growth and properties of the CIGSSe absorber film. Knowing how the absorber film will grow and develop from a precursor nanoparticle film into a fully coarsened selenide CIGSe (CIGSSe) film under various conditions, especially in the presence of externally-added alkali, is needed to enhance the performance of nanoparticle-based CIGSSe.

8.2 Suggested Future Research

8.2.1 Heavy Alkali Post-Deposition Treatments

In Chapter 3, Cu and Ga surface depletion were found to require post-selenization treatments. Reducing the thickness of the CdS buffer layer for CIGSe films with a Cu depleted surface represents one of the benefits of heavy alkali treatments on CIGSSe devices. However, application of heavy alkali PDT onto solution-processed CIGSSe films remains challenging in that the selenized CIGSSe film needs to be transferred from the annealing furnace to the apparatus with which the alkali treatment is applied and back. This transfer will potentially increase the probability of film oxidation as the selenized film is exposed to ambient air. One approach to remove the potential oxide from the film surface is to anneal the film after the heavy alkali PDT in a reducing atmosphere, e.g. H_2 or H_2S.

The use of alkali PDT may also be combined with the surface sulfurization of the CIGSSe film. Surface sulfurization of CIGSSe films has been used extensively, most notably by Solar Frontier in their 23.35% CIGSSe world record [21]. Surface sulfurization is one of the methods to apply a front bandgap grading. Sulfurizing the CIGSe film surface increases the bandgap in the near-surface region of the CIGSSe film aiding in the passivation of the CIGSSe/CdS interface. A proposed process combining heavy alkali PDT and surface sulfurization is shown on Figure 8.1. A fully coarsened CIGSSe film is subjected to a heavy alkali (K, Rb, Cs) post-selenization treatment either through evaporation or through a solution-based approach. After the PDT, the film is annealed in a hydrogen sulfide atmosphere to reduce and sulfurize the surface forming a high-bandgap S-rich layer at the top of the film.

8.2.2 Selenide-Based Precursors

In most of the solution-processed CIGSSe literature, the selenide film is grown from sulfide-based precursor films. This film structure induces top-down growth in that the growth will start at the free surface at the top of the film and continue downwards towards the bottom of the film [55]. Inhibiting top-down growth and relying on a growth regime through bulk film coarsening, i.e. grains will grow from the film bulk in all directions, will potentially lead to CIGSe films with flatter surfaces. Flatter film surface improving the interface with the

n-type layer and subsequent window layer. Furthermore, CIGSSe films with flatter surfaces will enable their use in a tandem solar cell structure, e.g. CI(G)Se/perovskite tandem. One of the highest efficiency solution-processed CIGSSe films, fabricated from a hydrazine-based ink, is grown via a bulk-coarsening regime [46].

The current hypothesis is that enabling bulk film growth requires removing sulfur from the system and staring from a pure selenide precursor film. This would enable the film to sinter and bulk coarsen, rather than breakdown and reconstitute as selenide CIGSSe, as what is occurring during the selenization and growth of sulfide-based precursor films [55], [115], [132]. Pure selenide CIGSe films may either be ligand-exchanged $Cu(In, Ga)Se_2$ nanoparticle films, or precursor films coated from a selenide-based molecular precursor ink.

Another approach is to mimic the successful vacuum-based three stage process using a solution-based route. A three stage-coating/annealing process may be devised. a molecular precursor ink of In, Ga and Se is deposited onto a Mo-coated substrate, followed by annealing the film in a Se atmosphere at (300 - 350 °C) forming a film of $(In, Ga)_2Se_3$. After which, a second layer of a Cu-Se-based ink is coated onto the $(In, Ga)_2Se_3$ film and then annealed in excess Se atmosphere at temperatures of 550-600 °C, forming a Cu-rich CIGSe film. Finally, the third stage consists of a coating/annealing stage of an In, Ga and Se ink at 550-600 °C, forming the final Cu-poor CIGSe film.
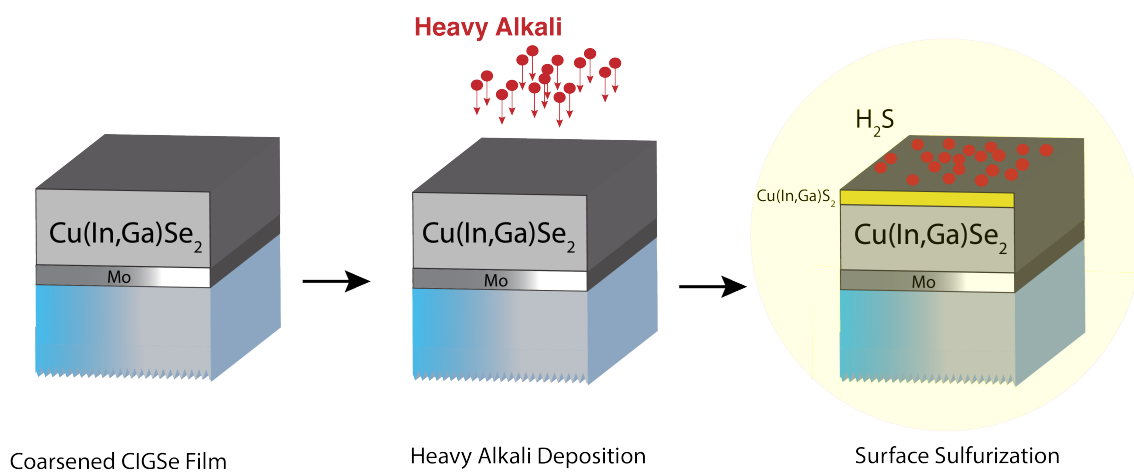
Figure 8.1. Diagram of proposed process of heavy alkali (K, Rb, Cs) PDT and subsequent surface sulfurization.

REFERENCES

[1] U.S. Energy Information Administration (EIA), "Annual Energy Outlook 2020," Tech. Rep., 2020.

[2] U.S. Energy Information Administration (EIA), "International Energy Outlook 2020 (IEO2020)," Tech. Rep., 2020.

[3] C. A. Wolden, J. Kurtin, J. B. Baxter, I. Repins, S. E. Shaheen, J. T. Torvik, A. A. Rockett, V. M. Fthenakis, and E. S. Aydil, "Photovoltaic manufacturing: Present status, future prospects, and research needs," *Journal of Vacuum Science & Technology A: Vacuum, Surfaces, and Films*, vol. 29, no. 3, p. 030 801, 2011. DOI: `10.1116/1.3569757`.

[4] J. Nelson, *The Physics of Solar Cells*. London, UK: Imperial College Press, 2003, ISBN: 1860943497.

[5] P. Würfel and U. Würfel, *Physics of solar cells : From Basic Principles to Advanced Concepts*, 2nd. Weinheim, Germany: Wiley-VCH, 2009, ISBN: 3527408576.

[6] A. Smets, K. Jäger, O. Isabella, R. van Swaaij, and M. Zeman, *Solar Energy: The Physics and Engineering of Photovoltaic Conversion, Technologies and Systems*. UIT Cambridge, 2016, ISBN: 9781906860325.

[7] S. S. Hegedus and W. N. Shafarman, "Thin-film solar cells: Device measurements and analysis," *Progress in Photovoltaics: Research and Applications*, vol. 12, no. 2-3, pp. 155–176, 2004. DOI: `10.1002/pip.518`.

[8] M. A. Green, E. D. Dunlop, D. H. Levi, J. Hohl-Ebinger, M. Yoshita, and A. W. Ho-Baillie, "Solar cell efficiency tables (version 54)," *Progress in Photovoltaics: Research and Applications*, vol. 27, no. 7, pp. 565–575, 2019. DOI: `10.1002/pip.3171`.

[9] T. D. Lee and A. U. Ebong, "A review of thin film solar cell technologies and challenges," *Renewable and Sustainable Energy Reviews*, vol. 70, no. November 2016, pp. 1286–1297, 2017. DOI: `10.1016/j.rser.2016.12.028`.

[10] A. Chirilă, S. Buecheler, F. Pianezzi, P. Bloesch, C. Gretener, A. R. Uhl, C. Fella, L. Kranz, J. Perrenoud, S. Seyrling, R. Verma, S. Nishiwaki, Y. E. Romanyuk, G. Bilger, and A. N. Tiwari, "Highly efficient Cu(In, Ga)Se$_2$ solar cells grown on flexible polymer films," *Nature Materials*, vol. 10, no. 11, pp. 857–861, 2011. DOI: `10.1038/nmat3122`.

[11]   D. Hariskos and M. Powalla, "Thermodynamic limitations for alkali metals in Cu(In,Ga)Se$_2$," *Journal of Materials Research*, vol. 32, no. 20, pp. 3789–3800, 2017. DOI: 10.1557/jmr.2017.394.

[12]   A. Chirilă, P. Reinhard, F. Pianezzi, P. Bloesch, A. R. Uhl, C. Fella, L. Kranz, D. Keller, C. Gretener, H. Hagendorfer, D. Jaeger, R. Erni, S. Nishiwaki, S. Buecheler, and A. N. Tiwari, "Potassium-induced surface modification of Cu(In, Ga)Se$_2$ thin films for high-efficiency solar cells," *Nature Materials*, vol. 12, no. 12, pp. 1107–1111, 2013. DOI: 10.1038/nmat3789.

[13]   T. Feurer, B. Bissig, T. P. Weiss, R. Carron, E. Avancini, J. Löckinger, S. Buecheler, and A. N. Tiwari, "Single-graded CIGS with narrow bandgap for tandem solar cells," *Science and Technology of Advanced Materials*, vol. 19, no. 1, pp. 263–270, 2018. DOI: 10.1080/14686996.2018.1444317.

[14]   T. Feurer, R. Carron, G. Torres Sevilla, F. Fu, S. Pisoni, Y. E. Romanyuk, S. Buecheler, and A. N. Tiwari, "Efficiency Improvement of Near-Stoichiometric CuInSe$_2$ Solar Cells for Application in Tandem Devices," *Advanced Energy Materials*, vol. 9, no. 35, pp. 2–7, 2019. DOI: 10.1002/aenm.201901428.

[15]   R. G. Ellis, D. Vak, A. S. R. Chesman, and R. Agrawal, "Slot Die Coating of CIGS Nanoparticle Inks for Scalable Solution Processed Photovoltaics," in *2019 IEEE 46th Photovoltaic Specialists Conference (PVSC)*, IEEE, 2019, pp. 1830–1833. DOI: 10.1109/PVSC40753.2019.8980504.

[16]   F. Kessler and D. Rudmann, "Technological aspects of flexible CIGS solar cells and modules," *Solar Energy*, vol. 77, no. 6, pp. 685–695, 2004. DOI: 10.1016/j.solener.2004.04.010.

[17]   P. Jackson, R. Würz, U. Rau, J. Mattheis, M. Kurth, T. Schlötzer, G. Bilger, and J. H. Werner, "High quality baseline for high efficiency Cu(In$_{1-x}$, Ga$_x$)Se$_2$ solar cells," *Progress in Photovoltaics: Research and Applications*, vol. 15, no. 6, pp. 507–519, 2007. DOI: 10.1002/pip.757.

[18]   D. Rudmann, "Effects of sodium on growth and properties of Cu(In, Ga)Se$_2$ thin films and solar cells," Ph.D. Dissertation, Eidgenössische Technische Hochschule ETH Zürich, 2004. DOI: 10.3929/ethz-a-004796411.

[19]   U. Rau and H.-W. Schock, "Cu(In,Ga)Se$_2$ Thin-Film Solar Cells," in *McEvoy's Handbook of Photovoltaics*, Elsevier, 2018, pp. 371–418. DOI: 10.1016/B978-0-12-809921-6.00010-0.

[20]   O. Lundberg, M. Edoff, and L. Stolt, "The effect of Ga-grading in CIGS thin film solar cells," *Thin Solid Films*, vol. 480-481, pp. 520–525, 2005. DOI: 10.1016/j.tsf.2004.11.080.

[21] M. Nakamura, K. Yamaguchi, Y. Kimoto, Y. Yasaki, T. Kato, and H. Sugimoto, "Cd-Free $Cu(In, Ga)(Se, S)_2$ Thin-Film Solar Cell With Record Efficiency of 23.35%," *IEEE Journal of Photovoltaics*, vol. 9, no. 6, pp. 1863–1867, 2019. DOI: `10.1109/JPHOTOV.2019.2937218`.

[22] T. Kato, "$Cu(In,Ga)Se_2$ solar cell research in Solar Frontier: Progress and current status," *Japanese Journal of Applied Physics*, vol. 56, no. 4S, 04CA02, 2017. DOI: `10.7567/JJAP.56.04CA02`.

[23] J. K. Larsen, J. Keller, O. Lundberg, T. Jarmar, L. Riekehr, J. J. S. Scragg, and C. Platzer-Bjorkman, "Sulfurization of Co-Evaporated $Cu(In, Ga)Se_2$ as a Postdeposition Treatment," *IEEE Journal of Photovoltaics*, vol. 8, no. 2, pp. 604–610, 2018. DOI: `10.1109/JPHOTOV.2018.2793759`.

[24] J. Ramanujam and U. P. Singh, "Copper indium gallium selenide based solar cells – a review," *Energy & Environmental Science*, vol. 10, no. 6, pp. 1306–1319, 2017. DOI: `10.1039/C7EE00826K`.

[25] M. A. Contreras, M. J. Romero, B. To, F. Hasoon, R. Noufi, S. Ward, and K. Ramanathan, "Optimization of CBD CdS process in high-efficiency $Cu(In, Ga)Se_2$-based solar cells," *Thin Solid Films*, vol. 403-404, pp. 204–211, 2002. DOI: `10.1016/S0040-6090(01)01538-3`.

[26] T. Lepetit, S. Harel, L. Arzel, G. Ouvrard, and N. Barreau, "Coevaporated $KInSe_2$: A Fast Alternative to KF Postdeposition Treatment in High-Efficiency $Cu(In, Ga)Se_2$ Thin Film Solar Cells," *IEEE Journal of Photovoltaics*, vol. 6, no. 5, pp. 1316–1320, 2016. DOI: `10.1109/JPHOTOV.2016.2589365`.

[27] J. Chantana, T. Kato, H. Sugimoto, and T. Minemoto, "Structures of $Cu(In, Ga)(S, Se)_2$ solar cells for minimizing open-circuit voltage deficit: Investigation of carrier recombination rates," *Progress in Photovoltaics: Research and Applications*, no. June 2018, pip.3137, 2019. DOI: `10.1002/pip.3137`.

[28] K. F. Tai, R. Kamada, T. Yagioka, T. Kato, and H. Sugimoto, "From 20.9 to 22.3% $Cu(In, Ga)(S, Se)_2$ solar cell: Reduced recombination rate at the heterojunction and the depletion region due to K-treatment," *Japanese Journal of Applied Physics*, vol. 56, no. 8S2, p. 08MC03, 2017. DOI: `10.7567/JJAP.56.08MC03`.

[29] J. Chantana, T. Kato, H. Sugimoto, and T. Minemoto, "Investigation of correlation between open-circuit voltage deficit and carrier recombination rates in $Cu(In, Ga)(S, Se)_2$ -based thin-film solar cells," *Applied Physics Letters*, vol. 112, no. 15, p. 151 601, 2018. DOI: `10.1063/1.5023828`.

[30] J. Chantana, Y. Kawano, T. Nishimura, Y. Kimoto, T. Kato, H. Sugimoto, and T. Minemoto, "Effect of Alkali Treatment on Photovoltaic Performances of $Cu(In, Ga)(S, Se)_2$ Solar Cells and Their Absorber Quality Analyzed by Urbach Energy and Carrier Recombination Rates," *ACS Applied Energy Materials*, vol. 3, no. 2, pp. 1292–1297, 2020. DOI: `10.1021/acsaem.9b02293`.

[31] T. Kato, A. Handa, T. Yagioka, T. Matsuura, K. Yamamoto, S. Higashi, J.-L. Wu, K. F. Tai, H. Hiroi, T. Yoshiyama, T. Sakai, and H. Sugimoto, "Enhanced Efficiency of Cd-Free $Cu(In, Ga)(Se, S)_2$ Minimodule Via (Zn,Mg)O Second Buffer Layer and Alkali Metal Post-Treatment," *IEEE Journal of Photovoltaics*, vol. 7, no. 6, pp. 1773–1780, 2017. DOI: `10.1109/JPHOTOV.2017.2745710`.

[32] J. Chantana, T. Kato, H. Sugimoto, and T. Minemoto, "20%-Efficient $Zn_{0.9}Mg_{0.1}O$:Al/$Zn_{0.8}Mg_{0.2}$ $Cu(In, Ga)(S, Se)_2$ Solar Cell Prepared by All Dry Process through Combination of Heat-Light Soaking and Light Soaking Process," *ACS Applied Materials & Interfaces*, acsami.8b01247, 2018. DOI: `10.1021/acsami.8b01247`.

[33] R. Noufi, A. M. Gabor, J. R. Tuttle, A. L. Tennant, M. A. Contreras, D. S. Albin, and J. J. Carapella, *Method of fabricating high-efficiency Cu(In, Ga)(Se, S)₂ thin films for solar cells. U.S. Patent 5,441,897*, 1995.

[34] K. Ramanathan, M. A. Contreras, C. L. Perkins, S. Asher, F. S. Hasoon, J. Keane, D. Young, M. Romero, W. Metzger, R. Noufi, J. Ward, and A. Duda, "Properties of 19.2% efficiency $ZnO/CdS/CuInGaSe_2$ thin-film solar cells," *Progress in Photovoltaics: Research and Applications*, vol. 11, no. 4, pp. 225–230, 2003. DOI: `10.1002/pip.494`.

[35] I. Repins, M. A. Contreras, B. Egaas, C. DeHart, J. Scharf, C. L. Perkins, B. To, and R. Noufi, "19 · 9%-efficient $ZnO/CdS/CuInGaSe_2$ solar cell with 81.2% fill factor," *Progress in Photovoltaics: Research and Applications*, vol. 16, no. 3, pp. 235–239, 2008. DOI: `10.1002/pip.822`.

[36] W. K. Kim, E. A. Payzant, S. Yoon, and T. J. Anderson, "In situ investigation on selenization kinetics of Cu-In precursor using time-resolved, high temperature X-ray diffraction," *Journal of Crystal Growth*, vol. 294, no. 2, pp. 231–235, 2006. DOI: `10.1016/j.jcrysgro.2006.05.066`.

[37] M. M. Islam, A. Uedono, T. Sakurai, A. Yamada, S. Ishizuka, K. Matsubara, S. Niki, and K. Akimoto, "Impact of Se flux on the defect formation in polycrystalline $Cu(In, Ga)Se_2$ thin films grown by three stage evaporation process," *Journal of Applied Physics*, vol. 113, no. 6, 2013. DOI: `10.1063/1.4792049`.

[38] G. Hanna, J. Mattheis, V. Laptev, Y. Yamamoto, U. Rau, and H. W. Schock, "Influence of the selenium flux on the growth of $Cu(In, Ga)Se_2$ thin films," *Thin Solid Films*, vol. 431-432, no. 03, pp. 31–36, 2003. DOI: `10.1016/S0040-6090(03)00242-6`.

[39] J. H. Yun, K. H. Kim, B. T. Ahn, and K. H. Yoon, "Effect of Se beam flux rate on photovoltaic properties of CIGS cells fabricated by three-stage co-evaporation process," *Physica Status Solidi (C) Current Topics in Solid State Physics*, vol. 3, no. 8, pp. 2547–2550, 2006. DOI: `10.1002/pssc.200669611`.

[40] R. Caballero, C. A. Kaufmann, V. Efimova, T. Rissom, V. Hoffmann, and H. W. Schock, "Investigation of $Cu(In, Ga)Se_2$ thin-film formation during the multi-stage co-evaporation process," *Progress in Photovoltaics: Research and Applications*, vol. 21, no. 1, pp. 30–46, 2013. DOI: `10.1002/pip.1233`.

[41] J. Hedstrom, H. Ohlsen, M. Bodegard, A. Kylner, L. Stolt, D. Hariskos, M. Ruckh, and H.-W. Schock, "$ZnO/CdS/Cu(In, Ga)Se_2$ thin film solar cells with improved performance," in *Conference Record of the Twenty Third IEEE Photovoltaic Specialists Conference - 1993 (Cat. No.93CH3283-9)*, IEEE, 1993, pp. 364–371. DOI: `10.1109/PVSC.1993.347154`.

[42] T. Kato, J.-L. Wu, Y. Hirai, H. Sugimoto, and V. Bermudez, "Record Efficiency for Thin-Film Polycrystalline Solar Cells Up to 22.9% Achieved by Cs-Treated $Cu(In, Ga)(Se, S)_2$," *IEEE Journal of Photovoltaics*, vol. 9, no. 1, pp. 325–330, 2019. DOI: `10.1109/JPHOTOV.2018.2882206`.

[43] W. Li, X. Yan, A. G. Aberle, and S. Venkataraj, "Effect of sodium diffusion on the properties of CIGS solar absorbers prepared using elemental Se in a two-step process," *Scientific Reports*, vol. 9, no. 1, p. 2637, 2019. DOI: `10.1038/s41598-019-39283-2`.

[44] C. J. Hibberd, E. Chassaing, W. Liu, D. B. Mitzi, D. Lincot, and A. N. Tiwari, "Non-vacuum methods for formation of $Cu(In, Ga)(Se\,S)_2$ thin film photovoltaic absorbers," *Progress in Photovoltaics: Research and Applications*, vol. 18, no. 6, pp. 434–452, 2010. DOI: `10.1002/pip.914`.

[45] A. Nakamura, H. Iida, T. Ohashi, Y. Kikuchi, Y.-C. Liao, Y. Kawaguchi, and T. Aramoto, "High Efficiency Solution Coated $Cu(In, Ga)(Se, S)_2$ Thin Film Solar Cells," *32nd European Photovoltaic Solar Energy Conference and Exhibition*, pp. 1108–1111, 2016. DOI: `10.4229/EUPVSEC20162016-3BO.8.3`.

[46] T. Zhang, Y. Yang, D. Liu, S. C. Tse, W. Cao, Z. Feng, S. Chen, and L. Qian, "High efficiency solution-processed thin-film $Cu(In, Ga)(Se, S)_2$ solar cells," *Energy Environ. Sci.*, vol. 9, no. 12, pp. 3674–3681, 2016. DOI: `10.1039/C6EE02352E`.

[47] S. M. McLeod, C. J. Hages, N. J. Carter, and R. Agrawal, "Synthesis and characterization of 15% efficient CIGSSe solar cells from nanoparticle inks," *Progress in Photovoltaics: Research and Applications*, vol. 23, no. 11, pp. 1550–1556, 2015. DOI: `10.1002/pip.2588`.

[48] G. M. Ford, Q. Guo, R. Agrawal, and H. W. Hillhouse, "Cu(In,Ga)(S,Se)$_2$ thin film solar cells from nanocrystal inks: Effect of nanocrystal precursors," *Thin Solid Films*, vol. 520, no. 1, pp. 523–528, 2011. DOI: `10.1016/j.tsf.2011.08.007`.

[49] G. M. Ford, Q. Guo, R. Agrawal, and H. W. Hillhouse, "Earth Abundant Element Cu$_2$Zn(Sn$_{1-x}$Ge$_x$)S$_4$ NanocrystalsforTunable Band Gap Solar Cells: 6.8% Efficient Device Fabrication," *Chemistry of Materials*, vol. 23, no. 10, pp. 8–11, 2011. DOI: `10.1021/cm2002836`.

[50] Q. Guo, G. M. Ford, W. C. Yang, B. C. Walker, E. a. Stach, H. W. Hillhouse, and R. Agrawal, "Fabrication of 7.2% efficient CZTSSe solar cells using CZTS nanocrystals," *Journal of the American Chemical Society*, vol. 132, no. 49, pp. 17 384–17 386, 2010. DOI: `10.1021/ja108427b`.

[51] C. K. Miskin, W.-C. Yang, C. J. Hages, N. J. Carter, C. S. Joglekar, E. A. Stach, and R. Agrawal, "9.0% efficient Cu$_2$ZnSn(S, Se)$_4$ solar cells from selenized nanoparticle inks," *Progress in Photovoltaics: Research and Applications*, vol. 23, no. 5, pp. 654–659, 2015. DOI: `10.1002/pip.2472`.

[52] C. J. Hages, S. Levcenco, C. K. Miskin, J. H. Alsmeier, D. Abou-Ras, R. G. Wilks, M. Bär, T. Unold, and R. Agrawal, "Improved performance of Ge-alloyed CZTGeSSe thin-film solar cells through control of elemental losses," *Progress in Photovoltaics: Research and Applications*, vol. 23, no. 3, pp. 376–384, 2015. DOI: `10.1002/pip.2442`.

[53] C. J. Hages, M. J. Koeper, and R. Agrawal, "Optoelectronic and material properties of nanocrystal-based CZTSe absorbers with Ag-alloying," *Solar Energy Materials and Solar Cells*, vol. 145, pp. 342–348, 2016. DOI: `10.1016/j.solmat.2015.10.039`.

[54] Q. Guo, G. M. Ford, R. Agrawal, and H. W. Hillhouse, "Ink formulation and low-temperature incorporation of sodium to yield 12% efficient Cu(In, Ga)(S, Se)$_2$ solar cells from sulfide nanocrystal inks," *Progress in Photovoltaics: Research and Applications*, vol. 21, no. 1, pp. 64–71, 2013. DOI: `10.1002/pip.2200`.

[55] S. McLeod, E. Alruqobah, and R. Agrawal, "Liquid assisted grain growth in solution processed Cu(In, Ga)(S, Se)$_2$," *Solar Energy Materials and Solar Cells*, vol. 195, no. February, pp. 12–23, 2019. DOI: `10.1016/j.solmat.2019.02.020`.

[56] E. H. Alruqobah and R. Agrawal, "Potassium Treatments for Solution-Processed Cu(In, Ga)(S, Se)$_2$ Solar Cells," *ACS Applied Energy Materials*, vol. 3, no. 5, pp. 4821–4830, 2020. DOI: `10.1021/acsaem.0c00422`.

[57]   R. G. Ellis, J. W. Turnley, D. J. Rokke, J. P. Fields, E. H. Alruqobah, S. D. Deshmukh, K. Kisslinger, and R. Agrawal, "Hybrid Ligand Exchange of $Cu(In, Ga)S_2$ Nanoparticles for Carbon Impurity Removal in Solution-Processed Photovoltaics," *Chemistry of Materials*, vol. 32, no. 12, pp. 5091–5103, 2020. DOI: `10.1021/acs.chemmater.0c00966`.

[58]   S. A. McClary, J. Andler, C. A. Handwerker, and R. Agrawal, "Solution-processed copper arsenic sulfide thin films for photovoltaic applications," *J. Mater. Chem. C*, vol. 5, no. 28, pp. 6913–6916, 2017. DOI: `10.1039/C7TC01920C`.

[59]   S. A. McClary, R. B. Balow, and R. Agrawal, "Role of annealing atmosphere on the crystal structure and composition of tetrahedrite–tennantite alloy nanoparticles," *Journal of Materials Chemistry C*, 2018. DOI: `10.1039/C8TC02762E`.

[60]   X. Hu, S. Pritchett-Montavon, C. Handwerker, and R. Agrawal, "Reaction pathways and optoelectronic characterization of single-phase Ag_2ZnSnS_4 nanoparticles," *Journal of Materials Research*, vol. 34, no. 22, pp. 3810–3818, 2019. DOI: `10.1557/jmr.2019.328`.

[61]   M. A. Boles, D. Ling, T. Hyeon, and D. V. Talapin, "The surface science of nanocrystals," *Nature Materials*, vol. 15, no. 2, pp. 141–153, 2016. DOI: `10.1038/nmat4526`.

[62]   J. Tang, S. Hinds, S. O. Kelley, and E. H. Sargent, "Synthesis of Colloidal $CuGaSe_2$, $CuInSe_2$, and $Cu(In, Ga)Se_2$ Nanoparticles," *Chemistry of Materials*, vol. 20, no. 22, pp. 6906–6910, 2008. DOI: `10.1021/cm801655w`.

[63]   S. D. Deshmukh, R. G. Ellis, D. S. Sutandar, D. J. Rokke, and R. Agrawal, "Versatile Colloidal Syntheses of Metal Chalcogenide Nanoparticles from Elemental Precursors Using Amine-Thiol Chemistry," *Chemistry of Materials*, vol. 31, no. 21, pp. 9087–9097, 2019. DOI: `10.1021/acs.chemmater.9b03401`.

[64]   U. Berner, D. Colombara, J. de Wild, E. V. Robert, M. Schütze, F. Hergert, N. Valle, M. Widenmeyer, and P. J. Dale, "13.3% efficient solution deposited $Cu(In, Ga)Se_2$ solar cells processed with different sodium salt sources," *Progress in Photovoltaics: Research and Applications*, vol. 24, no. 6, pp. 749–759, 2016. DOI: `10.1002/pip.2721`.

[65]   A. R. Uhl, A. Rajagopal, J. A. Clark, A. Murray, T. Feurer, S. Buecheler, A. K.-Y. Jen, and H. W. Hillhouse, "Solution-Processed Low-Bandgap $CuIn(S, Se)_2$ Absorbers for High-Efficiency Single-Junction and Monolithic Chalcopyrite-Perovskite Tandem Solar Cells," *Advanced Energy Materials*, vol. 8, no. 27, p. 1 801 254, 2018. DOI: `10.1002/aenm.201801254`.

[66] X. Zhao, M. Lu, M. J. Koeper, and R. Agrawal, "Solution-processed sulfur depleted $Cu(In, Ga)Se_2$ solar cells synthesized from a monoamine–dithiol solvent mixture," *Journal of Materials Chemistry A*, vol. 4, no. 19, pp. 7390–7397, 2016. DOI: `10.1039/C6TA00533K`.

[67] X. Zhao, S. D. Deshmukh, D. J. Rokke, G. Zhang, Z. Wu, J. T. Miller, and R. Agrawal, "Investigating Chemistry of Metal Dissolution in Amine–Thiol Mixtures and Exploiting It toward Benign Ink Formulation for Metal Chalcogenide Thin Films," *Chemistry of Materials*, vol. 31, no. 15, pp. 5674–5682, 2019. DOI: `10.1021/acs.chemmater.9b01566`.

[68] D. Zhao, Q. Fan, Q. Tian, Z. Zhou, Y. Meng, D. Kou, W. Zhou, and S. Wu, "Eliminating fine-grained layers in $Cu(In, Ga)(S, Se)_2$ thin films for solution-processed high efficiency solar cells," *Journal of Materials Chemistry A*, vol. 4, no. 35, pp. 13 476–13 481, 2016. DOI: `10.1039/C6TA05728D`.

[69] S. Yuan, X. Wang, Y. Zhao, Q. Chang, Z. Xu, J. Kong, and S. Wu, "Solution Processed $Cu(In, Ga)(S, Se)_2$ Solar Cells with 15.25% Efficiency by Surface Sulfurization," *ACS Applied Energy Materials*, vol. 3, no. 7, pp. 6785–6792, 2020. DOI: `10.1021/acsaem.0c00917`.

[70] D. Rudmann, A. F. Da Cunha, M. Kaelin, F. Kurdesau, H. Zogg, A. N. Tiwari, and G. Bilger, "Efficiency enhancement of $Cu(In, Ga)Se_2$ solar cells due to post-deposition Na incorporation," *Applied Physics Letters*, vol. 84, no. 7, pp. 1129–1131, 2004. DOI: `10.1063/1.1646758`.

[71] D. Rudmann, D. Brémaud, A. F. Da Cunha, G. Bilger, A. Strohm, M. Kaelin, H. Zogg, and A. N. Tiwari, "Sodium incorporation strategies for CIGS growth at different temperatures," *Thin Solid Films*, vol. 480-481, pp. 55–60, 2005. DOI: `10.1016/j.tsf.2004.11.071`.

[72] D. Rudmann, A. F. Da Cunha, M. Kaelin, F. J. Haug, H. Zogg, and A. N. Tiwari, "Effects of Na on the Growth of $Cu(In, Ga)Se_2$ Thin Films and Solar Cells," *Materials Research Society Symposium - Proceedings*, vol. 763, pp. 53–66, 2003. DOI: `10.1557/proc-763-b1.9`.

[73] E. Handick, P. Reinhard, R. G. Wilks, F. Pianezzi, T. Kunze, D. Kreikemeyer-Lorenzo, L. Weinhardt, M. Blum, W. Yang, M. Gorgoi, E. Ikenaga, D. Gerlach, S. Ueda, Y. Yamashita, T. Chikyow, C. Heske, S. Buecheler, A. N. Tiwari, and M. Bär, "Formation of a K—In—Se Surface Species by NaF/KF Postdeposition Treatment of $Cu(In, Ga)Se_2$ Thin-Film Solar Cell Absorbers," *ACS Applied Materials & Interfaces*, vol. 9, no. 4, pp. 3581–3589, 2017. DOI: `10.1021/acsami.6b11892`.

[74] T. Lepetit, S. Harel, L. Arzel, G. Ouvrard, and N. Barreau, "KF post deposition treatment in co-evaporated $Cu(In, Ga)Se_2$ thin film solar cells: Beneficial or detrimental effect induced by the absorber characteristics," *Progress in Photovoltaics: Research and Applications*, vol. 25, no. 12, pp. 1068–1076, 2017. DOI: 10.1002/pip.2924.

[75] E. Avancini, R. Carron, T. P. Weiss, C. Andres, M. Bürki, C. Schreiner, R. Figi, Y. E. Romanyuk, S. Buecheler, and A. N. Tiwari, "Effects of Rubidium Fluoride and Potassium Fluoride Postdeposition Treatments on $Cu(In, Ga)Se_2$ Thin Films and Solar Cell Performance," *Chemistry of Materials*, vol. 29, no. 22, pp. 9695–9704, 2017. DOI: 10.1021/acs.chemmater.7b03412.

[76] D. Kreikemeyer-Lorenzo, D. Hauschild, P. Jackson, T. M. Friedlmeier, D. Hariskos, M. Blum, W. Yang, F. Reinert, M. Powalla, C. Heske, and L. Weinhardt, "Rubidium Fluoride Post-Deposition Treatment: Impact on the Chemical Structure of the $Cu(In, Ga)Se_2$ Surface and $CdS/Cu(In, Ga)Se_2$ Interface in Thin-Film Solar Cells," *ACS Applied Materials & Interfaces*, vol. 10, no. 43, pp. 37 602–37 608, 2018. DOI: 10.1021/acsami.8b10005.

[77] H. Lee, Y. Jang, S.-w. Nam, C. Jung, P.-p. Choi, J. Gwak, J. H. Yun, K. Kim, and B. Shin, "Passivation of Deep-Level Defects by Cesium Fluoride Post-Deposition Treatment for Improved Device Performance of $Cu(In, Ga)Se_2$ Solar Cells," *ACS Applied Materials & Interfaces*, vol. 11, no. 39, pp. 35 653–35 660, 2019. DOI: 10.1021/acsami.9b08316.

[78] K. Beppu, Y. Hirai, T. Kato, S. Ishizuka, T. Ina, and T. Wada, "Effect of cesium for $Cu(In, Ga)Se_2$ and $Cu(In, Ga)(S, Se)_2$ films studied by depth-resolved XAFS," *Applied Physics Letters*, vol. 117, no. 4, p. 043 901, 2020. DOI: 10.1063/5.0013375.

[79] M. Bodeg Ård, K. Granath, and L. Stolt, "Growth of $Cu(In, Ga)Se_2$ thin films by coevaporation using alkaline precursors," *Thin Solid Films*, vol. 361-362, pp. 9–16, 2000. DOI: 10.1016/S0040-6090(99)00828-7.

[80] M. Contreras, B. Egaas, P. Dippo, J. Webb, J. Granata, K. Ramanathan, S. Asher, A. Swartzlander, and R. Noufi, "On the role of Na and modifications to $Cu(In, Ga)Se_2$ absorber materials using thin-MF (M=Na, K, Cs) precursor layers [solar cells]," in *Conference Record of the Twenty Sixth IEEE Photovoltaic Specialists Conference - 1997*, vol. 96, IEEE, 1997, pp. 359–362. DOI: 10.1109/PVSC.1997.654102.

[81] S. Siebentritt, E. Avancini, M. Bär, J. Bombsch, E. Bourgeois, S. Buecheler, R. Carron, C. Castro, S. Duguay, R. Félix, E. Handick, D. Hariskos, V. Havu, P. Jackson, H.-p. Komsa, T. Kunze, M. Malitckaya, R. Menozzi, M. Nesladek, N. Nicoara, M. Puska, M. Raghuwanshi, P. Pareige, S. Sadewasser, G. Sozzi, A. N. Tiwari, S. Ueda, A. Vilalta-Clemente, T. P. Weiss, F. Werner, R. G. Wilks, W. Witte, and M. H. Wolter, "Heavy Alkali Treatment of $Cu(In, Ga)Se_2$ Solar Cells: Surface versus Bulk Effects," *Advanced Energy Materials*, vol. 10, no. 8, p. 1 903 752, 2020. DOI: 10.1002/aenm.201903752.

[82] D. Braunger, D. Hariskos, G. Bilger, U. Rau, and H. W. Schock, "Influence of sodium on the growth of polycrystalline $Cu(In, Ga)Se_2$ thin films," *Thin Solid Films*, vol. 361, pp. 161–166, 2000. DOI: `10.1016/S0040-6090(99)00777-4`.

[83] L. Kronik, D. Cahen, and H. W. Schock, "Effects of Sodium on Polycrystalline $Cu(In, Ga)Se_2$ and Its Solar Cell Performance," *Advanced Materials*, vol. 10, no. 1, pp. 31–36, 1998. DOI: `10.1002/(SICI)1521-4095(199801)10:1<31::AID-ADMA31>3.0.CO;2-3`.

[84] D. W. Niles, K. Ramanathan, J. Granata, F. Hasoon, R. Noufi, B. J. Tielsch, and J. E. Fulghum, "Na Impurity Chemistry in Photovoltaic CIGS thin-Films: An Investigation with Photo and Auger Electron Spectroscopies," *MRS Proceedings*, vol. 485, p. 179, 1997. DOI: `10.1557/PROC-485-179`.

[85] B. Stanbery, S. Kincal, S. Kim, T. Anderson, O. Crisalle, S. Ahrenkiel, and G. Lippold, "Role of sodium in the control of defect structures in CIS [solar cells]," in *Conference Record of the Twenty-Eighth IEEE Photovoltaic Specialists Conference - 2000 (Cat. No.00CH37036)*, vol. 2000, IEEE, 2000, pp. 440–445, ISBN: 0-7803-5772-8. DOI: `10.1109/PVSC.2000.915864`.

[86] D. W. Niles, M. Al-Jassim, and K. Ramanathan, "Direct observation of Na and O impurities at grain surfaces of $CuInSe_2$ thin films," *Journal of Vacuum Science & Technology A: Vacuum, Surfaces, and Films*, vol. 17, no. 1, pp. 291–296, 1999. DOI: `10.1116/1.581583`.

[87] D. Abou-Ras, A. Nikolaeva, S. Caicedo Dávila, M. Krause, H. Guthrey, M. Al-Jassim, M. Morawski, and R. Scheer, "No Evidence for Passivation Effects of Na and K at Grain Boundaries in Polycrystalline $Cu(In, Ga)Se_2$ Thin Films for Solar Cells," *Solar RRL*, vol. 1900095, p. 1 900 095, 2019. DOI: `10.1002/solr.201900095`.

[88] M. Ohring, *Materials science of thin films: deposition and structure*. Academic Press, 2002, ISBN: 0080491782.

[89] T. Nakada, D. Iga, H. Ohbo, and A. Kunioka, "Effects of Sodium on $Cu(In, Ga)Se_2$-Based Thin Films and Solar Cells," *Japanese Journal of Applied Physics*, vol. 36, no. Part 1, No. 2, pp. 732–737, 1997. DOI: `10.1143/JJAP.36.732`.

[90] D. Abou-Ras, S. S. Schmidt, R. Caballero, T. Unold, H. W. Schock, C. T. Koch, B. Schaffer, M. Schaffer, P. P. Choi, and O. Cojocaru-Miredin, "Confined and chemically flexible grain boundaries in polycrystalline compound semiconductors," *Advanced Energy Materials*, vol. 2, no. 8, pp. 992–998, 2012. DOI: `10.1002/aenm.201100764`.

[91] E. Cadel, N. Barreau, J. Kessler, and P. Pareige, "Atom probe study of sodium distribution in polycrystalline $Cu(In, Ga)Se_2$ thin film," *Acta Materialia*, vol. 58, no. 7, pp. 2634–2637, 2010. DOI: `10.1016/j.actamat.2009.12.049`.

[92] E. Handick, P. Reinhard, J.-H. Alsmeier, L. Köhler, F. Pianezzi, S. Krause, M. Gorgoi, E. Ikenaga, N. Koch, R. G. Wilks, S. Buecheler, A. N. Tiwari, and M. Bär, "Potassium Postdeposition Treatment-Induced Band Gap Widening at Cu(In, Ga)Se$_2$ Surfaces – Reason for Performance Leap?" *ACS Applied Materials & Interfaces*, vol. 7, no. 49, pp. 27 414–27 420, 2015. DOI: `10.1021/acsami.5b09231`.

[93] P. Pistor, D. Greiner, C. A. Kaufmann, S. Brunken, M. Gorgoi, A. Steigert, W. Calvet, I. Lauermann, R. Klenk, T. Unold, and M. C. Lux-Steiner, "Experimental indication for band gap widening of chalcopyrite solar cell absorbers after potassium fluoride treatment," *Applied Physics Letters*, vol. 105, no. 6, 2014. DOI: `10.1063/1.4892882`.

[94] M. Malitckaya, H.-P. Komsa, V. Havu, and M. J. Puska, "Effect of Alkali Metal Atom Doping on the CuInSe$_2$-Based Solar Cell Absorber," *The Journal of Physical Chemistry C*, vol. 121, no. 29, pp. 15 516–15 528, 2017. DOI: `10.1021/acs.jpcc.7b03083`.

[95] S. Wang, X. Hao, M. M. Islam, T. Kato, H. Sugimoto, K. Akimoto, and T. Sakurai, "Influence of potassium treatment on electronic properties of Cu(In$_{1-x}$, Ga$_x$)(Se$_{1-y}$S$_y$)$_2$ solar cells studied by steady state photo-capacitance and admittance spectroscopy," *Japanese Journal of Applied Physics*, vol. 57, no. 8S3, 08RC13, 2018. DOI: `10.7567/JJAP.57.08RC13`.

[96] M. Mezher, L. M. Mansfield, K. Horsley, W. Yang, M. Blum, L. Weinhardt, K. Ramanathan, and C. Heske, "Variations in the Chemical and Electronic Impact of Post-Deposition Treatments on Cu(In, Ga)(S, Se)$_2$ Absorbers," *ACS Applied Energy Materials*, vol. 2, no. 12, pp. 8641–8648, 2019. DOI: `10.1021/acsaem.9b01565`.

[97] M. H. Wolter, B. Bissig, E. Avancini, R. Carron, S. Buecheler, P. Jackson, and S. Siebentritt, "Influence of Sodium and Rubidium Postdeposition Treatment on the Quasi-Fermi Level Splitting of Cu(In, Ga)Se$_2$ Thin Films," *IEEE Journal of Photovoltaics*, vol. 8, no. 5, pp. 1320–1325, 2018. DOI: `10.1109/JPHOTOV.2018.2855113`.

[98] N. Maticiuc, T. Kodalle, J. Lauche, R. Wenisch, T. Bertram, C. A. Kaufmann, and I. Lauermann, "In vacuo XPS investigation of Cu(In, Ga)Se$_2$ surface after RbF post-deposition treatment," *Thin Solid Films*, vol. 665, no. July, pp. 143–147, 2018. DOI: `10.1016/j.tsf.2018.09.026`.

[99] P. Schöppe, S. Schönherr, R. Wuerz, W. Wisniewski, G. Martínez-Criado, M. Ritzer, K. Ritter, C. Ronning, and C. S. Schnohr, "Rubidium segregation at random grain boundaries in Cu(In, Ga)Se$_2$ absorbers," *Nano Energy*, vol. 42, no. August, pp. 307–313, 2017. DOI: `10.1016/j.nanoen.2017.10.063`.

[100] P. Schöppe, S. Schönherr, P. Jackson, R. Wuerz, W. Wisniewski, M. Ritzer, M. Zapf, A. Johannes, C. S. Schnohr, and C. Ronning, "Overall Distribution of Rubidium in Highly Efficient Cu(In, Ga)Se$_2$ Solar Cells," *ACS Applied Materials & Interfaces*, acsami.8b16040, 2018. DOI: `10.1021/acsami.8b16040`.

[101] D. Hauschild, D. Kreikemeyer-Lorenzo, P. Jackson, T. M. Friedlmeier, D. Hariskos, F. Reinert, M. Powalla, C. Heske, and L. Weinhardt, "Impact of a RbF Postdeposition Treatment on the Electronic Structure of the CdS/Cu(In, Ga)Se$_2$ Heterojunction in High-Efficiency Thin-Film Solar Cells," *ACS Energy Letters*, pp. 2383–2387, 2017. DOI: `10.1021/acsenergylett.7b00720`.

[102] J. Moon, S. Rehan, T. R. Rana, B. O, S. K. Ahn, and S. Ahn, "Na-Induced Conversion of a Notorious Fine-Grained Residue Layer into a Working Absorber in Solution-Processed CuInSe$_2$ Devices," *Solar RRL*, vol. 3, no. 11, p. 1 900 260, 2019. DOI: `10.1002/solr.201900260`.

[103] S. Rehan, J. Moon, Y.-j. Eo, A. Cho, and J. Gwak, "Role of Na in solution-processed CuInSe$_2$ devices : a different story for efficiency improvement," vol. 48, no. February, p. 2017, 2017. DOI: `10.1016/j.nanoen.2018.03.065`.

[104] K. Granath, M. Bodegård, and L. Stolt, "The effect of NaF on Cu(In, Ga)Se$_2$ thin film solar cells," *Solar Energy Materials and Solar Cells*, vol. 60, no. 3, pp. 279–293, 2000. DOI: `10.1016/S0927-0248(99)00089-6`.

[105] E. S. Mungan, X. Wang, and M. A. Alam, "Modeling the Effects of Na Incorporation on CIGS Solar Cells," *IEEE Journal of Photovoltaics*, vol. 3, no. 1, pp. 451–456, 2013. DOI: `10.1109/JPHOTOV.2012.2221082`.

[106] H. Ruckh, D. Schmid, M. Kaiser, R. Schaffler, T. Walter, and H. Schock, "Influence of substrates on the electrical properties of Cu(In, Ga)Se$_2$ thin films," in *Proceedings of 1994 IEEE 1st World Conference on Photovoltaic Energy Conversion - WCPEC (A Joint Conference of PVSC, PVSEC and PSEC)*, vol. 1, IEEE, 1996, pp. 156–159, ISBN: 0-7803-1460-3. DOI: `10.1109/WCPEC.1994.519831`.

[107] C. A. Schneider, W. S. Rasband, and K. W. Eliceiri, "NIH Image to ImageJ: 25 years of image analysis," *Nature Methods*, vol. 9, no. 7, pp. 671–675, 2012. DOI: `10.1038/nmeth.2089`.

[108] D. Hauschild, F. Meyer, S. Pohlner, R. Lechner, R. Dietmüller, J. Palm, C. Heske, L. Weinhardt, and F. Reinert, "Impact of environmental conditions on the chemical surface properties of Cu(In, Ga)(S, Se)$_2$ thin-film solar cell absorbers," *Journal of Applied Physics*, vol. 115, no. 18, p. 183 707, 2014. DOI: `10.1063/1.4876257`.

[109] Q. Guo, G. M. Ford, H. W. Hillhouse, and R. Agrawal, "Sulfide Nanocrystal Inks for Dense $Cu(In_{1-x}, Ga_x)(S_{1-y}Se_y)_2$ Absorber Films and Their Photovoltaic Performance," *Nano Letters*, vol. 9, no. 8, pp. 3060–3065, 2009. DOI: `10.1021/nl901538w`.

[110] B. D. Chernomordik, A. E. Béland, D. D. Deng, L. F. Francis, and E. S. Aydil, "Microstructure Evolution and Crystal Growth in Cu_2ZnSnS_4 Thin Films Formed By Annealing Colloidal Nanocrystal Coatings," *Chemistry of Materials*, vol. 26, no. 10, pp. 3191–3201, 2014. DOI: `10.1021/cm500791a`.

[111] B. A. Williams, M. A. Smeaton, N. D. Trejo, L. F. Francis, and E. S. Aydil, "Effect of Nanocrystal Size and Carbon on Grain Growth during Annealing of Copper Zinc Tin Sulfide Nanocrystal Coatings," *Chemistry of Materials*, vol. 29, no. 4, pp. 1676–1683, 2017. DOI: `10.1021/acs.chemmater.6b05058`.

[112] C. M. Sutter-Fella, J. A. Stückelberger, H. Hagendorfer, F. La Mattina, L. Kranz, S. Nishiwaki, A. R. Uhl, Y. E. Romanyuk, and A. N. Tiwari, "Sodium Assisted Sintering of Chalcogenides and Its Application to Solution Processed $Cu_2ZnSn(S, Se)_4$ Thin Film Solar Cells," *Chemistry of Materials*, vol. 26, no. 3, pp. 1420–1425, 2014. DOI: `10.1021/cm403504u`.

[113] D. Braunger, D. Hariskos, G. Bilger, U. Rau, and H. Schock, "Influence of sodium on the growth of polycrystalline $Cu(In, Ga)Se_2$ thin films," *Thin Solid Films*, vol. 361-362, pp. 161–166, 2000. DOI: `10.1016/S0040-6090(99)00777-4`.

[114] A. R. Uhl, P. Fuchs, A. Rieger, F. Pianezzi, C. M. Sutter-Fella, L. Kranz, D. Keller, H. Hagendorfer, Y. E. Romanyuk, F. LaMattina, S. Yoon, L. Karvonen, T. Magorian-Friedlmeier, E. Ahlswede, D. VanGenechten, F. Stassin, and A. N. Tiwari, "Liquid-selenium-enhanced grain growth of nanoparticle precursor layers for $CuInSe_2$ solar cell absorbers," *Progress in Photovoltaics: Research and Applications*, vol. 23, no. 9, pp. 1110–1119, 2015. DOI: `10.1002/pip.2529`.

[115] C. J. Hages, M. J. Koeper, C. K. Miskin, K. W. Brew, and R. Agrawal, "Controlled Grain Growth for High Performance Nanoparticle-Based Kesterite Solar Cells," *Chemistry of Materials*, vol. 28, no. 21, pp. 7703–7714, 2016. DOI: `10.1021/acs.chemmater.6b02733`.

[116] W. Witte, R. Kniese, and M. Powalla, "Raman investigations of $Cu(In, Ga)Se_2$ thin films with various copper contents," *Thin Solid Films*, vol. 517, no. 2, pp. 867–869, 2008. DOI: `10.1016/j.tsf.2008.07.011`.

[117] B. Canava, J. Vigneron, A. Etcheberry, J. Guillemoles, and D. Lincot, "High resolution XPS studies of Se chemistry of a $Cu(In, Ga)Se_2$ surface," *Applied Surface Science*, vol. 202, no. 1-2, pp. 8–14, 2002. DOI: `10.1016/S0169-4332(02)00186-1`.

[118] J. A. Clark, A. R. Uhl, T. R. Martin, and H. W. Hillhouse, "Evolution of Morphology and Composition during Annealing and Selenization in Solution-Processed $Cu_2ZnSn(S, Se)_4$," *Chemistry of Materials*, vol. 29, no. 21, pp. 9328–9339, 2017. DOI: 10.1021/acs.chemmater.7b03313.

[119] F. Pianezzi, P. Reinhard, A. Chirilă, B. Bissig, S. Nishiwaki, S. Buecheler, and A. N. Tiwari, "Unveiling the effects of post-deposition treatment with different alkaline elements on the electronic properties of CIGS thin film solar cells," *Physical Chemistry Chemical Physics*, vol. 16, no. 19, pp. 8843–8851, 2014. DOI: 10.1039/c4cp00614c.

[120] T. Kodalle, M. D. Heinemann, D. Greiner, H. A. Yetkin, M. Klupsch, C. Li, P. A. van Aken, I. Lauermann, R. Schlatmann, and C. A. Kaufmann, "Elucidating the Mechanism of an RbF Post Deposition Treatment in CIGS Thin Film Solar Cells," *Solar RRL*, vol. 2, no. 9, p. 1 800 156, 2018. DOI: 10.1002/solr.201800156.

[121] A. Villanueva-Tovar, T. Kodalle, C. A. Kaufmann, R. Schlatmann, and R. Klenk, "Limitation of Current Transport across the Heterojunction in $Cu(In, Ga)Se_2$ Solar Cells Prepared with Alkali Fluoride Postdeposition Treatment," *Solar RRL*, vol. 4, no. 4, p. 1 900 560, 2020. DOI: 10.1002/solr.201900560.

[122] C. J. Hages, N. J. Carter, and R. Agrawal, "Generalized quantum efficiency analysis for non-ideal solar cells: Case of $Cu_2ZnSnSe_4$," *Journal of Applied Physics*, vol. 119, no. 1, p. 014 505, 2016. DOI: 10.1063/1.4939487.

[123] M. Troviano and K. Taretto, "Analysis of internal quantum efficiency in double-graded bandgap solar cells including sub-bandgap absorption," *Solar Energy Materials and Solar Cells*, vol. 95, no. 3, pp. 821–828, 2011. DOI: 10.1016/j.solmat.2010.10.028.

[124] S. Rehan, J. Moon, T. G. Kim, J. Gwak, J. Kim, J. W. Kim, W. Jo, S. K. Ahn, and S. Ahn, "Role of Na in solution-processed $CuInSe_2$ (CISe) devices: A different story for improving efficiency," *Nano Energy*, vol. 48, no. March, pp. 401–412, 2018. DOI: 10.1016/j.nanoen.2018.03.065.

[125] N. Nicoara, S. Harel, T. Lepetit, L. Arzel, N. Barreau, and S. Sadewasser, "Impact of KF Post-Deposition Treatment on Aging of the $Cu(In, Ga)Se_2$ Surface and Its Interface with CdS," *ACS Applied Energy Materials*, vol. 1, no. 6, pp. 2681–2688, 2018. DOI: 10.1021/acsaem.8b00365.

[126] B. P. Payne, M. C. Biesinger, and N. S. McIntyre, "Use of oxygen/nickel ratios in the XPS characterisation of oxide phases on nickel metal and nickel alloy surfaces," *Journal of Electron Spectroscopy and Related Phenomena*, vol. 185, no. 5-7, pp. 159–166, 2012. DOI: 10.1016/j.elspec.2012.06.008.

[127] S. M. McLeod, "Selenization and Grain Growth of Thin-Film CIGSSe from Nanoparticle Inks," PhD. Dissertation, Purdue University, 2017.

[128] S. Rehan, K. Y. Kim, J. Han, Y. J. Eo, J. Gwak, S. K. Ahn, J. H. Yun, K. H. Yoon, A. Cho, and S. J. Ahn, "Carbon-Impurity Affected Depth Elemental Distribution in Solution-Processed Inorganic Thin Films for Solar Cell Application," *ACS Applied Materials and Interfaces*, vol. 8, no. 8, pp. 5261–5272, 2016. DOI: 10.1021/acsami.5b10789.

[129] W. Wu, Y. Cao, J. V. Caspar, Q. Guo, L. K. Johnson, I. Malajovich, H. D. Rosenfeld, and K. R. Choudhury, "Studies of the fine-grain sub-layer in the printed CZTSSe photovoltaic devices," *Journal of Materials Chemistry C*, vol. 2, no. 19, p. 3777, 2014. DOI: 10.1039/c4tc00391h.

[130] D. R. Baer, "Guide to making XPS measurements on nanoparticles," *Journal of Vacuum Science & Technology A*, vol. 38, no. 3, p. 031 201, 2020. DOI: 10.1116/1.5141419.

[131] Q. Guo, G. M. Ford, W. C. Yang, C. J. Hages, H. W. Hillhouse, and R. Agrawal, "Enhancing the performance of CZTSSe solar cells with Ge alloying," *Solar Energy Materials and Solar Cells*, vol. 105, pp. 132–136, 2012. DOI: 10.1016/j.solmat.2012.05.039.

[132] N. J. Carter, R. Mainz, B. C. Walker, C. J. Hages, J. Just, M. Klaus, S. S. Schmidt, A. Weber, W.-C. D. Yang, O. Zander, E. A. Stach, T. Unold, and R. Agrawal, "The role of interparticle heterogeneities in the selenization pathway of Cu–Zn–Sn–S nanoparticle thin films: a real-time study," *J. Mater. Chem. C*, vol. 3, no. 27, pp. 7128–7134, 2015. DOI: 10.1039/C5TC01139F.

[133] P. Jackson, D. Hariskos, E. Lotter, S. Paetel, R. Wuerz, R. Menner, W. Wischmann, and M. Powalla, "New world record efficiency for Cu(In, Ga)Se$_2$ thin-film solar cells beyond 20%," *Progress in Photovoltaics: Research and Applications*, vol. 19, no. 7, pp. 894–897, 2011. DOI: 10.1002/pip.1078.

[134] P. Jackson, R. Wuerz, D. Hariskos, E. Lotter, W. Witte, and M. Powalla, "Effects of heavy alkali elements in Cu(In, Ga)Se$_2$ solar cells with efficiencies up to 22.6%," *physica status solidi (RRL) – Rapid Research Letters*, vol. 10, no. 8, pp. 583–586, 2016. DOI: 10.1002/pssr.201600199.

[135] T. Feurer, R. Carron, G. Torres Sevilla, F. Fu, S. Pisoni, Y. E. Romanyuk, S. Buecheler, and A. N. Tiwari, "Efficiency Improvement of Near-Stoichiometric CuInSe$_2$ Solar Cells for Application in Tandem Devices," *Advanced Energy Materials*, vol. 9, no. 35, pp. 2–7, 2019. DOI: 10.1002/aenm.201901428.

[136] M. Raghuwanshi, A. Vilalta-Clemente, C. Castro, S. Duguay, E. Cadel, P. Jackson, D. Hariskos, W. Witte, and P. Pareige, "Influence of RbF post deposition treatment on heterojunction and grain boundaries in high efficient (21.1%) $Cu(In, Ga)Se_2$ solar cells," *Nano Energy*, vol. 60, no. March, pp. 103–110, 2019. DOI: `10.1016/j.nanoen.2019.03.028`.

[137] A. J. McEvoy, L. Castaner, and T. Markvart, *Solar cells : materials, manufacture and operation*. Academic Press, 2013, ISBN: 0080993796.

[138] S. H. Wei and A. Zunger, "Band offsets and optical bowling of chalcopyrite and Zn-based II-IV alloys," *Journal of Applied Physics*, vol. 78, no. September, p. 3846, 1995.

[139] T. Dullweber, G. Hanna, W. Shams-Kolahi, A. Schwartzlander, M. Contreras, R. Noufi, and H. Schock, "Study of the effect of gallium grading in $Cu(In, Ga)Se_2$," *Thin Solid Films*, vol. 361-362, pp. 478–481, 2000. DOI: `10.1016/S0040-6090(99)00845-7`.

[140] H.-W. Schock, R. Noufi, M. Contreras, U. Rau, and T. Dullweber, "Photogeneration and carrier recombination in graded gap $Cu(In, Ga)Se_2$ solar cells," *IEEE Transactions on Electron Devices*, vol. 47, no. 12, pp. 2249–2254, 2000. DOI: `10.1109/16.887004`.

[141] D. Drouin, A. R. Couture, D. Joly, X. Tastet, V. Aimez, and R. Gauvin, "CASINO V2.42—A Fast and Easy-to-use Modeling Tool for Scanning Electron Microscopy and Microanalysis Users," *Scanning*, vol. 29, no. 3, pp. 92–101, 2007. DOI: `10.1002/sca.20000`.

[142] M. Gloeckler and J. R. Sites, "Band-gap grading in $Cu(In, Ga)Se_2$ solar cells," *Journal of Physics and Chemistry of Solids*, vol. 66, no. 11, pp. 1891–1894, 2005. DOI: `10.1016/j.jpcs.2005.09.087`.

[143] J. Wang, Y. F. Zhang, F. Dong, and J. Zhu, "Ga-grading profiles formed by incorporation of gallium into $Cu(In_{1-x}, Ga_x)Se_2$ absorber thin films," *Applied Surface Science*, vol. 258, no. 22, pp. 8636–8640, 2012. DOI: `10.1016/j.apsusc.2012.05.065`.

[144] N. Barreau, T. Painchaud, F. Couzinié-Devy, L. Arzel, and J. Kessler, "Recrystallization of CIGSe layers grown by three-step processes: A model based on grain boundary migration," *Acta Materialia*, vol. 58, no. 17, pp. 5572–5577, 2010. DOI: `10.1016/j.actamat.2010.06.025`.

A. APPENDIX: RAPID THERMAL PROCESSING FURNACE EXPERIMENTAL DETAILS

Temperature profiles of representative RTP runs are given below. T_{sample} and T_{Se} denote the sample and selenium temperatures; see Figure A.1 for temperature measurement positions on RTP diagram, and Figure A.2 for an image of graphite tray with the sample placed along with the glass shims.
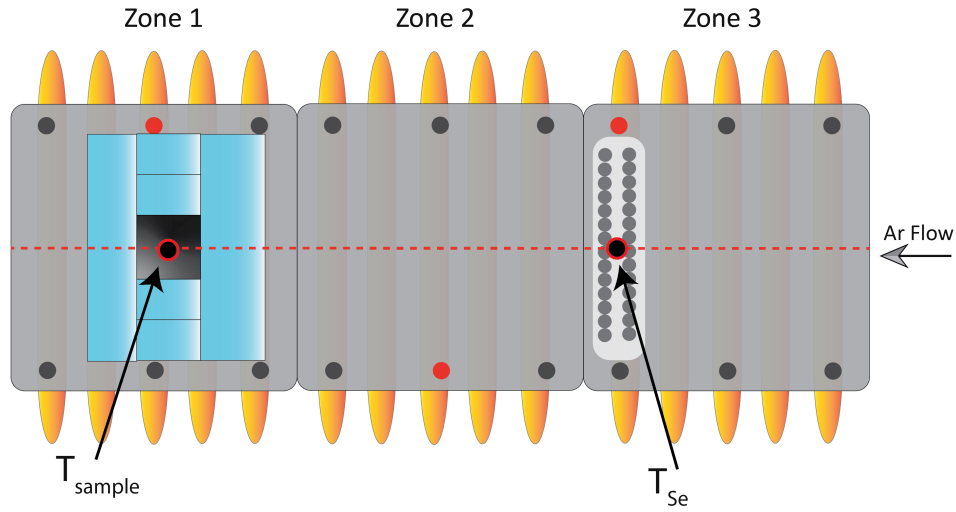

Figure A.1. Rapid thermal processing furnace diagram with T_{sample} and T_{Se} denoted.
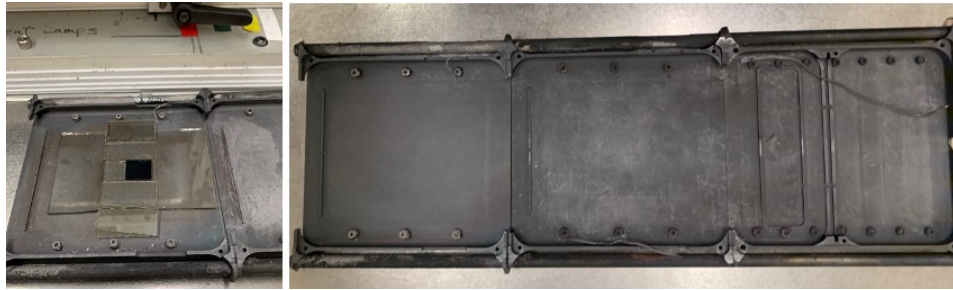

Figure A.2. (Right) Image of graphite tray used in RTP, on which the sample and Se are placed. (Left) CIGS nanoparticle film placed on Zone 1, along with glass shims to control the flow.

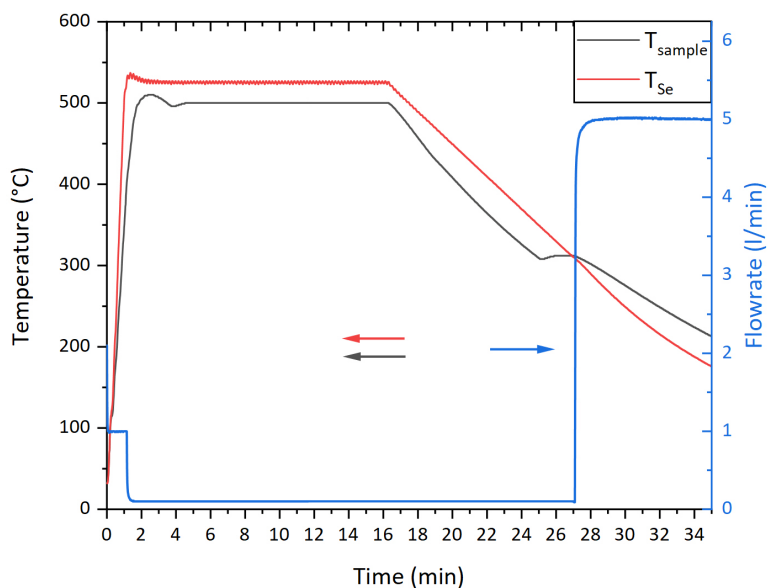## A.1 Representative Temperature Profiles

Figure A.3. Representative temperature-time and Ar flow-time profiles of an RTP run. Sample was selenized at 500 °C, with Se at 525 °C for 15 minutes. Furnace is cooled in a controlled manner ensuring that the Se is always hotter than the sample, until 300 °C. Ar flowrate was set at 0.1 l/min during the selenization and controlled cool stages.
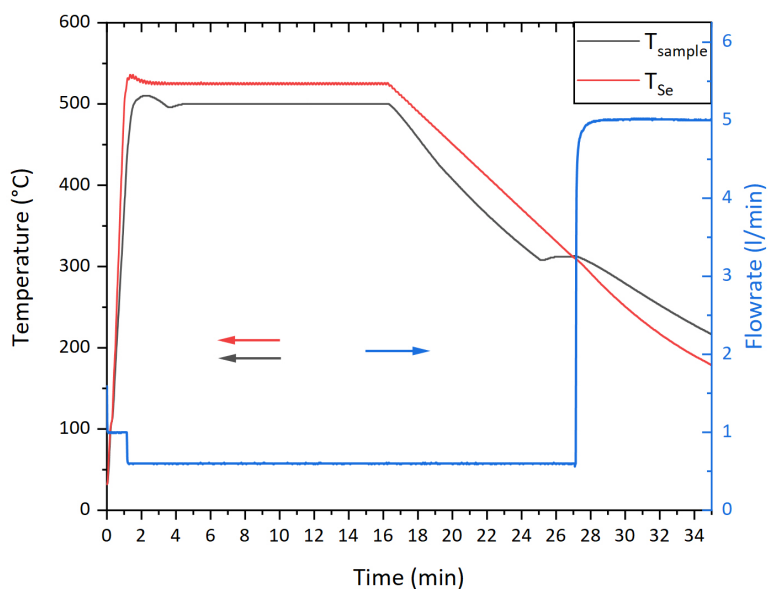
Figure A.4. Representative temperature-time and Ar flow-time profiles of an RTP run. Sample was selenized at 500 °C, with Se at 525 °C for 15 minutes. Furnace is cooled in a controlled manner ensuring that the Se is always hotter than the sample, until 300 °C. Ar flowrate was set at 0.6 l/min during the selenization and controlled cool stages.

Figure A.5. Representative temperature-time and Ar flow-time profiles of an RTP run. Sample was selenized at 550 °C, with Se at 575 °C for 10 minutes. Furnace is cooled in a controlled manner ensuring that the Se is always hotter than the sample, until 300 °C. Ar flowrate was set at 0.1 l/min during the selenization and controlled cool stages.
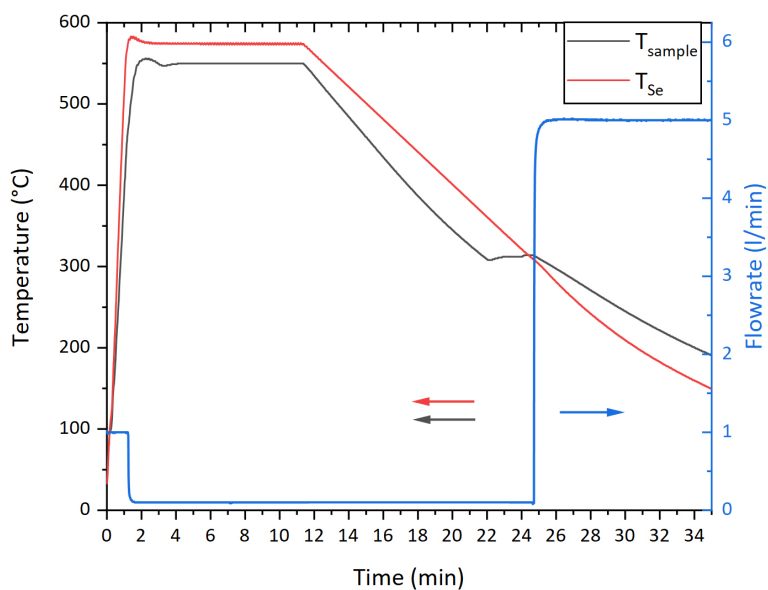
Figure A.6. Representative temperature-time and Ar flow-time profiles of an RTP run. Sample was selenized at 550 °C, with Se at 575 °C for 10 minutes. Furnace is cooled in a controlled manner ensuring that the Se is always hotter than the sample, until 300 °C. Ar flowrate was set at 0.3 l/min during the selenization and controlled cool stages.
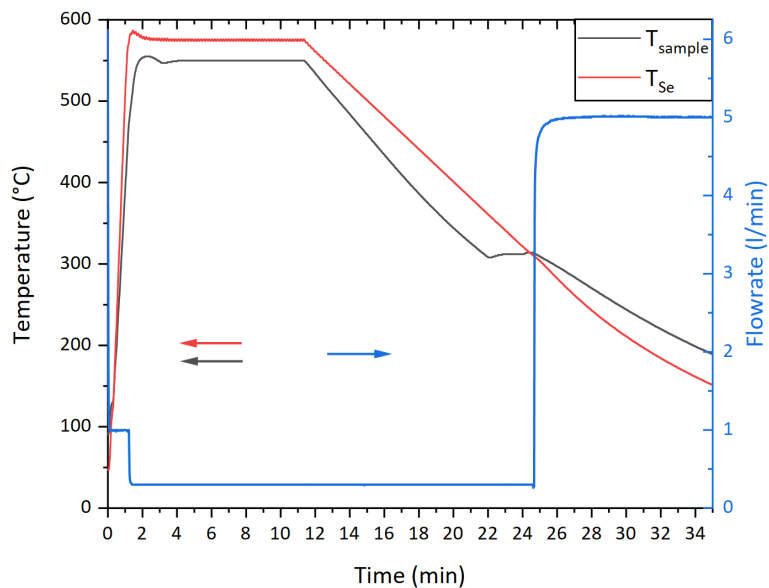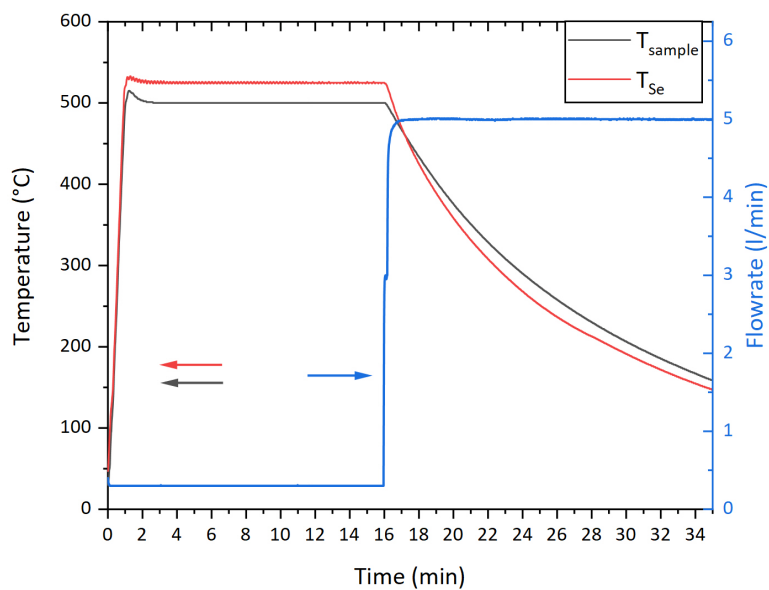

Figure A.7. Representative temperature-time and Ar flow-time profiles of an RTP run. Sample was selenized at 500 °C, with Se at 525 °C for 15 minutes. Furnace is cooled naturally. Ar flowrate was set at 0.3 l/min during the selenization.

VITA

Essam Homoud Alruqobah was born in July 18th 1992 to Homoud and Lamyaa Al-ruqobah. He has one older brother, Abdullah. Growing up with a chemical engineer father, he developed an aptitude towards math and science. In 2010, he graduated from Jaber Al-Mubarak High School (Science Branch).

Following the footsteps of his father, Essam enrolled in the chemical engineering undergraduate program at Kuwait University's College of Engineering and Petroleum. He graduated with a Bachelor of Science, Honors, in Chemical Engineering in 2014. In 2015, Essam was awarded a highly-competitive fellowship for graduate studies in the United States.

In 2015, Essam joined the graduate program at the Davidson School of Chemical Engineering, Purdue University. He joined Prof. Rakesh Agrawal's Solar Research Group, working on the synthesis and fabrication of solar cell absorber films and devices from nanoparticle-based precursors. He obtained his Master of Science degree in 2017, and his PhD. in 2020. After obtaining his PhD. , Essam accepetd an offer for an assistant professor at his alma mater, Kuwait University.

PUBLICATIONS

• McLeod, S.; **Alruqobah, E.**; Agrawal, R. Liquid Assisted Grain Growth in Solution Processed $Cu(In, Ga)(S, Se)_2$. Sol. Energy Mater. Sol. Cells 2019, 195, 12–23.

• **Alruqobah, E. H.**; Agrawal, R. Potassium Treatments for Solution-Processed $Cu(In, Ga)(S, Se)_2$ Solar Cells. Appl. Energy Mater. 2020, 3 (5), 4821–4830.

• Ellis, R. G.; Turnley, J. W.; Rokke, D. J.; Fields, J. P.; **Alruqobah, E. H.**; Deshmukh, S. D.; Kisslinger, K.; Agrawal, R. Hybrid Ligand Exchange of $Cu(In, Ga)S_2$ Nanoparticles for Carbon Impurity Removal in Solution-Processed Photovoltaics. Chem. Mater. 2020, 32, 5091–5103.

• Ellis, R. G.; **Alruqobah, E. H.**; Turnley, J. W.; Agrawal, R. Improving Solution Processed CIGSSe Devices Through Colloidal Nanoparticle Ligand Exchange. In Conference Record of the IEEE Photovoltaic Specialists Conference; 2020.

• Suresh, S.; **Alruqobah, E. H.**; Rokke, D. J.; Agrawal, R.; Uhl, A. Extrinsic doping of solution-processed $Cu(In, Ga)(S, Se)_2$ and $CuIn(S, Se)_2$ absorbers. In Preparation

• **Alruqobah, E. H.**; Agrawal, R. Surface RbF Treatments for Solution-Processed $Cu(In, Ga)(S, Se)_2$ Solar Cells. *In Preparation.*

• **Alruqobah, E. H.**; Agrawal, R. Effect of Capping Ligand on the Selenization and Growth of CIGSSe Films from Nanoparticle Precursors. *In Preperation.*